Volume 49
Number 14
21 July 2020
Pages 4595–5102

Chem Soc Rev

Chemical Society Reviews

rsc.li/chem-soc-rev

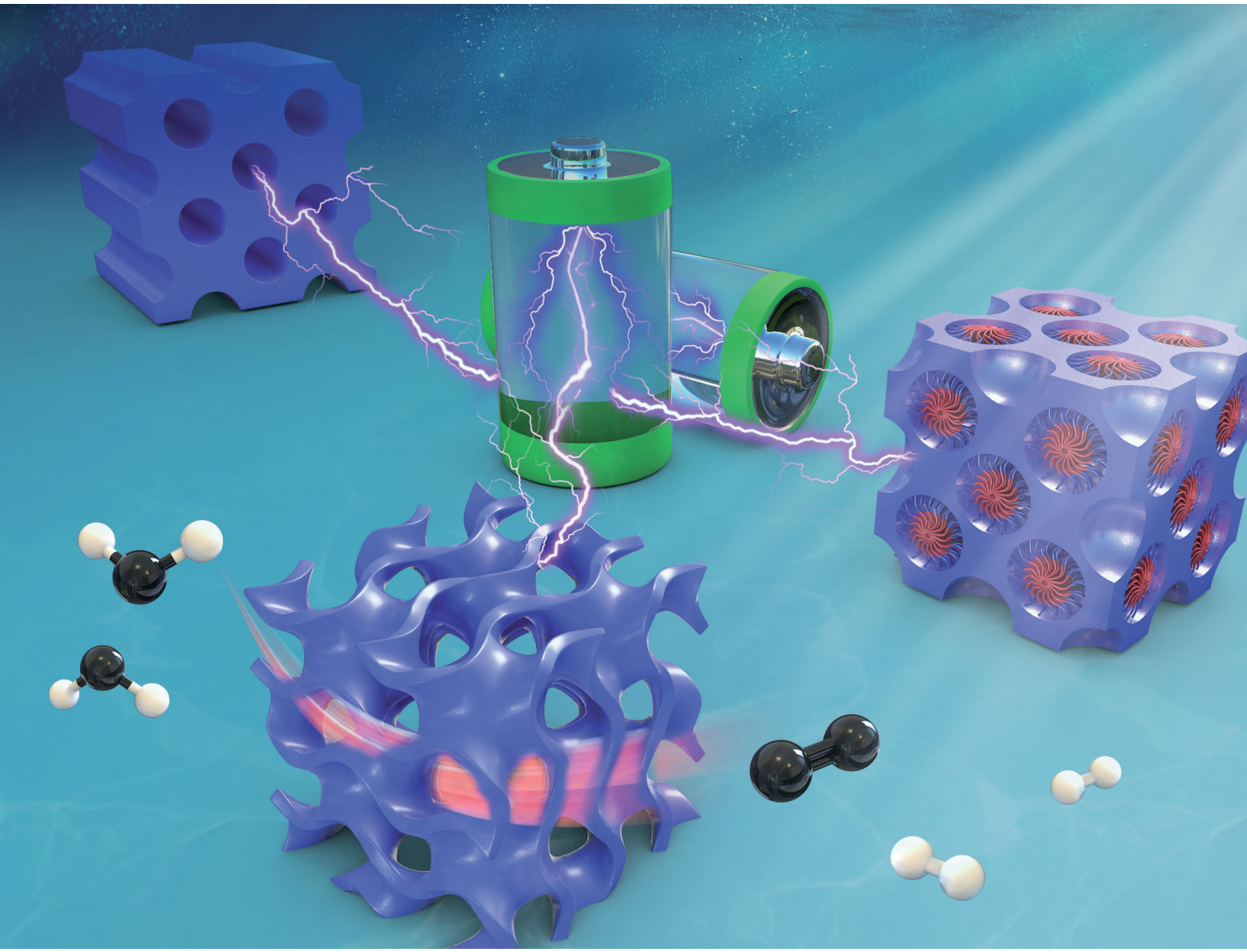

ISSN 0306-0012

ROYAL SOCIETY OF CHEMISTRY

REVIEW ARTICLE

Yiyong Mai, Yusuke Yamauchi *et al.*

Self-assembly of block copolymers towards mesoporous materials for energy storage and conversion systems

Chem Soc Rev

REVIEW ARTICLE

View Article Online
View Journal | View Issue

Cite this: *Chem. Soc. Rev.*, 2020, **49**, 4681

Self-assembly of block copolymers towards mesoporous materials for energy storage and conversion systems

Chen Li,†[a] Qian Li,†[a] Yusuf Valentino Kaneti,[b] Dan Hou,[a] Yusuke Yamauchi *[cd] and Yiyong Mai *[a]

Self-assembly of block copolymers (BCPs) provides a versatile strategy for controllable preparation of a broad range of functional materials with different ordered structures. In recent decades, this soft-templating strategy has been widely utilized for preparing a wide range of mesoporous materials. These porous materials have attracted tremendous interest in energy storage and conversion (ESC) applications in view of their ability to absorb, store, and interact with guest species on their exterior/interior surfaces and in the pore space. Compared with other synthetic approaches, such as template-free and hard-templating methods, BCP soft-templating protocols show great advantages in the construction of large mesopores with diameters between 10–60 nm, which are suitable for applications requiring the storage or hosting of large-sized species/molecules. In addition, this strategy shows incomparable merits in the flexible control of pore size/architecture/wall thickness, which determines the final performance of mesoporous materials in ESC devices. In the last decade, rapid development has been witnessed in the area of BCP-templated mesoporous materials. In this review paper, we overview the progress of this field over the past 10 years, with an emphasis on the discussions of synthetic methodologies, the control of materials structures (including morphology and pore size/shape), and potential applications particularly in rechargeable batteries, supercapacitors, electro-/photocatalysis, solar cells, *etc.*

Received 11th January 2020

DOI: 10.1039/d0cs00021c

rsc.li/chem-soc-rev

[a] *School of Chemistry and Chemical Engineering, Frontiers Science Center for Transformative Molecules, Shanghai Key Laboratory of Electrical Insulation and Thermal Ageing, Shanghai Jiao Tong University, 800 Dongchuan Road, Shanghai 200242, China. E-mail: mai@sjtu.edu.cn*

[b] *International Center for Materials Nanoarchitectonics (WPI-MANA), National Institute for Materials Science (NIMS), 1-1 Namiki, Ibaraki 305-0044, Japan*

[c] *School of Chemical Engineering and Australian Institute for Bioengineering and Nanotechnology (AIBN), The University of Queensland, Brisbane, QLD 4072, Australia. E-mail: y.yamauchi@uq.edu.au*

[d] *Key Laboratory of Marine Chemistry Theory and Technology, Ministry of Education, Ocean University of China, Qingdao 266100, China*

† These authors contributed equally to this work.

Chen Li

Chen Li received her Master's degree from the Shanghai Institute of Ceramics, Chinese Academy of Science, in 2018. She joined the group of Prof. Yiyong Mai at Shanghai Jiao Tong University in September 2018 as a PhD student. Her current study focuses on the self-assembly of block polymers and mesoporous materials for energy storage and conversion applications.

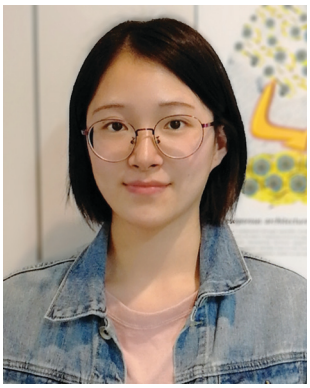

Qian Li

Qian Li received her Bachelor's degree from the Power Metallurgy Research Institute, Central South University, in 2017. She is currently pursuing her PhD degree under the supervision of Prof. Yiyong Mai at Shanghai Jiao Tong University. Her present study focuses on block copolymer-templated synthesis of mesoporous materials for energy storage and conversion applications.

1. Introduction

In recent years, serious energy and environmental problems have prompted the development of green and efficient energy storage and conversion (ESC) systems. Extensive effort has been devoted to developing functional electrode materials with high performance for ESC devices.[1–3] Porous materials, in particular mesoporous solids, have attracted enormous interest in numerous energy-related applications owing to their ability to absorb, store, and interact with guest species on their exterior/interior surfaces and in the pore space.[4–6] The International Union of Pure and Applied Chemistry (IUPAC) has defined the pore dimension of mesoporous materials to be in the range of 2–50 nm.[2,5] Inspired by the first synthesis of mesoporous silica in the 1990s, a diverse range of mesoporous materials involving a broad range of compositions have been developed thus far, including carbons, metallic compounds, noble metals, and their hybrids. These materials are appealing candidates for ESC applications due to their high electrochemical or catalytic activity and will be the main focus of this review.

Mesoporous materials possess a number of intrinsic properties, including high specific surface area (SSA), large pore volume, tunable pore size and shape. In many energy applications, especially with surface or interface-related processes (*e.g.*, adsorption, catalysis and energy storage), high surface area materials are desired because they can provide a large number of active sites.[2,5,6] Furthermore, the large pore volume of mesoporous

Yusuf Valentino Kaneti

Yusuf Valentino Kaneti received his PhD from the University of New South Wales in July 2014 under the supervision of Prof. Aibing Yu. He joined the group of Prof. Yusuke Yamauchi at the National Institute of Materials Science as a JSPS Postdoctoral Fellow in September 2016. He is now working as a MANA Research Associate at NIMS. His research interest is focused on the fabrication of functional porous materials for energy and environmental applications.

Dan Hou

Dan Hou obtained his Bachelor's degree from Qingdao University of Science and Technology in 2017. He joined Prof. Yiyong Mai's group as a master candidate in September 2017. His current research interest involves the synthesis of mesoporous materials and their applications in energy storage and conversion systems.

Yusuke Yamauchi

Yusuke Yamauchi received his bachelor's degree (2003), master's degree (2004), and PhD degree (2007) from Waseda University, Japan. After that, he joined thr National Institute for Materials Science to start his research group. Currently, he is a full professor at the School of Chemical Engineering and a senior group leader at AIBN in The University of Queensland. He concurrently serves as an associate editor of J Mater Chem A (RSC) and Chem Eng J (Elsevier). He has published over 750 papers with >40 000 citations (h-index >100). He was selected as the Highly Cited Researchers in Chemistry in 2016–2019.

Yiyong Mai

Prof. Yiyong Mai received his PhD from Shanghai Jiao Tong University in April 2007 under the supervision of Prof. Deyue Yan. He joined the group of Prof. Adi Eisenberg at McGill University as a Postdoctoral Fellow in September 2008, where he was promoted as a Research Associate in March 2012. He has been a Professor at the School of Chemistry and Chemical Engineering, Shanghai Jiao Tong University, since March 2013. He visited the group of Prof. Klaus Müllen at Max Plank Institute for Polymer Research (MPIP) as a visiting scholar from May to October 2013. He was awarded "Distinguished Professor of Special Appointment at Shanghai Institutions of Higher Learning" in 2014/2018 and "Shanghai Academic Research Leader" in 2019, respectively. His present research interest involves polymer self-assembly and functional materials for optoelectronic and energy-related applications. He has published over 100 papers in international refereed journals with >5000 total citations.

materials is advantageous for achieving a high loading of guest species and for accommodating volume expansion and strain relaxation during repeated charge/discharge processes in energy storage devices. Pore size and structure significantly affect mass transport inside porous materials. For example, large mesopores allow for increased accessibility to the active sites as well as better accommodation and transport of large-sized species compared to microporous materials (pore size <2 nm).[7,8] In addition, different pore structures, such as spherical,[9–11] cylindrical,[12,13] or bicontinuous pores,[14–16] result in different mass transport modes in the interiors of materials, thus affecting the effective surface area and the amount of accessible active sites. Therefore, achieving a balanced control of pore size and architecture is essential for optimizing the effective surface area and pore volume of mesoporous materials, both of which are highly crucial in determining their performance in ESC devices.

To date, various synthetic protocols have been developed for synthesizing mesoporous materials, including template-free,[17–19] hard-templating,[20–22] and soft-templating approaches.[1,23,24] Generally speaking, these approaches all have their own unique advantages. Template-free methods usually involve the chemical connection or aggregation of nanoscale building blocks. For example, reticular chemistry broadens the spectrum of mesoporous materials by creating metal–organic frameworks (MOFs)[25–27] and covalent organic frameworks (COFs)[28–30] through molecular building blocks (such as organic molecules and inorganic clusters). However, template-free strategies typically suffer from difficulties in tailoring the morphology and pore structures of the resulting mesoporous materials.[2,31,32] Hard-templating methods (also known as nanocasting) usually employ preformed rigid mesoporous materials, such as silica, carbon, or colloidal crystals, as hard templates.[20,33,34] Benefiting from some hard templates that can offer enhanced structural stability at high temperatures, this method facilitates the preparation of highly crystalline or even single-crystalline mesoporous materials. Nevertheless, this approach suffers from tedious multi-step procedures for removing the template and the utilization of corrosive agents, which impede the massive production of mesoporous materials by this method.[33–35] In contrast, soft templates generally refer to "soft" molecules, including small-molecule surfactants and block copolymers (BCPs). As these soft molecules can self-assemble into a wide variety of ordered nanostructures, the soft-templating strategy shows great advantages in determining the pore shape or size. Moreover, the soft molecules can be easily dissolved in common solvents, including water, and can be pyrolyzed at high temperatures under inert atmosphere. These features enable the facile removal of the soft templates. Compared with small-molecule surfactants, BCPs have several additional merits as pore-forming agents. First, the morphological control of BCP assemblies is more flexible as the properties of BCPs, such as compositions, molecular weights, and volume fractions, can be controlled to adjust their packing parameters (p),[36–38] which offers the possibility of creating porous materials with a broader range of pore architectures. Second, low-molecular weight surfactants usually lead to the formation of mesoporous materials with small mesopores (usually 4–6 nm) due to their short hydrophobic chains,[23] while high molar mass BCPs afford the possibilities of synthesizing mesoporous materials with large pore sizes (10–60 nm) and thick pore walls, which are suitable for applications requiring the storage or hosting of large-sized species/molecules.[23,39,40] Third, the hydrophobic blocks of most BCPs consist of sp- or sp^2-carbon atoms, which can be *in situ* carbonized to residual carbons and thus support the formation or crystallization of pore walls during high-temperature treatment under inert atmosphere.[1,41–43]

In light of the exceptional advantages of BCP self-assembly in the synthesis of mesoporous materials as well as the extensive interest and the high level of activity of this area, this review article describes the recent progress in the field of mesoporous materials over the past 10 years. Different from existing review articles,[2,40,43–45] this paper is more comprehensive. It not only introduces the key principles of BCP self-assembly in the bulk and in solution, providing essential guidance for the construction of mesoporous materials, but also covers all the prevalent and newly emerging synthetic strategies, including bulk self-assembly, solvent evaporation-induced self-assembly (EISA), nanoprecipitation, interfacial self-assembly, and emulsion-templating self-assembly. In particular, the control of the morphology and pore geometry/size of mesoporous materials and its necessity in different ESC systems are discussed, which may help to understand the advantages of the BCP self-assembly-guided synthetic strategies. Following the introduction, the second section introduces the basic principles of the self-assembly of BCPs in the bulk and in solution. The third section discusses the synthetic strategies towards mesoporous materials, including their principles, advantages and disadvantages. The fourth section covers the potential applications of mesoporous materials in various ESC systems, including secondary batteries, supercapacitors, electro- or photo-catalysis, and solar cells. In this section, the advantages and disadvantages of mesopores as well as the effect of their sizes/shapes on the functional performance of ESC devices are also described. The final section presents the summary and future outlook on the development of this area.

2. Self-assembly of block copolymers

In general, the self-assembly of BCPs can occur both in the bulk[46–48] and in solution.[36,37,49–53] Taking diblock copolymers as an example, bulk BCPs with immiscible blocks can separate into microphases with various morphologies, including spheres (S), cylinders (C), bicontinuous structures (G), lamellae (L), *etc.*, as shown in Fig. 1.[46,54,55] The morphology is mainly dependent on three parameters:[46,56] (1) χ_{AB}, namely, the Flory–Huggins parameter that expresses the degree of incompatibility between the two different blocks; (2) the total degree of polymerization ($N = N_A + N_B$), and (3) the volume fractions of A and B blocks (f_A and f_B, $f_A + f_B = 1$). The degree of microphase separation of diblock copolymers is determined by the segregation product, χN. With increasing f_A at a fixed χN above 10.5 (critical order-to-disorder transition point), the order-to-order transition (OOT) of BCPs occurs from closely packed spheres (CPS), going through body-centered cubic spheres (S), hexagonally packed cylinders

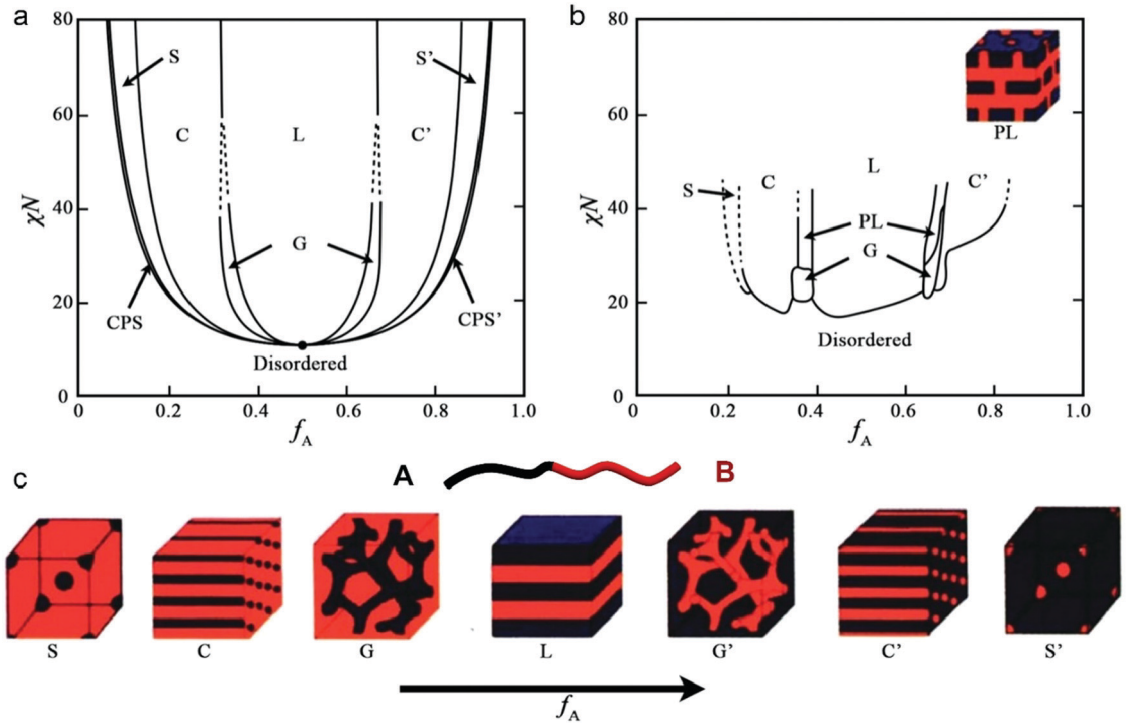

Fig. 1 Self-assembly of BCPs in the bulk. (a) Theoretical phase diagram of AB diblock copolymers predicted by the self-consistent mean-field theory, depending on volume fraction (f) of the blocks and the segregation parameter, χN, where χ is the Flory–Huggins parameter and N is the degree of polymerization. (b) Experimental phase portrait of PI-*b*-PS copolymers, in which f_A represents the volume fraction of polyisoprene, PL = perforated lamellae. (c) Equilibrium morphologies of AB diblock copolymers in the bulk. In these figures, CPS and CPS′ = closely packed spheres, S and S′ = body-centered cubic spheres, C and C′ = hexagonally packed cylinders, G and G′ = bicontinuous gyroids, and L = lamellae. Reproduced with permission.[37] Copyright 2012, Royal Society of Chemistry.

(C) and bicontinuous gyroids (G), to lamellae (L). With the copolymer composition inverted, morphological inversion takes place following the order L–G′–C′–S′–CPS′-disordered. The morphological phase diagram has been verified experimentally by many diblock copolymers in the bulk, *e.g.* polyisoprene-*block*-polystyrene (PI-*b*-PS).[54] For multiblock copolymers, the level of complexity for their phase separation increases with the increase in the number of blocks. For example, theoretical simulation has predicted the existence of 30 different morphologies for phase separation of ABC triblock copolymers and many of them have been obtained experimentally.[57,58] A lot of these ordered structures are different from those formed by diblock copolymers, which provide opportunities for creation of novel mesoporous materials.[23,59–61]

The self-assembly of amphiphilic BCPs in aqueous solutions is one of the most widely used template-based strategies for synthesizing mesoporous materials.[1,23,24,59] The hydrophobic interaction of the hydrophobic blocks drives the aggregation of amphiphilic BCP chains. The formed aggregates are protected by hydrophilic coronae in aqueous solutions, which reduce the contact of the hydrophobic block with water, thus minimizing the system energy. The aggregates mainly include spherical micelles, cylindrical micelles, bicontinuous structures, lamellae, vesicles, and their inverse structures, *etc.* (Fig. 2).[37,62] Their final morphologies are determined by the packing parameter, $p = v/a_0 l_c$, where v and l_c represent the volume and length of the hydrophobic segment, respectively, while a_0 denotes the contact area of the hydrophilic block.[36,37,63,64] Generally, When $p < 1/3$, spherical micelles or spheres with face-centered cubic (fcc) and body-centered cubic (bcc) packing modes can be formed, depending on the adopted self-assembly approach; if $1/3 < p < 1/2$, cylindrical micelles or hexagonally packed cylinders (Hex) can be formed; when $1/2 < p < 1$, vesicles or modulated lamellae; when $p = 1$, planar bilayers or multi-layered lamellae; if $p > 1$, minimal surfaces (G, D, and P surfaces) or inverse Hex, fcc, and bcc structures can be formed. The general principle for the morphological transition can be simply explained by the classical cone-column geometric change mechanism, as illustrated in Fig. 2,[36,37,63] which is also applicable to microphase separation of BCPs in the bulk. The packing parameter is affected by a number of factors, including the polymer composition and concentration, nature of the solvent, water content, addition of additives, and so on.[37,65–69] The adjustments of these influencing factors afford flexible control over the morphology and dimension of BCP aggregates. In general, the preparation of mesoporous materials templated by BCP aggregates requires the cooperative self-assembly of BCPs and specific precursors that may form the pore walls in solutions, followed by cross-linking or polymerization of the precursors.[1,23,70] During self-assembly, the effects of the added precursors on the morphology of the resulting aggregates and the resulting pore architectures primarily originate from the variations in the interactions among corona chains in the presence

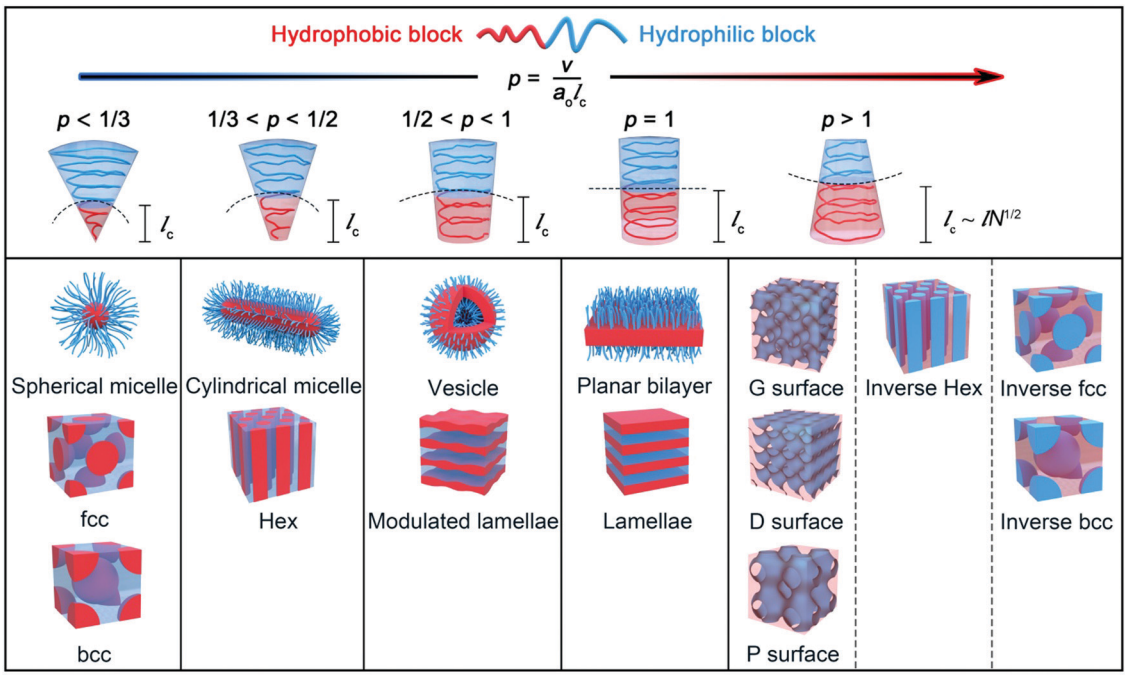

Fig. 2 Schematic phase diagram of block copolymer self-assembly in solution, which presents the major morphologies. The self-assembled structures are determined by the packing parameter (p) of the copolymer chains, which correlates with their conical or columnar arrangements in the assemblies. The definitions of the symbols and formulas are given in the main text.

of the precursors. Although the co-self-assembly systems are more complicated, the principle of the morphological control is analogous to that of the solo self-assembly of BCPs.[1,23,71] For most mesoporous materials, their pores are templated by the hydrophobic domains in the self-assembled structures, in which the length (l_c) of the hydrophobic block of the copolymer chain is approximately equal to $lN^{1/2}$ (Fig. 2),[9,46,72] where l represents the length of one repeat unit and N is the number of repeating units; thus, the dimensions of the created mesopores are nearly proportional to $lN^{1/2}$.

3. Synthetic strategies

In 1997, Wiesner's group synthesized mesoporous aluminosilicates with pore sizes of 10–50 nm, by employing high-molar-mass polyisoprene-*b*-poly(ethylene oxide) (PI-*b*-PEO) diblock copolymers as structure-guiding agents.[39] In 1998, Zhao *et al.* prepared ordered mesoporous silica (SBA-15) with large pore sizes of 4–12 nm in solution, employing commercial triblock poly(ethylene oxide)–poly(propylene oxide)–poly(ethylene oxide) (PEO–PPO–PEO) copolymers as soft templates.[73] These pioneering studies opened up avenues for the synthesis of mesoporous materials with large-sized pores, which have been explored in energy, catalysis, and separation applications, especially those involving large molecules.[2,23,39,74] These studies also inspired the wide utilization of BCPs, including Pluronic (commercial PEO–PPO–PEO series including P123, F127, F108, *etc.*)[61,75–77] and non-Pluronic families, for preparing mesoporous materials.[2,40,78,79] Compared to the Pluronic copolymers, non-Pluronic BCPs generally consist of hydrophilic blocks, such as poly(ethylene oxide) (PEO), poly(2-vinylpyridine) (P2VP) or poly(4-vinylpyridine) (P4VP), and hydrophobic blocks including polystyrene (PS), polyisoprene (PI), and polyacrylonitrile (PAN), among others. The merits of these non-Pluronic copolymers include their lower oxygen and higher carbon contents as well as higher glass transition temperatures (T_g) and better thermal stability.[23] Moreover, these copolymers are typically laboratory-made through controllable living polymerization methodologies, such as atom transfer radical polymerization (ATRP)[80–82] and reversible addition–fragmentation chain transfer polymerization (RAFT).[83–85] Hence, the compositions, volume fractions, and molar masses of the composing blocks can be readily controlled, which makes the non-Pluronic BCPs desirable templates for the construction of mesoporous materials with tunable pore size/architecture/wall thickness/composition. To date, a number of powerful synthetic strategies based on the self-assembly of BCPs have been developed, which mainly include bulk self-assembly, EISA, solution-based nanoprecipitation, interfacial self-assembly, and emulsion-templating self-assembly. In the following subsections, these strategies will be introduced in detail; their accessible materials and structures, and advantages and disadvantages are summarized in Table 1.

3.1 Bulk self-assembly

The phase separation of BCPs in the bulk is mostly applied for preparing mesoporous carbon materials. In the bulk, the self-assembly of BCPs usually takes place with heating and annealing of the polymers at temperatures higher than their T_gs, which enable the microphase separation of the BCPs into ordered morphologies.[37,54] Then, the resulting ordered morphologies

Table 1 Comparison of the currently available synthetic strategies towards mesoporous materials

Methods	Existing material categories	Existing typical structures	Advantages	Disadvantages
Bulk self-assembly	Carbons	Films or monoliths with spherical mesopores	One step; easily processable; fewer parameters affecting the final pore structure	Limited BCP category; difficult for mass production; only applicable to carbon materials; limited morphologies of materials
EISA	Metal compounds (metal oxides, metal minerals, *etc.*); carbons; metals; hybrids (carbon/metal, carbon/metal oxide, *etc.*)	Films or monoliths with spherical, cylindrical, bicontinuous, or hierarchical pore structures	Applicable to the synthesis of a wide range of mesoporous materials; accessible to various highly ordered pore structures; easy for film preparations	Difficult for mass production; the quality of materials is sensitive to experimental conditions; inevitable use of volatile solvents
EIAA	Metal oxides; carbons	Discrete particles with spherical or cylindrical mesopores	Tolerant to aqueous solution; controllable evaporation process; accessible to discrete particles	Time consuming; the quality of materials is sensitive to experimental conditions; inevitable use of volatile solvents
Solution-based nanoprecipitation	Carbons; metal oxides; metals; hybrids (carbon/metal, carbon/metal carbides, *etc.*)	Discrete particles with spherical, cylindrical, or bicontinuous pore structures; free-standing nanosheets with spherical mesopores; monoliths with spherical or cylindrical mesopores	Large-scale production; applicable to aqueous solution synthesis; short time of preparation; easily accessible to discrete particles of tunable morphologies and various pore structures	A lot of factors affecting material morphology and pore structure; hard to predict a specific morphology
Interfacial self-assembly	Carbons; conducting polymers; metal oxides; metals; hybrids (carbon/metal, carbon/metal oxides, carbon/metal carbides, conducting polymer/metal oxides, *etc.*)	1D–3D materials with spherical, cylindrical or hierarchical pore structures	Applicable to diverse structural templates; tunable dimensions and morphologies of materials; easily accessible to free-standing 2D porous nanosheets; easy construction of heterojunction structures	Complex interactions among precursors, BCP micelles, and substrates; surface modifications of the substrates are usually required
Emulsion-template	Carbons; conducting polymers	Discrete particles (especially anisotropic particles) with spherical, cylindrical or hierarchical pore structures	Large-scale production; accessible to anisotropic particles and hierarchical structures; easy removal of the emulsion template	Emulsion template is sensitive to experimental parameters; complex mechanisms of particle formations; difficult to predict a specific morphology

can be quenched at temperatures much lower than T_g. Subsequently, mesoporous carbons can be obtained by pyrolysis of the BCPs with ordered microphases at high temperatures (generally 800–1000 °C) under inert atmosphere. In this method, the BCP precursors require a carbon-rich block (usually containing sp or sp^2-hybridized carbon atoms), which can form continuous domains after the phase separation.[86] For example, Matyjaszewski and coworkers reported a one-pot approach towards mesoporous nitrogen-doped carbons *via* the pyrolysis of polyacrylonitrile-*block*-poly(*n*-butyl acrylate) (PAN_{128}-*b*-PBA_{76}, the subscript numbers denote the degrees of polymerization of the blocks).[87] First, the PAN_{128}-*b*-PBA_{76} copolymer was annealed at 280 °C in air, which led to the nanophase separation of the copolymer and cyclization of PAN side chains. Subsequently, the pyrolysis of this polymer at 500–800 °C under inert atmosphere resulted in the carbonization of the PAN domain and the removal of the PBA block, thereby generating mesoporous N-doped carbon (Fig. 3a).[87] The mesopore size of the resulting porous carbon increased with an increase in the length of the pore-forming PBA block (Fig. 3b).[88] On the other hand, the pore connectivity was reduced with a decrease in the molar mass of the copolymers, which was attributed to the weaker phase segregation between the blocks of shorter lengths (Fig. 3c).[56] On the basis of similar principles, a variety of mesoporous carbon materials with spherical and cylindrical pore structures have been prepared by using other BCPs containing PAN blocks as soft templates, such as PAN-*b*-poly-(methyl methacrylate) (PAN-*b*-PMMA),[89–93] PAN-*b*-poly(*tert*-butyl acrylate) (PAN-*b*-P*t*BA),[94] and PAN-*b*-polystyrene (PAN-*b*-PS).[95]

3.2 Solvent evaporation-induced self-assembly

EISA is a versatile strategy towards a diversity of mesoporous materials in addition to carbons. The EISA protocol is based on the cooperative self-assembly of BCPs and specific precursors that can form the pore walls in the process of solvent evaporation, as illustrated in Fig. 4.[23,40,96] Typically, in solutions, BCP chains interact with the soluble precursors *via* intermolecular interactions, such as hydrogen bonding and electrostatic interactions. During the solvent evaporation, the cooperative self-assembly of the precursors (*e.g.*, carbon sources or metal alkoxides) with BCPs generates a microphase separation. Then, a continuous network is formed by condensation or cross-linking of the precursors. These reactions may happen simultaneously or after the self-assembly process. Finally, the BCP template can be removed by calcination or solvent extraction, producing a mesoporous architecture. As the mesopores and walls are templated by the different blocks of BCPs, the pore dimension and wall thickness can be simply regulated by modifying the block lengths of the sacrificial BCPs.

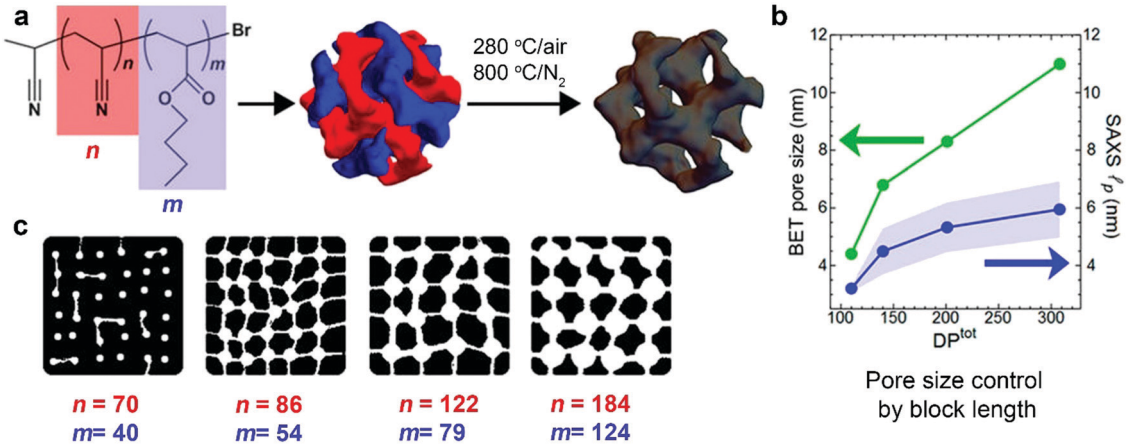

Fig. 3 Fabrication of mesoporous carbons by the self-assembly of PAN-*b*-PBA copolymers in the bulk. (a) Synthetic route towards mesoporous nitrogen-enriched nanocarbons. (b) Pore sizes from the Brunauer–Emmett–Teller (BET) method (green) and inhomogeneity lengths from small-angle X-ray scattering (SAXS) (blue) of nitrogen-enriched nanocarbons prepared by the pyrolysis of BCPs with different total degrees of polymerization. (c) Relationship between the mesopore connectivity and the molecular weight of BCPs. (a–c) Reproduced with permission.[88] Copyright 2017, American Chemical Society.

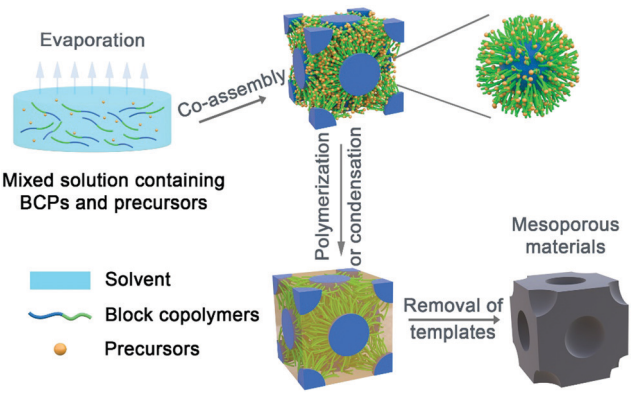

Fig. 4 Scheme illustration of a typical EISA process for the synthesis of mesoporous materials using BCPs as the soft template.

In 1994, Ogawa *et al.* first demonstrated the preparation of silica–surfactant composite films by EISA,[97] in which an aqueous mixture solution of alkyltrimethylammonium bromide and tetramethoxysilane was spin-coated on a glass substrate and dried in air at 100 °C to remove the solvent and to promote condensation of the silica. As a result, thin films with ordered phase structures were formed on the substrates. This work first demonstrated the feasibility of the EISA method for preparing ordered mesophases.[97] Afterwards, Brinker and co-workers synthesized ordered mesoporous silica by the EISA method.[98] They evaporated the precursor solutions, which were prepared by adding a cationic surfactant, cetyltrimethylammonium bromide (CTAB), to an ethanol solution containing polymeric silica sols and tetraethylorthosilicate (TEOS). Following calcination, continuous silica films with cubic and hexagonal mesoporous structures were obtained.[98] Although low-molecular-weight surfactants can be used to prepare ordered mesoporous materials, the resulting pore size is usually small and limited in the range of 2–8 nm. In 1997, Wiesner's group prepared mesoporous ceramics by using high-molecular-weight lab-made BCPs as soft templates (Fig. 5).[39] They employed PI-*b*-PEO diblock copolymers along with inorganic precursors including 3-glycidyloxypropyl-trimethoxysilane (GLPMO) and aluminum *sec*-butoxide ($Al(OBu^s)_3$), which were first dissolved in a 1:1 mixed solvent of chloroform and tetrahydrofuran (THF). The subsequent solvent evaporation and calcination produced mesoporous aluminosilicates with cylindrical or lamellar morphology depending on the weight ratio of the inorganic precursors to BCP. The pore sizes were adjustable in the window of 10–50 nm by tailoring the molar mass of PI-*b*-PEO between 10 000 and 100 000 g mol^{-1}.[39]

After the achievements in mesoporous ceramics, in 1998 Yang *et al.* extended the BCP-templated method to the synthesis of mesoporous metal oxides.[75] They employed Pluronic P123 as pore-forming agents in non-aqueous solutions containing inorganic metal chlorides as the metal precursors (Fig. 5). A library of ordered mesoporous metal oxides (TiO_2, ZrO_2, Al_2O_3, Nb_2O_5, TaO_5, WO_3 and SnO_2) and mixed oxides ($SiAlO_{3.5}$, $SiTiO_4$, $ZrTiO_4$, Al_2TiO_5, and ZrW_2O_8) were synthesized (Fig. 5).[75] Although these metal oxides with large pore sizes (up to 14 nm) could be obtained in their study, the resulting metal oxides were mostly amorphous with poorly-crystallized walls.[75] In order to overcome this limitation, Wiesner and co-workers developed a facile EISA method based on combined self-assembly by soft and hard chemistries, simply referred to as "CASH", in 2008.[41] They applied PI-*b*-PEO copolymers with PI blocks containing sp^2-hybridized carbons as the pore-forming agents (Fig. 5). During the heating process, the sp^2 carbons of the PI blocks (soft) were converted to sturdy, amorphous carbons (as hard templates) under inert environment, which could prevent the collapse of the mesoporous structure during the high-temperature crystallization. Through the CASH method, mesoporous TiO_2 and Nb_2O_5 with highly crystalline walls were synthesized.[41] In 2003, Zhao and co-workers extended the fabrication of mesoporous materials to multicomponent mesostructured minerals by introducing an "acid–base pairs" concept, which addressed the effect of the inorganic–inorganic interplay on the preparation of mesoporous

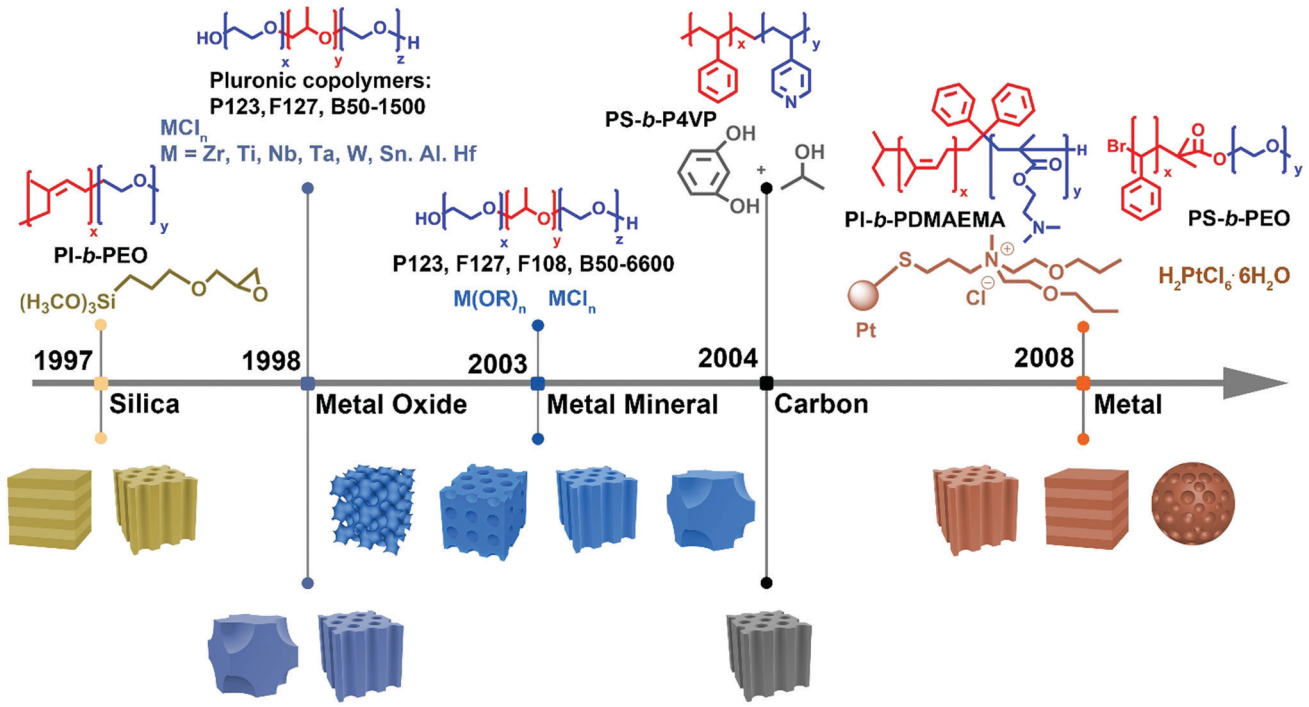

Fig. 5 Historical development of mesoporous materials synthesized by the EISA method using different BCPs as the structure-directing agents.

materials (Fig. 5).[99] They classified various metallic and non-metallic sources in terms of their relative acidity and alkalinity on solvation. Using suitable pairs, the pH of the system can be self-adjusted without the addition of extra reagents. This work provided a new principle to regulate the hydrolysis rate of metallic/non-metallic precursors, which gave birth to several new types of mesoporous materials, including mixed metal oxides, metal phosphates, and metal borates.[99]

Apart from inorganic materials, organic mesostructures and carbon materials can be synthesized by EISA based on organic–organic self-assembly. In 2004, Dai and colleagues first prepared ordered mesoporous carbon materials by using polystyrene-*b*-poly(4-vinylpyridine) (PS-*b*-P4VP) as the structure-guiding agent and resorcinol–formaldehyde as the carbon-rich source (Fig. 5).[100] The PS-*b*-P4VP copolymer and resorcinol monomers co-assembled into an ordered structure by annealing at 80 °C in *N*,*N*′-dimethylformamide (DMF)/benzene mixed vapor. Then, the nanostructure was stabilized *via in situ* polymerization of the resorcinol monomers by treatment of formaldehyde gas. The subsequent pyrolysis of the polymeric film under inert atmosphere generated a hexagonal carbon-channel array.[100] Later, Zhao's group extended the organic carbon precursors to low-molecular-weight phenolic resins (resol), which could be polymerized at low temperatures without using formaldehyde gas.[101] Nowadays, resol has become one of the most commonly used carbon precursors for the preparation of porous carbon materials.

After carbon-based materials, the EISA strategy was successfully applied for the synthesis of mesoporous metals. Wiesner and colleagues first reported the preparation of porous platinum mesostructures using platinum-rich nanoparticles (NPs) stabilized with ionic liquid ligands as the platinum precursor and PI-*b*-poly(dimethylaminoethyl methacrylate) (PI-*b*-PDMAEMA) as the structure-directing agent (Fig. 5).[78] They dissolved the ligand-stabilized platinum nanoparticles (PtNPs) and the BCPs in a chloroform/methanol mixture. The resulting solution was evaporated slowly to generate a metal-rich mesostructured PtNP–BCP hybrid. Then, the Pt–C composite was obtained by heating this hybrid under inert atmosphere. Finally, the carbon domains in the materials were removed by Ar–O plasma or acid-etching, yielding ordered mesoporous platinum with lamellar or inverse hexagonal mesostructures.[78] In addition to metal-rich NPs as the metal precursors, inorganic metal salts can be an alternative. Yamauchi and co-workers constructed a mesoporous platinum framework consisting of connected NPs using polystyrene-*b*-poly(ethylene oxide) (PS-*b*-PEO) as the soft template (Fig. 5).[102] They drop-coated a THF solution of PS_{37}-*b*-PEO_{110} and hydrogen hexachloroplatinate(IV) hexahydrate ($H_2PtCl_6{\cdot}6H_2O$) onto an indium tin oxide substrate. After THF evaporation, the obtained yellow film was placed in a three-electrode system for electrochemical deposition of Pt. The BCP template was eliminated by repeated washing with organic solvents, producing mesoporous Pt with closely-connected giant mesocages.[102]

In general, the EISA method is not applicable to water-containing systems and the resulting materials typically have a film-like morphology. Deng *et al.* established a solvent evaporation-induced aggregating assembly (EIAA) approach, by which mesoporous materials of various morphologies can be obtained in aqueous solutions (Fig. 6).[103–106] For instance, they utilized poly(methyl methacrylate)-*b*-poly(ethylene oxide) ($PMMA_{174}$-*b*-PEO_{125}) as the pore-forming agent and TEOS as the silica precursor in an acidic THF–H_2O mixture.[103] During the evaporation of THF, the self-assembly process occurred at the liquid–liquid

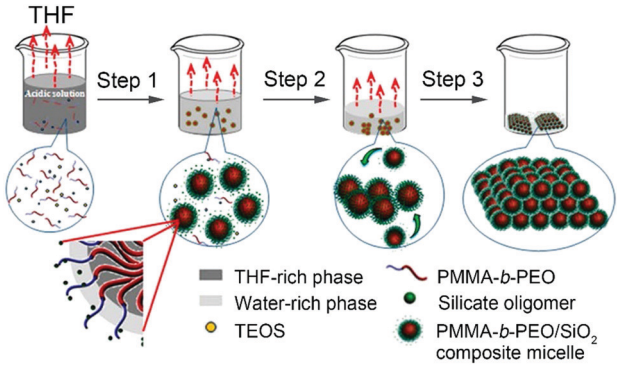

Fig. 6 Illustration of a typical EIAA process in the synthesis of mesoporous materials (silica as an example). Reproduced with permission.[103] Copyright 2011, American Chemical Society.

interface and granular SiO_2/PMMA-*b*-PEO composites with crystal-like morphology were formed. Following calcination, SiO_2 particles with face centered cubic (fcc) mesostructures and large pore dimensions (up to 37 nm) were achieved.[103] Different from the EISA method, in which an ordered mesostructure is formed at the substrate–liquid interface at the final stage of solvent evaporation,[107] the self-assembly process of EIAA occurs in the solution at an early stage. In this way, the EIAA method facilitates the construction of mesoporous materials with variety of architectures, such as particle, sphere or rod-like morphology. Later, they extended the EIAA concept to carbon materials and they obtained ordered mesoporous carbon nanofibers with cylindrical pores.[40]

In principle, EISA and EIAA are similar to the self-assembly of BCPs in the bulk, as the slow evaporation of the volatile solvent drives the aggregation of the BCPs or their aggregates to closely pack into various ordered morphologies, depending on the packing parameters.[23,37] By virtue of the microphase separation mechanism of BCPs, EISA and EIAA are powerful strategies for preparing mesoporous materials with various well-defined pore structures, including closely-packed spherical pores, hexagonally packed cylindrical pores, bicontinuous structures, *etc.* The remainder of this subsection concentrates on the discussions of pore structure engineering.

3.2.1 Spherical pore structures. In the EISA process, BCPs and precursors can microphase separate into closely-packed spheres with appropriate packing parameters ($p < 1/3$) after solvent evaporation, including disordered packing, face centered cubic (fcc) (space group $Fm\bar{3}m$), body centered cubic (bcc) (space group $Im\bar{3}m$), and 3D hexagonally packed structures (space group $P6_3/mmc$),[37,107] which have been the most common structures achieved thus far. These structures can be solidified by the cross-linking of the precursors and converted to mesoporous materials by removing the BCPs during the solvent extraction process or through high-temperature pyrolysis. Mesoporous materials with spherical pores, which have been reported in the past 10 years, are summarized in Table 2,[42,108–119] while those reported prior to 2010 have been covered by several related review articles.[1,23,61,70,107]

The disordered pore structure lacks a long-range ordered structure. However, the utilization of BCPs as soft templates can enable the attainment of uniform pore sizes and high SSAs. Furthermore, the pore size can be tuned by changing the molar mass of BCPs. For example, mesoporous TiO_2 with randomly packed spherical mesopores was synthesized using a poly(ethylene oxide)-*b*-polybutadiene-*b*-poly(ethylene oxide) (PEO-*b*-PB-*b*-PEO) triblock copolymer and $TiCl_4$ (titania precursor) in an ethanol–water mixed solution.[120] Mesoporous TiO_2 films were prepared by dip-coating the precursor solutions onto Si substrates. After solvent evaporation, the films were dried at 80 °C and subsequently calcined at 475 °C to remove the BCP template. The pore dimension of the resulting mesoporous TiO_2 film could be tailored by varying the molar mass of the copolymer with a constant PB/PEO weight ratio. The obtained TiO_2 displayed a randomly packed spherical pore structure with pore sizes in the range of 7.6–16.6 nm and SSAs of 85–328 $m^2\ g^{-1}$.[120] In addition to this report, a number of other mesoporous materials with randomly packed spherical pores have also been prepared in the last decade, including TiO_2,[121–123] Al-doped TiO_2,[124] Nd-doped TiO_2,[125] TiO_2/carbon,[126] IrO_2,[127] $FePO_4$,[128] $NiFe_2O_4$,[129] N-doped carbon,[96] $LiFeO_4$/carbon,[130] *etc.*, using PS-*b*-poly(acrylic acid) (PS-*b*-PAA),[96] PI-*b*-PEO,[124–126,130] PS-*b*-PEO,[121] and PS-*b*-poly(2-vinylpyridine)-*b*-PEO (PS-*b*-P2VP-*b*-PEO)[122,128,129] as soft templates.

The fcc structure is a common feature of ordered closely-packed spherical pore architecture, which has a $Fm\bar{3}m$ space group. The preparation of ordered pore structures, which requires an ordered packing of BCP/precursor composite micelles during EISA, needs delicate control and thus, is more difficult than the fabrication of disordered pore structures. A major difficulty lies in the control of the hydrolysis and condensation of precursors.[23,40,99] To overcome this difficulty, a number of approaches have been developed.[75,99,131] Zhao and co-workers established an effective ligand-assisted method to synthesize ordered mesoporous oxide materials. For instance, they employed PS-*b*-PEO diblock copolymer and tungsten chloride (WCl_6) as the soft template and tungsten precursor, respectively, with the assistance of acetylacetone to slow down the hydrolysis and condensation of the tungsten precursor (Fig. 7a).[116] When a THF solution of PS-*b*-PEO was mixed with an ethanolic solution of WCl_6 and acetylacetone (AcAc), $WCl_{6-x}(AcAc)_x$ compounds were formed owing to the strong coordination of AcAc with W^{6+} ions, which slowed down the hydrolysis process. Following evaporation of the solvent, mesoporous WO_3 with an ordered $Fm\bar{3}m$ symmetry was achieved (Fig. 7b and c). The porosity could be tailored by changing the PS block length. The resulting mesoporous WO_3 materials exhibited tunable pore diameters in the range of 10.6–15.3 nm, pore volumes of 0.13–0.17 $cm^3\ g^{-1}$, and SSAs of 76–136 $m^2\ g^{-1}$.[116] Other typical mesoporous materials with the fcc structure are also summarized in Table 2.

When the proportion of the hydrophobic block increases, the interface curvature of the micelles will reduce, resulting in mesophase transformation from fcc to a looser packing mode, namely the bcc structure, which is another common type of ordered spherical pore architecture.[107,132] Table 2 lists some representative mesoporous materials with bcc mesostructures, which were reported in the last decade. For instance, Wei *et al.* fabricated N-doped mesoporous carbon using dicyandiamide and resol as the carbon

Table 2 Summary of mesoporous materials prepared by EISA over the recent 10 years[a]

Pore structure	Symmetry	Product	Template	Pore size (nm)	V_t[b] ($cm^3\ g^{-1}$)	S_{BET}[c] ($m^2\ g^{-1}$)	Ref.
Spherical	$Fm\bar{3}m$	Carbon	PEO-*b*-PMMA-*b*-PS	19.4–20.0	~0.6	~900	108
		CoO_x-doped carbon	PS-*b*-PEO	13.4–16.0	0.41–0.48	394–483	115
		WO_3	PS-*b*-PEO	10.9	—	121	42
		WO_3	PS-*b*-PEO	21.7	—	70.4	114
		WO_3	PS-*b*-PEO	10.1–12.5	0.21–0.32	112–128	119
		WO_3	PS-*b*-PEO	10.6–15.3	0.13–0.17	76–136	116
		Rare earth oxide	PIB-*b*-PEO	17–42	—	—	111
	$Im\bar{3}m$	N-Doped carbon	F127	3.9–17.6	0.27–0.47	503–548	112
			F127	2.98–3.06	0.32–0.36	604–645	113
	$P6_3/mmc$	TiO_2/g-C_3N_4	PS-*b*-PEO	18	0.338	76	117
		SnO_2	PS-*b*-PEO	18	—	98	118
	Primitive cubic	TiO_2	PS-*b*-PEO	16.0	0.21	112	109
Cylindrical	*p6mm*	Carbon	PS-*b*-PEO	26.2	0.49	555	106
		Carbon	F127	2.6–3.8	0.23–0.47	364–888	146
		N-Doped carbon	F127	3.3	0.26	450	148
		N,P-Codoped carbon	PS-*b*-PEO	26–38	—	1020–1110	144
		Carbon/silica	PS-*b*-PEO	26–34	—	372–472	142
		Sn/carbon/silica	PS-*b*-PEO	17.3–17.4	0.25–0.36	408–427	143
		N/TiO_2-carbon	F127	3.6–4.8	0.22–0.27	319–342	149
		TiO_2	PS-*b*-PEO	—	—	—	139
		TiO_2	F127	5.7; 10–30	0.164	112	145
		TiO_2	P123	9.8	0.52	370	141
		Black-TiO_2	P123	9.6	0.24	124	137
		TiO_2/silica	P123	2.6	0.156	145	151
		Yb,Tm/TiO_2	F127	3–5	—	44–113	140
		ZrO_2	F127	6.2	0.06	56	138
		In_2O_3	PS-*b*-PEO	14.5	0.22	48	150
		SnPi	F127	7.4	—	310	147
Bicontinuous	$Ia\bar{3}d$	Carbon	PI-*b*-PS-*b*-PEO	11–39	0.24–1.56	172–606	155
		Carbon	PI-*b*-PS-*b*-PEO	15–39	0.89–1.56	202–692	159
		Carbon	PI-*b*-PS-*b*-PEO	—	—	—	161
		N-Doped carbon	PCL-*b*-PEO	11.8	0.59	620	162
		TiO_2/carbon	PI-*b*-PS-*b*-PEO	—	—	—	157
	$I4_132$	Carbon	PI-*b*-PS-*b*-PEO	31	1.41	348	159
		Carbon	PI-*b*-PS-*b*-PEO	31–35	1.04–2.01	348–588	155
		Carbon	PI-*b*-PS-*b*-PEO	—	—	—	161
		Nb_2O_5	PI-*b*-PS-*b*-PEO	—	—	—	154
		$CsTaWO_6$	PI-*b*-PS-*b*-PEO	42	—	37	164
		NbN	PI-*b*-PS-*b*-PEO	16–31	0.41–1.01	59–111	160
		$Ti_{0.5}Nb_{0.5}N$	PI-*b*-PS-*b*-PEO	15	—	—	158
		Pt/Au NPs	PI-*b*-PS-*b*-PDMAEM	—	—	—	156
	$I4_1/amd$	TiO_2	DNPE-PEO-*b*-PS	—	—	—	163
	$Pn\bar{3}m$	Al_2O_3	PMMA-*b*-PEO	72.8	0.34	52	165

[a] Information on mesoporous materials reported before 2010 is covered by several related review articles (*e.g.* ref. 1, 23, 61, 70 and 107). [b] V_t: total pore volume. [c] S_{BET}: SSAs calculated from nitrogen adsorption–desorption isotherms by the BET equation.

sources and Pluronic F127 as the structure-templating agent.[112] The resulting carbon materials showed an ordered bcc mesoporous structure with an $Im\bar{3}m$ symmetry (q^2 ratio: 1 : 2 : 3). By altering the mass ratio of dicyandiamide to resol, the mesoporous carbons showed tunable pore sizes of 3.9–17.6 nm, pore volume of 0.27–0.47 $cm^3\ g^{-1}$, and SSAs of 500–548 $m^2\ g^{-1}$.[112]

In addition to fcc and bcc mesostructures, many mesoporous materials exhibit 3D hexagonal mesostructures, in which spherical pores are hexagonally arranged with a $P6_3/mmc$ space group (Fig. 7d). For example, Deng *et al.* prepared ordered SnO_2 materials with hexagonal mesostructures using PS-*b*-PEO as the template and $SnCl_4$ as the tin oxide precursor.[118] They employed acetylacetone as a chelating agent of $SnCl_4$ in order to slow the aggregation of SnO_2 nanoclusters formed by the initial hydrolysis of $SnCl_4$. The obtained SnO_2 displayed a hexagonal mesostructure with a space group of $P6_3/mmc$ (Fig. 7e and f). It had a uniform pore size of 18 nm and an SSA of 98 $m^2\ g^{-1}$.[118]

3.2.2 Cylindrical pore structures. BCPs are able to form cylindrical structures in the packing parameter range of 1/3 to 1/2.[37] Such templates can be used to synthesize porous materials with cylindrical pore channels, including disordered wormhole-like pores and ordered hexagonally packed structures. Disordered cylindrical pore structures usually present as wormhole-like mesostructures or short-range ordered nanochannels. Compared to spherical pores, wormhole-like pores are usually harder to achieve as cylindrical micelles are more difficult to obtain than spherical micelles by the self-assembly of BCPs in solutions, because their formation requires one-dimensional (1D) fusion of spherical micelles.[133,134] Prior to 2010, many studies focused on the synthesis of mesoporous materials with single components, primarily carbons and metal oxides. Over the last decade, mesoporous materials with wormhole-like pores have been extended to composite/hybrid materials for combining the advantages of different functional materials. For instance, Lee and colleagues

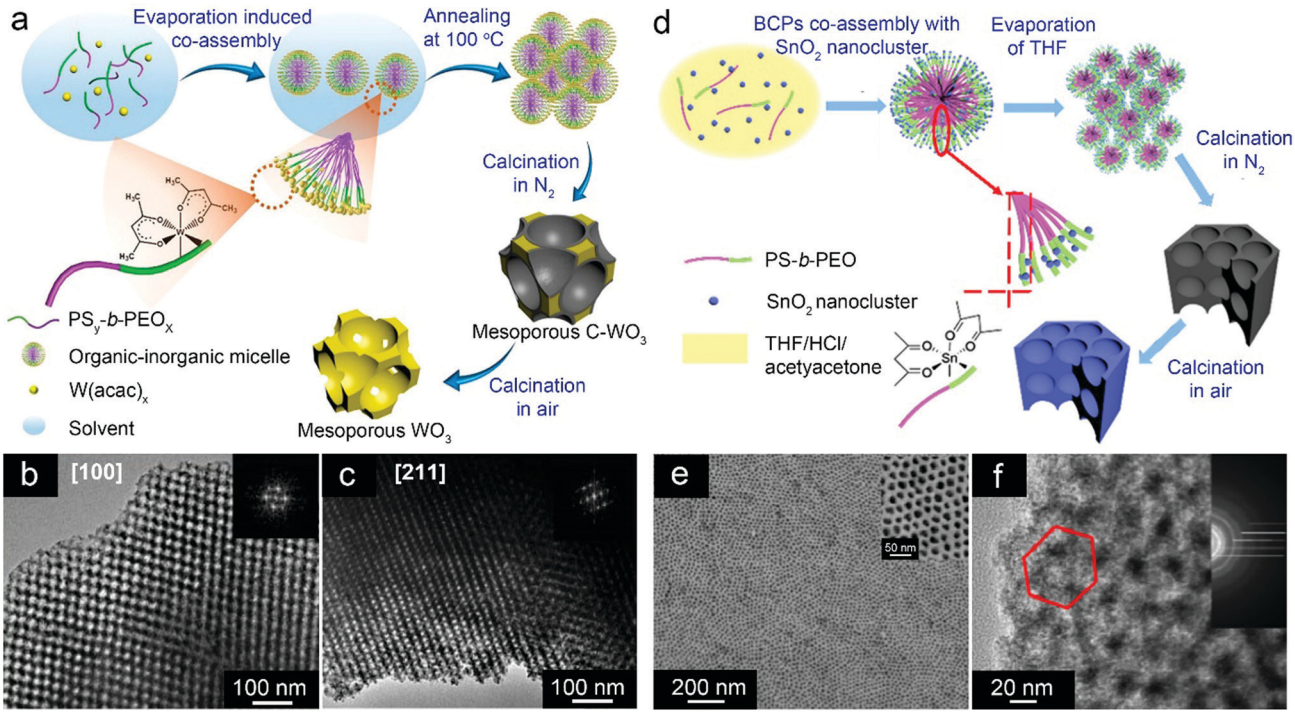

Fig. 7 Typical examples of mesoporous materials with spherical pore structures prepared by EISA. (a) Synthetic route towards ordered mesoporous WO_3 with an fcc structure. (b and c) TEM images of the ordered mesoporous WO_3 recorded from (b) [100] and (c) [211] directions, respectively. (a–c) Reproduced with permission.[116] Copyright 2017, American Chemical Society. (d) Synthetic route of ordered SnO_2 with a $P6_3/mmc$ symmetry. (e) SEM image of the ordered mesoporous SnO_2. The inset shows a high-magnification SEM image. (f) TEM image of the ordered mesoporous SnO_2. The inset shows a corresponding selected-area electron diffraction (SAED) pattern. The red hexagon marks the hexagonal array of the mesopores. (d–f) Reproduced with permission.[118] Copyright 2018, American Chemical Society.

synthesized mesoporous Ge/GeO_2/carbon hybrid materials with disordered cylindrical channels using PS-*b*-PEO as the template along with resol and $Ge(OEt)_4$ as the carbon and Ge/GeO_2 precursors, respectively (Fig. 8a).[135] Resol could interact with the PEO block *via* hydrogen bonding, while hydrophilic $GeO_x(OH)_y$ moieties were generated during the hydrolysis of the Ge precursor, which could mix well with the PEO block. The as-made hybrid material was carbonized at 600 °C under argon atmosphere, yielding a mesoporous GeO_2/C composite. After the thermal reduction of the GeO_2/carbon composite under 4% H_2/Ar atmosphere at 600 °C, mesoporous Ge/GeO_2/carbon hybrid with a wormhole-like pore structure was obtained (Fig. 8b), with an average pore size of 44 nm and an SSA of 89 $m^2\ g^{-1}$.[135] In addition to this report, other mesoporous materials with wormhole-like pore structures were also prepared in the last decade, including Li_4TiO_{12}[136] and TiO_2/carbon,[126] using PI-*b*-PEO as the soft template.

An ordered cylindrical pore structure is typically generated by hexagonally packed cylindrical mesopores with a *p6mm* space group. Fu and co-workers reported the preparation of porous black TiO_2 with an ordered hexagonal mesostructure *via* an ethylenediamine encircling process, followed by hydrogenation (Fig. 8c).[137] They employed the co-assembly of Pluronic P123 and tetrabutyl titanate (TBT) in an acidic ethanol solution upon solvent evaporation. After calcining the sample at 350 °C under N_2 atmosphere and subsequently at 700 °C in air, the as-made mesoporous TiO_2 showed a 2D ordered hexagonal structure with a *p6mm* symmetry (q^2 ratio = 1 : 3 : 4) (Fig. 8d and e). Mesoporous black TiO_2 was further prepared by calcining the as-made mesoporous TiO_2 under H_2 flow at 500 °C for 3 hours, which had a large pore size of 9.6 nm, a pore volume of 0.24 $cm^3\ g^{-1}$, and a high SSA of 124 $m^2\ g^{-1}$.[137] Other examples of ordered mesoporous materials with hexagonally packed cylindrical pores are summarized in Table 2.[106,126,136,138–151]

3.2.3 Bicontinuous structures. As the packing parameter increases to $p > 1$, bicontinuous structures can be formed in the EISA process of BCPs and precursors.[37,38] Bicontinuous mesoporous materials have drawn tremendous interest in light of their triply periodic minimal surfaces (TPMSs) and the presence of 3D continuous pores, which facilitate smooth mass transport in all directions and the maximum utilization of active sites in the materials.[5,152] These features are highly desirable in ESC applications. Ordered bicontinuous structures are generally divided into three basic categories, including the Schoen gyroid (G), the Schwarz diamond (D), and the Schwarz primitive (P) surfaces (Fig. 9). These minimal surfaces separate the space into two intertwined labyrinths on both sides.[152] Therefore, they are also called double gyroid (DG), double diamond (DD), and double primitive (DP) structures. It is quite difficult to obtain bicontinuous structures because of their very narrow phase region in the

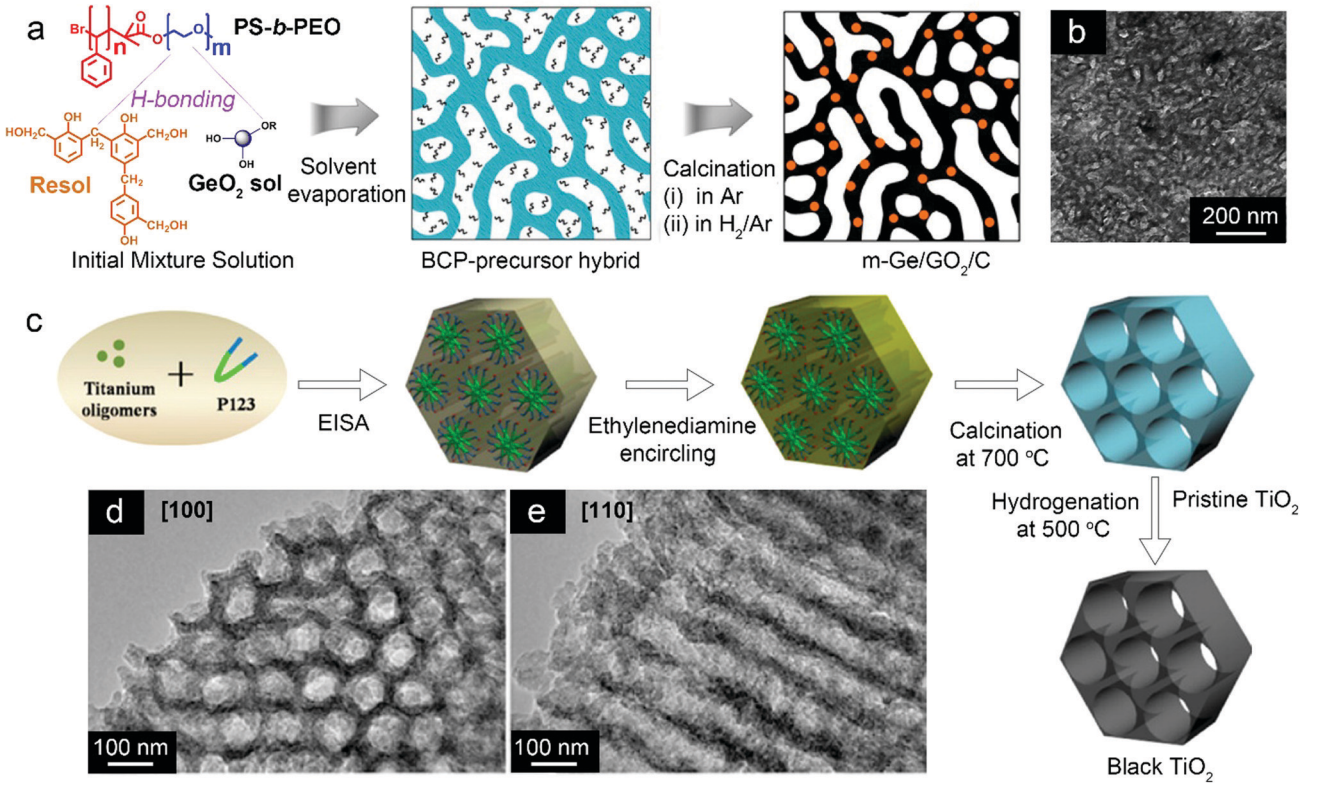

Fig. 8 Typical examples of mesoporous materials with cylindrical pore structures prepared by EISA. (a) Synthetic route towards mesoporous Ge/GeO_2/carbon composites (m-Ge/GeO_2/C). (b) TEM image of m-Ge/GeO_2/C. (a and b) Reproduced with permission.[135] Copyright 2015, American Chemical Society. (c) The formation process of ordered mesoporous black TiO_2. (d and e) TEM images of ordered mesoporous TiO_2 along (d) [100] and (e) [110] directions, respectively. (d and e) Reproduced with permission.[137] Copyright 2014, American Chemical Society.

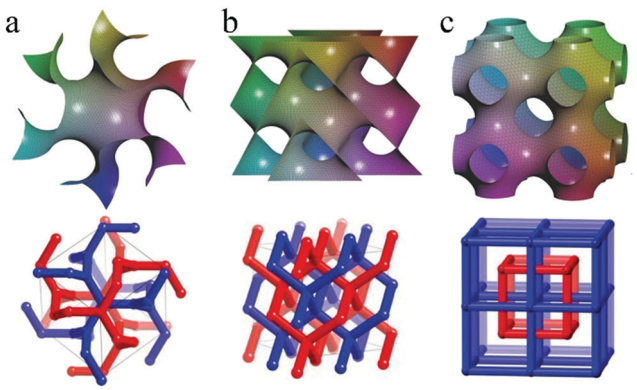

Fig. 9 Schematic drawings and skeletal graphs of triply periodic minimal surfaces. (a) G surface, (b) D surface and (c) P surface. Reprinted with permission.[152] Copyright 2018. Wiley-VCH.

morphological phase diagram of BCP self-assembly and the difficulties in finding appropriate self-assembly conditions. Typical examples of ordered bicontinuous mesoporous materials are listed in Table 2.[153–165]

3.2.3.1 Gyroid structure. Among the different ordered bicontinuous architectures, gyroidal structure is relatively easy to obtain, which makes it a common morphology in bicontinuous mesoporous materials.[152] This structure separates two intertwined frameworks with three-coordinate connectivity (Fig. 9a). Since the first report on mesoporous SiO_2 with a gyroid structure, namely MCM-48,[166] tremendous efforts have been devoted to the fabrication of bicontinuous mesoporous materials. To date, various mesoporous materials with gyroid structures, including carbons,[155,159,161,162,167] metal oxides,[154,157,164] metal nitrides,[158,160] and even pure metals[78,156] have been synthesized. There are two types of gyroidal structures in the self-assembly of BCPs, including double gyroid (G^D) and alternating gyroid (G^A) structures.[155,156] The two networks are composed of the same materials in the G^D structure, which is accessible *via* diblock copolymers, while the two networks are different materials in the G^A structure, which is only available *via* triblock terpolymers. In 2014, Wiesner and co-workers demonstrated tunable synthesis of gyroidal mesoporous carbons by EISA of triblock terpolymer PI-*b*-PS-*b*-PEO (ISO) and resol (Fig. 10a).[155] They successfully synthesized two gyroidal mesoporous carbon materials, including double gyroid mesoporous carbon (G^DMC) (Fig. 10b) and alternating gyroid mesoporous carbon (G^AMC) (Fig. 10c). The triblock terpolymer with a PEO volume fraction of *ca.* 50 vol% led to the formation of G^DMC with an $Ia\bar{3}d$ symmetry, while the terpolymer with a very small PEO volume fraction of 4.9 vol% gave rise to G^AMC with an $I4_132$ symmetry (q^2 ratio: 3 : 4 : 6 : 7 : 8). They found that the alternating gyroid structure can provide more pore volume compared to the double gyroid counterpart. The largest pore volume of G^DMC was 1.56 $cm^3\ g^{-1}$, with a uniform pore size of

39 nm and a high SSA of 682 $m^2 g^{-1}$. In comparison, the largest pore volume of G^AMC was 2.01 $cm^3 g^{-1}$, with a uniform pore size of 35 nm and an SSA of 588 $m^2 g^{-1}$.[155]

Later, highly ordered mesoporous metals comprising single or binary metal NPs with alternating gyroid structures were successfully synthesized. Polyisoprene-*b*-polystyrene-*b*-poly(*N*,*N*-dimethylamino)ethyl methacrylate (PI-*b*-PS-*b*-PDMAEMA) terpolymers were employed as the structure-directing agents and ligand-stabilized Pt or Au NPs were utilized as the metal precursors (Fig. 10d).[156] They found that the ligands of the metal NPs could govern the BCP/NP self-assembly and tailoring the ligands of binary metal NPs could enable control over the NP spatial arrangement in the 3D structures (Fig. 10e). The synthesized polymer/NP hybrids showed an $I4_132$ symmetry with a $(q/q_{100})^2$ ratio of 2 : 6 : 8 : 10 : 12 : 14 : 16 : 18 : 20 : 22 : 24 : 26 : 30 : 32 : 34, with q_{100} being the reciprocal vector. This work provided important clues for the preparation of metallic systems with bicontinuous mesoporous structures.[156] To date, gyroid structures have also been demonstrated in many metallic compounds, including TiO_2,[157] Nb_2O_5,[154] $CsTaWO_6$,[164] $Ti_{0.5}Nb_{0.5}N$,[158] and NbN[160] (Table 2).

3.2.3.2 Diamond structure. The diamond (D) surface structure separates space into two intertwined diamond networks. Each network has a tetrahedral connectivity, as shown in Fig. 9b.[152] However, this bicontinuous structure has been rarely reported, with several successful cases exclusively in SiO_2,[168] TiO_2,[163] and Al_2O_3.[165] In 2014, Che's group employed a laboratory-made amphiphilic triblock terpolymer, poly(*tert*-butyl acrylate)-*b*-PS-*b*-PEO (PtBA-*b*-PS-*b*-PEO, ASO), as the soft template and TEOS as the silica precursor, and they obtained ordered mesoporous silica with a double diamond structure.[168] The mesoporous silica had a symmetry of $I4_1/amd$ (q^2 ratio: 3 : 8 : 11 : 12 : 16 : 19) and a tetragonal rather than a cubic structure. The two sets of frameworks were adhered to each other, demonstrating a shifted double diamond structure. This is because the evaporation of THF and water led to the two frameworks losing the mutual support and the original cubic symmetry could not be maintained. Hence, the two frameworks shifted and attached to each other.[168] In another study, they synthesized a shifted double diamond TiO_2 scaffold using the linear dinonylphenyl end-capped PS-*b*-PEO copolymer (DNPE-PEO-*b*-PS) as the soft template and titanium diisopropoxide bis(acetylacetonate) (TIA) as the Ti source (Fig. 11a).[163] The shifted double diamond TiO_2 showed an $I4_1/amd$ symmetry with a q^2 ratio of 3 : 8 : 11 (Fig. 11b–d), which exhibited a complete bandgap by shifting 0.332c with a high dielectric contrast of TiO_2 and thus provided an opportunity for the development of new optical devices.[163] In 2018, Zhao' group extended DD-structured materials to γ-Al_2O_3 *via* vesicle-aggregation-assembly approach using PMMA-*b*-PEO as the soft template and aluminum isopropoxide as the Al_2O_3 precursor.[165] The Al^{3+}-based gel/polymer composite microspheres were obtained *via* the co-assembly between aluminum precursor molecules and PEO segments of

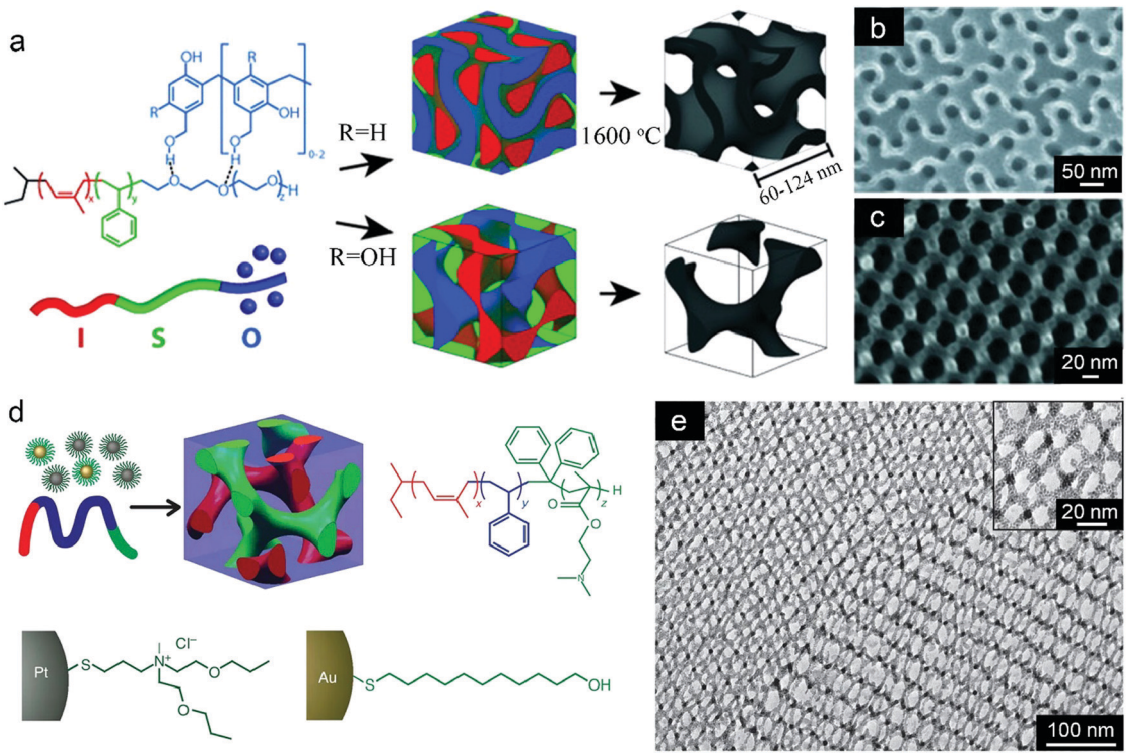

Fig. 10 Typical examples of mesoporous materials with gyroid structures. (a) Synthesis of gyroidal mesoporous carbons with two types of gyroidal structures. (b) TEM image of the ordered mesoporous carbon with a double gyroid structure. (c) TEM image of the ordered mesoporous carbon with an alternating gyroid structure. (a–c) Reproduced with permission.[155] Copyright 2014, American Chemical Society. (d) Schematic illustration of triblock terpolymer-binary Pt and AuNP self-assembly. (e) TEM image of the ordered porous gyroidal network of the binary metal NPs. (d and e) Reproduced with permission.[156] Copyright 2014, Nature Publishing Group.

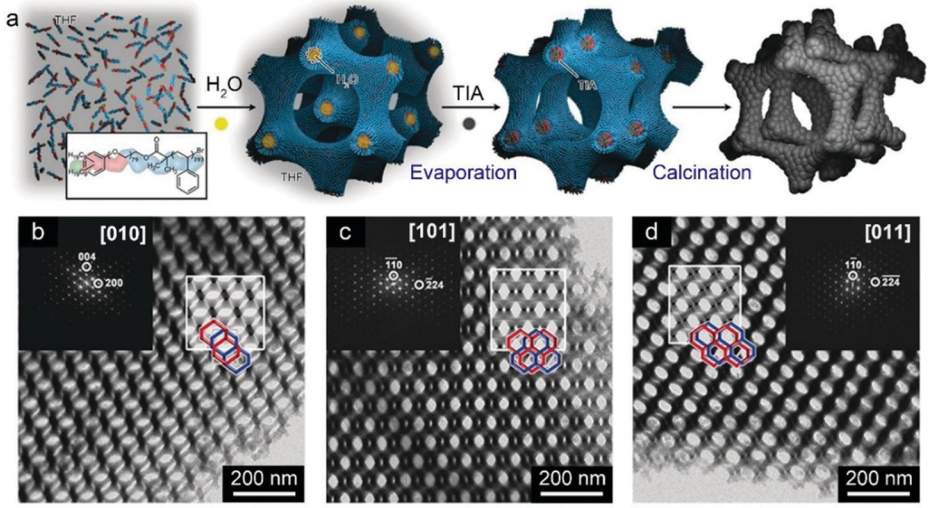

Fig. 11 Mesoporous titania with a diamond structure. (a) Illustration of the synthesis of ordered mesoporous titania with a shifted double diamond structure. (b and c) TEM images of the ordered mesoporous titania along (b) [010], (c) [101] and (d) [011] directions, respectively. (a–d) Reproduced with permission.[163] Copyright 2017, Wiley-VCH.

the copolymers during solvent evaporation. The calcination of the composite in the air produced mesoporous γ-Al_2O_3 microspheres with a shifted double diamond structure, which afforded an average pore size of 72.8 nm, a pore volume of 0.34 $cm^3\ g^{-1}$, and an SSA of 52 $m^2\ g^{-1}$.[165]

3.2.3.3 Primitive structure. The primitive (P) surface is also called the ''Plumber' nightmare'', which has a six-coordinate interconnected node for each labyrinth, as depicted in Fig. 9c.[152] The symmetry of the P surface is the same as that of the bcc structure. In 2001, Wiesner and coworkers first reported this bicontinuous structure in mesoporous materials.[169] They synthesized cubic bicontinuous aluminosilicates using PI-*b*-PEO as the template and (3-glycidyloxypropyl)trimethoxysilane and aluminum *sec*-butoxide as the inorganic precursors. The resulting mesoporous aluminosilicates had a q ratio of $\sqrt{2}{:}\sqrt{4}{:}\sqrt{6}{:}\sqrt{8}{:}\sqrt{14}$, which was consistent with that of the $Im\bar{3}m$ space group.[169] Further characterization by TEM confirmed the plumber's nightmare architecture of the resulting mesoporous aluminosilicates,[170,171] rather than a bcc structure. The P surface structure has been rarely documented thus far. In the last decade, there have been no reports on mesoporous materials with this structure, except for SiO_2.

3.2.4 Hierarchical pore structures. Hierarchical pore structures combine the benefits of macropores (which can provide improved mass transport) and mesopores or micropores (which can provide high surface area).[6,20,172,173] However, many hierarchical porous materials are typically generated by activation of alkali[174,175] or ammonia gas,[176] and the pore structure is often irregular/disordered, which is not beneficial to the precise control of functional performance of the materials. Hence, the preparation of hierarchical porous materials with well-defined pore structures has become a research hotspot in recent years.[177–180]

Wiesner and coworkers reported a facile multiscale phase separation approach for the synthesis of hierarchical porous polymer scaffolds *via* spinodal decomposition, which can induce macro- and mesophase separation.[177] They chose PS-*b*-PEO as the structure-guiding agent and a PEO oligomer (*o*-PEO) as a small additive. The BCP and *o*-PEO were dissolved in xylene at 10 wt%, followed by solvent evaporation at 130 °C (Fig. 12a). During the evaporation of the solvent, macrophase separation between the copolymer and *o*-PEO occurred, while mesopores formed due to the microphase separation of PS-*b*-PEO (Fig. 12b). The removal of *o*-PEO by washing with water and methanol/ethanol generated the macropores (Fig. 12c).[177] This innovative method blazed a trail for the preparation of hierarchical porous materials for ESC applications.

Similarly, by multiscale phase separation of BCP and a homopolymer based on spinodal decomposition, Lee's group successfully developed a spherical and hollow assembly-based particle engineering (SHAPE) strategy for the synthesis of ordered discrete particles with tailored morphologies and hierarchical pore structures (Fig. 12d).[178] They dissolved PS-*b*-PEO, homo-polystyrene (hPS), and an inorganic precursor (pre-hydrolyzed aluminosilicate or titanium ethoxide) or organic precursor (resol) in THF to yield a homogeneous solution. During the evaporation of THF, macrophase separation occurred between hPS-rich and (precursor/PS-*b*-PEO)-rich domains, leading to a sphere-like structure (Fig. 12e). The (precursor/PS-*b*-PEO)-rich domains further underwent microphase separation to form ordered mesostructures. After calcination of the as-made samples at high temperatures to remove the polymers, ordered mesoporous materials with spherical morphology were obtained. Interestingly, the addition of a small amount of homo-poly(methylmethacrylate) (hPMMA) into the precursor solution led to the formation of mesoporous hollow spheres. As the hPMMA polymer was incompatible with the hPS polymer blend, the precursor/PS-*b*-PEO domains were preferentially located at the interface of the hPS and hPMMA domains. After the removal of the polymers, hollow porous structures were obtained (Fig. 12f). This strategy was applicable to a diverse range of mesoporous particles, such as aluminosilicates, carbon, TiO_2, Nb_2O_5, and WO_3.[178]

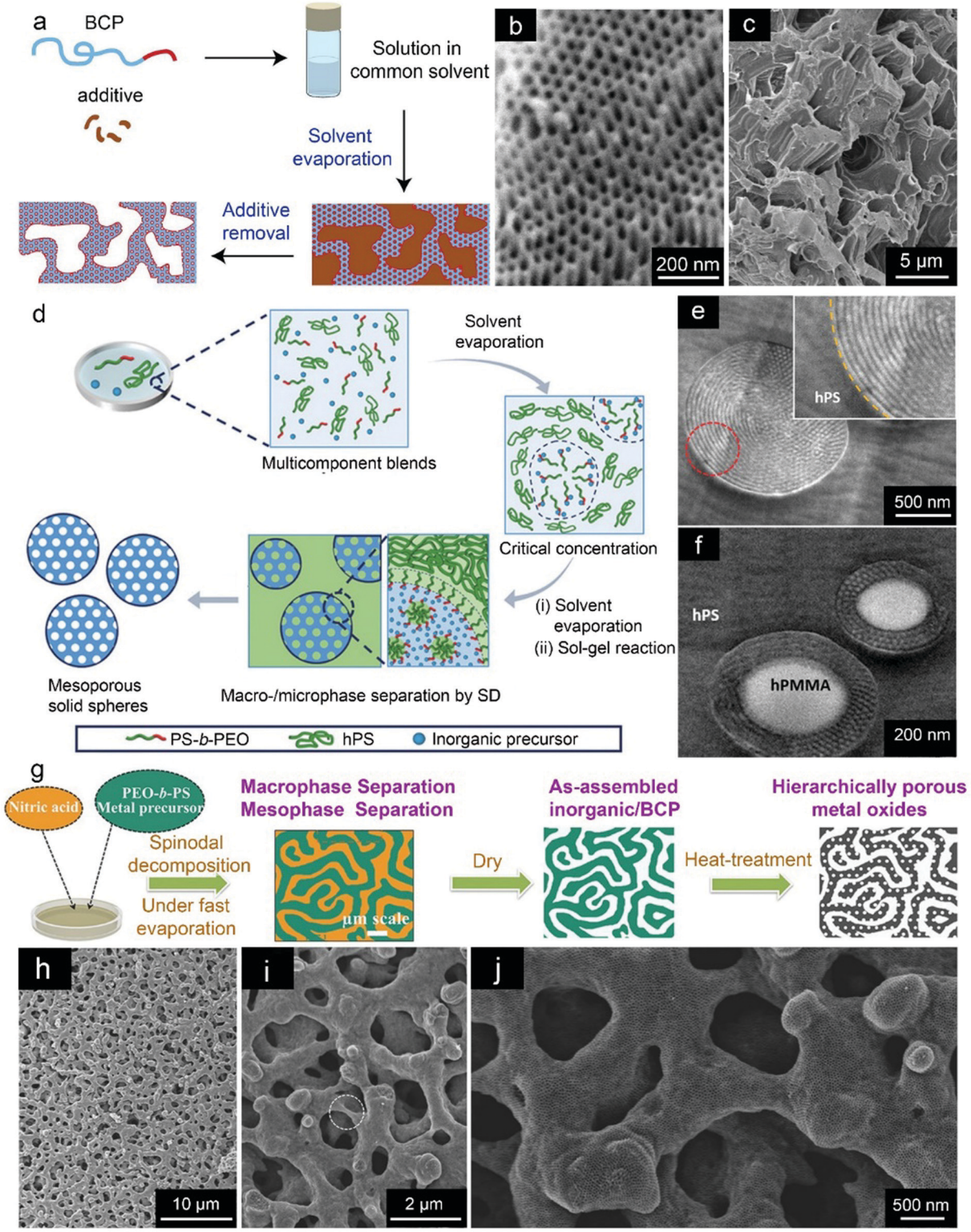

Fig. 12 Typical examples of mesoporous materials with hierarchical pore structures prepared by EISA. (a) Illustration of the synthesis of hierarchically porous polymer scaffolds with mesostructures using the spinodal-decomposition induced macro- and mesophase separation plus extraction by rinsing method (SIM^{2}PLE). (b and c) SEM images at different length scales of a bulk hierarchically porous BCP film after the removal of the PEO oligomer in methanol. (a–c) Reproduced with permission.[177] Copyright 2013, American Association for the Advancement of Science. (d) Synthesis of mesoporous solid spheres using the spherical and hollow assembly-based particle engineering (SHAPE) strategy. (e) TEM image of the as-made mesoporous aluminosilicate spheres in the hPS matrix with the inset showing the enlarged area in the red circle. (f) TEM image of the as-made mesoporous hollow aluminosilicate spheres. (d–f) Reproduced with permission.[178] Copyright 2018, Wiley-VCH. (g) Synthetic route towards the hierarchically porous TiO_2. (h–j) SEM images of hierarchically porous titanium-niobium oxides. (g–j) Reproduced with permission.[179] Copyright 2018, Wiley-VCH.

In another report, Lee's group synthesized hierarchically porous metal oxides with macro/meso/micropores *via* multi-scale phase separation by introducing volatile small molecules (Fig. 12g).[179] Nitric acid was added into a THF solution containing PS-*b*-PEO and metal oxide precursors. During the evaporation of THF, the mesophase separation took place from PS-*b*-PEO, while the addition of nitric acid and the controlled evaporation process led to the macrophase separation. The fast and preferential evaporation of THF acted as the stimulus for spinodal decomposition, which made the homogeneous solution thermodynamically unstable. Thus, the macrophase separation occurred between the immiscible phases of the nitric acid and the precursor solution. During the evaporation process, the nitride acid was removed, resulting in macropores. As a result, they obtained hierarchically porous titanium–niobium oxide (Fig. 12h–j).[179]

Hierarchically porous structures based on BCP-templated methods have also been introduced into metal–organic frameworks (MOFs) and covalent organic frameworks (COFs), which generally consist of well-defined uniform micropores or small mesopores (2–3 nm). The introduction of large mesopores to construct hierarchically porous MOFs or COFs is an effective strategy to enhance their functional performance. Many studies have reported the successful synthesis of hierarchically porous MOFs and their pore structures are diverse.[45,181–184] As a typical example, Yang and coworkers synthesized hierarchical macro-/mesoporous Cu-BDC MOFs using PS spheres as the macroporous template and P123 as the mesoporous template.[184] These templates were first dispersed in ethanol. Subsequently, the MOF precursors including $Cu(NO_3)_2{\cdot}3H_2O$ and *p*-phthalic acid were dissolved in the mixture. After the evaporation of ethanol at 30 °C for 5 days and the removal of these two templates, followed by further reaction at 60 °C for 10 hours, Cu-BDC MOFs with highly ordered macropores (fcc close-packed arrangement) and mesopores (hexagonal packing) were obtained.[184] Compared with the synthesis of hierarchically porous MOFs, hierarchically porous COFs have been rarely achieved thus far. Very recently, Ke and colleagues reported a general method combining 3D-printing technology and the BCP-templated method for the synthesis of imine COFs with hierarchical porous structures.[185] The COF precursors (imine and β-ketoenamine oligomer) and F127 were first dissolved in a mixed solvent of water and THF. After the evaporation of THF, a hydrogel was obtained as a 3D-printable source. After 3D printing, removal of the F127 template and solvent annealing, imine COFs with a nano-to-macroscale hierarchical porous feature were obtained.[185] Profiting from their high surface areas and hierarchically porous structures, these MOF and COF materials hold great promise as electro- or photocatalysts.[186,187]

3.3 Solution-based nanoprecipitation methods

In addition to BCP self-assembly in the bulk and EISA methods, solution-based nanoprecipitation strategies provide effective routes for constructing porous nanomaterials with well-defined morphologies, tunable sizes and pore structures, accompanied by less time/energy-consuming preparation processes.[44,188–190] Moreover, the solution-based routes offer advantages for large-scale production owing to unlimited batch size. By nanoprecipitation methods, porous materials with distinct morphologies can be constructed. In addition, a wide range of porous materials with different dimensions have been achieved by utilizing templates with different dimensions.

In a typical nanoprecipitation approach, BCP/precursor composite aggregates are formed by the co-assembly of BCPs and precursor molecules in suitable solvent systems or by the interactions between precursor molecules and pre-assembled BCP aggregates, such as hydrogen bonding, electrostatic force, coordination interactions, and other non-covalent interactions.[44,189] The morphology of the composite aggregates can be tailored by adjusting the composition of the BCP, the molar ratio of the BCP to precursor, the nature of the solvent system, and so on. Initiated by catalysts or other polymerization/condensation conditions, the precursors crosslink or polymerize into continuous networks in the coronal domain of the BCP aggregate templates. The removal of the sacrificial BCP templates by solvent dissolution or thermal treatment produces mesoporous materials. By selecting different precursors to interact with BCP templates in solutions, various types of mesoporous materials have been constructed, including carbons, metals, metallic compounds, and carbon/metal composites.[44,189] Without any other template to control the dimension, 2D and 3D mesoporous materials are the typical products of nanoprecipitation methods.

3.3.1 2D mesoporous materials. Since the discovery of mechanically exfoliated graphene in 2004, research interest on 2D materials has increased exponentially.[191–193] Owing to their unprecedented physical and chemical properties, 2D materials have been considered as an emerging class of nanostructures with large surface area, and unique electronic and optical properties.[194,195] The introduction of mesopores in 2D materials provides opportunities to tune their functional properties because the pores may enhance the mass transport and the increased surface area may improve the effective utilization of the materials, thus providing an increased amount of active sites for reactants.[196,197]

3.3.1.1 Freestanding nanosheets. 2D freestanding nanosheets are challenging to achieve without the assistance of 2D templates. To date, there have been only a few reports on the successful synthesis of freestanding nanosheets through the solution-based nanoprecipitation method. Recently, Yamauchi and co-workers fabricated 2D mesoporous Ir nanosheets with hexagonally arranged mesopores *via* the self-assembly of PS-*b*-PEO into spherical micelles in a mixture solution of DMF and H_2O (Fig. 13a),[198] using $IrCl_3$ as the Ir source and formic acid as both reducing and shape control agents. In this report, the Ir precursor was reduced into small Ir nanocrystals by formic acid at 80 °C. These Ir nanocrystals were subsequently stabilized by the PEO chains of PS-*b*-PEO spherical micelles. Then, the decomposition of formic acid into carbon monoxide occurred, catalyzed by the presence of Ir metal. The released CO was adsorbed on the surfaces of the Ir nanocrystals and drove the anisotropic growth of the Ir/micelle superstructure into sheet-like morphology. After the removal of the template by solvent extraction and calcination in N_2, 2D fcc mesoporous Ir nanosheets

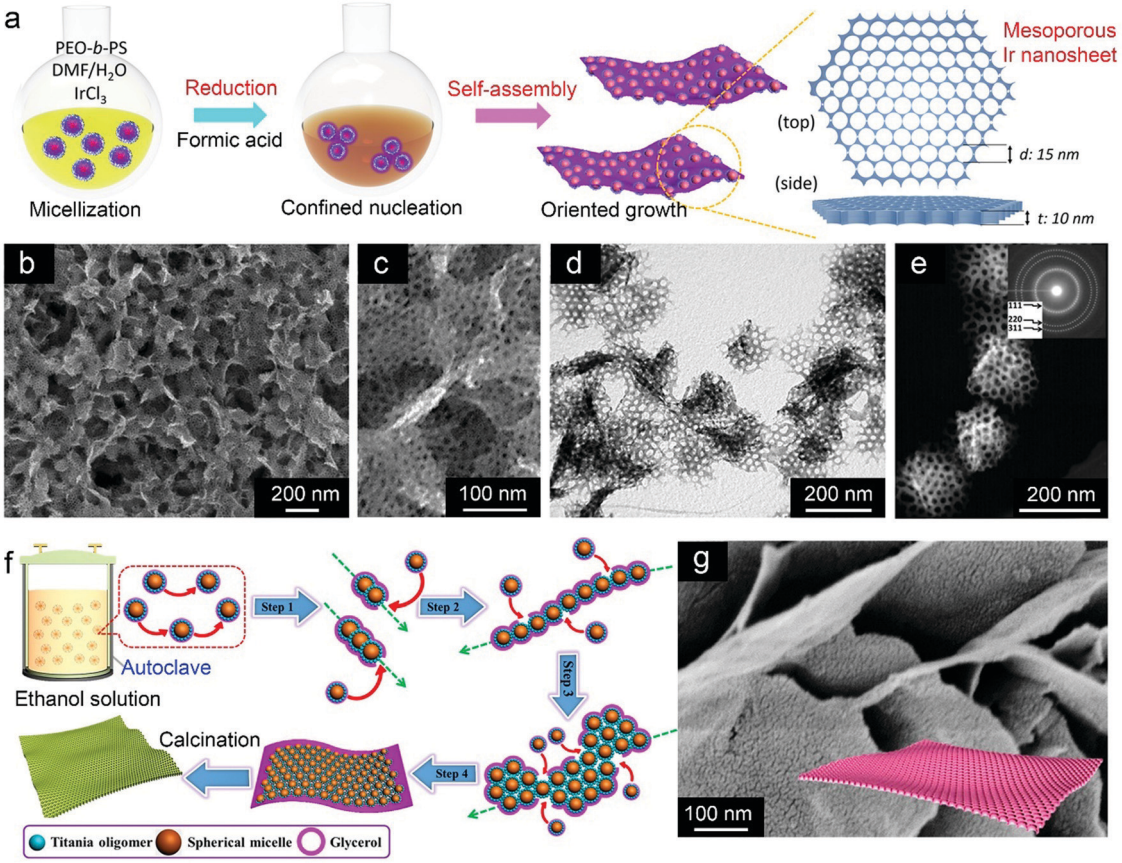

Fig. 13 BCP micelle-templating synthesis of freestanding 2D nanosheets in solution. (a) Schematic representation of the formation of the mesoporous Ir nanosheets. (b) Low- and (c) high-magnification SEM images showing the macroporous and mesoporous structures of Ir nanosheets. (d) TEM image and (e) HAADF-STEM image of the mesoporous Ir nanosheets. (a–e) Reproduced with permission.[198] Copyright 2018, American Chemical Society. (f) Schematic illustration of the formation process for the single-layered 2D ordered mesoporous TiO_2 nanosheets *via* hydrothermal-induced solvent-confined monomicelle assembly. (g) TEM image of the single-layered mesoporous TiO_2. (f and g) Reproduced with permission.[199] Copyright 2018, American Chemical Society.

(Fig. 13b–e) with an average pore size of 15 nm and SSA of 42 $m^2 g^{-1}$ were obtained.[198]

Controlling the morphology of mesoporous metal oxide materials provides further opportunities to tune their functional properties. However, the shape control of mesoporous oxides remains challenging as it typically requires a high-pressure environment. Lan *et al.* previously demonstrated the synthesis of freestanding mesoporous TiO_2 nanosheets through hydrothermal-induced solvent-confined self-assembly of spherical F127/TiO_2 hybrid monomicelles (Fig. 13f and g).[199] The formation of such mesoporous nanosheets originated from the self-assembly of the initially formed F127/TiO_2 composite spherical monomicelles dispersed in an ethanol/glycerol mixture into a single-layered 2D mesostructure under hydrothermal conditions (at 100 °C). The thickness of the resulting mesoporous TiO_2 nanosheets could be controlled from 5.5 to 25.5 nm by modifying the ethanol/glycerol ratio from 1 : 1 to 5 : 1, leading to significant reduction in SSA from 210 to 154 $m^2 g^{-1}$. Similarly, the increase of the precursor concentration (*i.e.*, the amount of monomicelle gel) also led to an increase in the thickness of the resulting TiO_2 nanosheets from 11.1 to 27.6 nm. Furthermore, the diameter of the mesopores could be tuned from 7.4 to 12.5 nm by the addition of trimethylbenzene as a swelling agent.[199]

3.3.1.2 Thin films. Different from freestanding nanosheets, the preparation of mesoporous thin films usually requires external assistance. For instance, Yamauchi's group reported the fabrication of many porous thin-films of metals and metal alloys by electrochemical deposition methods using BCP micelles as soft templates.[21,200] For example, continuous mesoporous Au films with large-sized pores of 19–25 nm (Fig. 14a) have been obtained through the electrochemical deposition of precursor solutions containing PS-*b*-PEO and tetrachloroauric(III) acid ($HAuCl_4$).[201] PS-*b*-PEO was first dissolved in a THF/ethanol mixture, which formed spherical micelles composed of PS cores and PEO coronas upon the addition of $HAuCl_4$ aqueous solution (Fig. 14b and c). The hydrophilic PEO blocks in the coronas of the micelles interacted with aqua-$HAuCl_4$ complexes. By applying potentials, the composite micelles associated with the Au species were deposited on the working electrode. The removal of the template was performed using ultraviolet (UV) ozone cleaning. The resulting mesoporous Au film possessed uniform mesopores with an

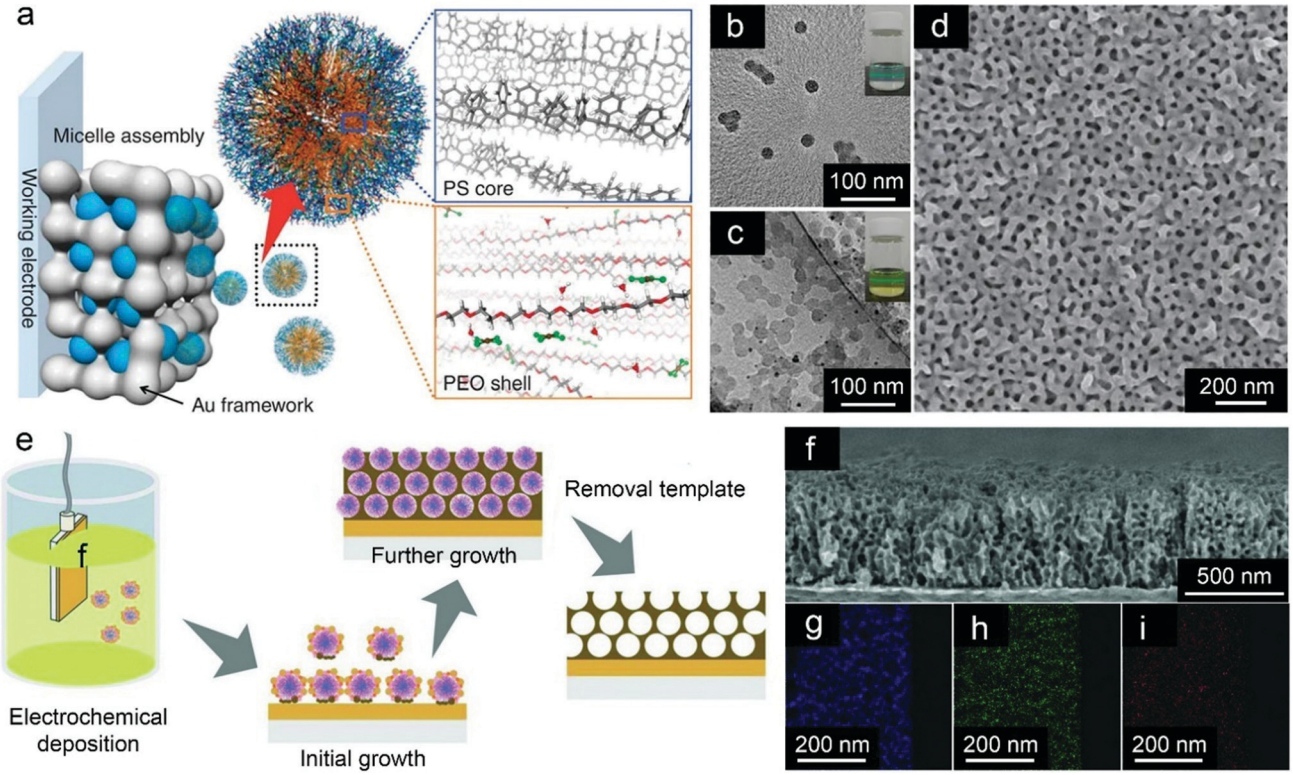

Fig. 14 BCP micelle-templating fabrication of mesoporous thin films by electrochemical synthesis. (a) Schematic illustration of the formation of mesoporous Au films. (b and c) TEM images of PS-*b*-PEO micelles formed in aqueous solution (b) without and (c) with a $HAuCl_4$ source. (d) Top-surface SEM images of a mesoporous Au film. (a–d) Reproduced with permission.[201] Copyright 2014, Nature Publishing Group. (e) Schematic illustration of the electrochemical synthesis of mesoporous AuCuNi ternary alloy films. (f) SEM image of the mesoporous AuCuNi film at an applied deposition potential of −0.9 V (*vs.* Ag/AgCl) at 40 °C, 1000 s. (g–i) Elemental mappings: (g) Au, (h) Cu, and (i) Ni. (e–i) Reproduced with permission.[212] Copyright 2018, Wiley-VCH.

average size of 25 nm (Fig. 14d). The convenience of this method lies in the ease of tuning of the pore size by changing the amount of THF. Specifically, by varying the amount of THF, the pore diameter of the film was reduced from 25 to 19 nm. Furthermore, the thickness of the resulting mesoporous Au film was controlled from 70 to 440 nm by adjusting the deposition time.[201] Based on this method, various mesoporous metallic films, including mesoporous Cu,[202] Pd,[203] Ni,[204] Pt,[205] Rh,[206] and Au,[207] have been obtained.

Similarly, bimetallic[208–211] and ternary trimetallic alloys[212] have been prepared using Pluronic or non-Pluronic BCPs as soft templates. Multimetallic alloys are known to exhibit superior catalytic activity and stability over monometallic metals due to the incorporation of additional metallic components. For instance, trimetallic mesoporous AuCuNi alloy films have been fabricated by the co-electrodeposition of $HAuCl_4$, $CuSO_4$, and $NiCl_2$ precursors in the presence of PS-*b*-PEO as a soft template (Fig. 14e).[212] In this work, the PS-*b*-PEO template was first dissolved in THF to produce a unimer solution. Following the addition of aqueous solutions containing Au, Cu and Ni precursors, the polymeric template self-assembled into spherical micelles in the solution. Following the application of an appropriate potential, the formed spherical micelles were deposited on the Au-coated silicon substrate. The selection of an appropriate applied potential was highly critical for achieving the co-deposition of the three metals because of the large difference between the standard reduction potentials of the different metal precursors (*i.e.*, the standard reduction potentials of $[AuCl_4]^-$/Au, Cu^{2+}/Cu, and Ni^{2+}/Ni are +1.00, +0.34, and −0.25 V *versus* standard calomel electrode (SCE), respectively). The final composition of the resulting mesoporous trimetallic AuCuNi films was easily controlled by modifying the initial concentrations of the Au, Cu, and Ni precursors in the original electrodeposition solution (Fig. 14f–i).[212]

3.3.2 3D mesoporous materials

3.3.2.1 Mesoporous particles with defined morphologies. Nanoprecipitation methods provide a versatile route for the controllable synthesis of discrete mesoporous particles with the assistance of BCP assemblies as the pore-directing templates. In this subsection, mesoporous particles with defined morphologies are discussed following an order of pore structures templated by spherical micelles, cylindrical micelles, vesicles, and bicontinuous assemblies, which successively appear with the increase of the packing parameter in the morphological phase diagram of BCP self-assembly in solution (Fig. 2).

Spherical micelles are the most common aggregates formed by the self-assembly of BCPs in solutions, which have been frequently used as single-micelle or compound-micelle templates for the construction of mesoporous nanospheres.[21,44,189,213–215] Using single micelles as the templates, Ariga and co-workers

prepared hollow carbon nanospheres loaded with Ir NPs through the co-assembly of asymmetrical triblock PS-*b*-P2VP-*b*-PEO copolymer micelles, Ir precursors (Na_3IrCl_6), phenolic resol resin in solutions containing THF and HCl, where negatively charged Ir ions interacted with a positively charged micelle template *via* electrostatic interactions and then coated with a layer of phenolic resol (Fig. 15a).[216] Each block of the terpolymer provided a distinct function: (1) the hydrophobic PS core was used to create hollow voids because the carbon source was accommodated around the PS core; (2) the protonated P2VP blocks served as binding sites for the metal ions and phenolic resol; (3) the hydrophilic PEO corona stabilized the composite micelles in solution. Heating the composite micelles under hydrothermal conditions induced the cross-linking of the phenolic resol on the PS-*b*-P2VP-*b*-PEO micelles. Then, the resin-coated micelles were decomposed to hollow carbon nanospheres loaded with Ir NPs following the thermal treatment under inert atmosphere due to the complete decomposition of the triblock copolymer template. The as-formed hollow carbon NPs had an average particle size of 42 nm, hollow cores of 23 nm, and SSA of 2490 $m^2\ g^{-1}$ with well-dispersed Ir NPs throughout the hollow carbon NPs (Fig. 15b).[216] Following similar strategies, a library of BCPs, such as PS-*b*-PAA, PMMA-*b*-PEO, PS-*b*-PMMA-*b*-PEO, and PS-*b*-poly[(3-(methacryloylamino)propyltrimethylammonium

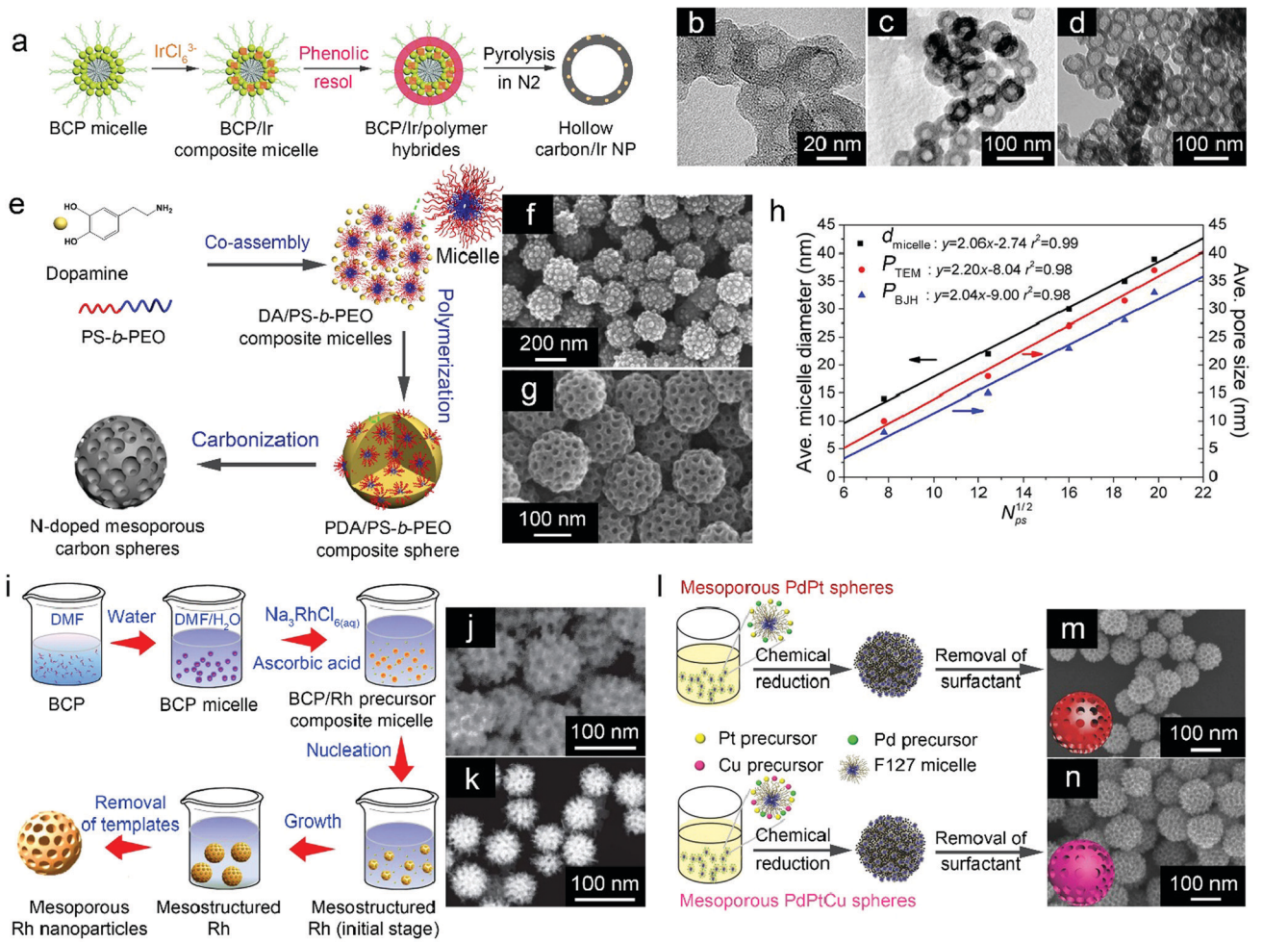

Fig. 15 Synthesis of discrete mesoporous nanospheres with the assistance of single or compound spherical micelles as the templates in solution. (a) Synthesis of hollow carbon nanospheres loaded with uniformly dispersed metal NPs by using BCP micelle templates. (b) Hollow carbon nanospheres loaded with Ir NPs. (a and b) Reproduced with permission.[216] Copyright 2017, Wiley-VCH. (c) Hollow carbon nanospheres. Reproduced with permission.[217] Copyright 2017, Royal Society of Chemistry. (d) Hollow NiO nanospheres. Reproduced with permission.[218] Copyright 2014, Royal Society of Chemistry. (e) Formation process of N-doped mesoporous carbon nanospheres. (f and g) SEM images of (f) polydopamine/PS-*b*-PEO composite spheres and (g) N-doped mesoporous carbon spheres. (e–g) Reproduced with permission.[220] Copyright 2015, Wiley-VCH. (h) A linear relationship between the average pore size of the mesoporous carbons and the square root of the number of repeating units in the PS block of PS-*b*-PEO ($d_{micelle}$ denotes the average diameter of the BCP micelles; P_{TEM} and P_{BJH} represent the average pore diameters of the mesoporous carbon spheres measured from TEM images and pore size distribution curve, respectively). Reproduced with permission.[9] Copyright 2016, Wiley-VCH. (i) An illustration describing the formation mechanism for a mesoporous Rh nanostructure. (j) High-magnification SEM micrograph and (k) HAADF-STEM micrograph of mesoporous Rh NPs. (i–k) Reproduced with permission.[221] Copyright 2017, Nature Publishing Group. (l) Schematic illustration of mesoporous bimetallic PdPt spheres and trimetallic PdPtCu spheres. (m and n) SEM images of (l) mesoporous PdPt spheres and (n) mesoporous PdPtCu spheres. (l–n) Reproduced with permission.[222] Copyright 2015, Wiley-VCH.

chloride)]-*b*-PEO (PS-*b*-PMAPTAC-*b*-PEO), have been used as soft templates for the construction of a broad range of hollow NPs,[189] such as carbon (Fig. 15c)[217] and metallic compounds (Fig. 15d).[218]

Aside from single spherical micelles, spherical compound micelles are frequently employed as soft templates to prepare mesoporous nanospheres.[9,219,220] Zhao and co-workers developed a low-concentration hydrothermal route towards ordered mesoporous carbon NPs.[219] In this work, spherical phenolic resol-F127 monomicelles were first formed through hydrogen bonding between Pluronic F127 and resol under a low concentration (10^{-7} mol L^{-1}), which prevented the excessive cross-linking of the micelles. During the hydrothermal process at 130 °C, the F127/resol spherical monomicelles self-assembled into a cubic-close packed mesostructure (space group $Im\bar{3}m$), in which phenolic resol was cross-linked, resulting in a spherical morphology. Simultaneously, when the polymerization of resol took place within the spheres, the high-temperature hydrothermal treatment drove the small spherical micelles to accumulate and rearrange, leading to the formation of a large spherical F127/resol composite with an ordered cubic mesostructure. After carbonization, the F127 template was removed and mesopores with an average pore size of 3 nm were generated. The diameter of the ordered mesostructure was controllable in the range of 20–140 nm by simply adjusting the reagent concentration. These mesoporous carbon nanospheres exhibited SSAs in the range of 894–1131 m^2 g^{-1} and pore volumes of 1.0–1.5 cm^3 g^{-1}.[219] Based on a similar self-assembly protocol, Yamauchi *et al.* prepared nitrogen-doped mesoporous carbon nanospheres using PS-*b*-PEO copolymers with different molar masses as soft templates and dopamine as the nitrogen-containing carbon source (Fig. 15e–g).[220] The mesopores were generated from the occupation of the PS block, and the wall thickness of the mesopores was determined by the length of the PEO block. Meanwhile, Mai and coworkers also synthesized N-doped mesoporous carbon nanospheres using a series of PS-*b*-PEO copolymers with different PS block lengths as soft templates.[9] This systematic study revealed a linear relationship between the average pore size of mesoporous carbon particles and the square root of the number of repeating units in the PS block, providing an equation for quantitatively controlling over the pore dimension of mesoporous carbon materials (Fig. 15h).[9]

Spherical compound micelles are also applicable for the construction of mesoporous noble metals that have emerged as cutting-edge nanostructured catalysts.[223,224] To date, a variety of mesoporous metals have been synthesized with the assistance of BCPs, including monometallic, bimetallic and trimetallic mesoporous metals.[21] In the past decade, significant progress has been made in the BCP-templated fabrication of mesoporous monometallic particles, such as mesoporous platinum (Pt),[225,226] rhodium (Rh),[221] and palladium (Pd).[227] For example, the shape- and size-controllable synthesis of mesoporous Pt nanospheres has been achieved through the slow reduction of H_2PtCl_6 with ascorbic acid in the presence of Pluronic F127 as a soft template.[226] The resulting Pt nanospheres exhibited interconnected mesopores with an average pore size and wall thickness of 11 and 10 nm, respectively. Mesoporous Pt nanospheres with large average pore sizes of 8, 14, and 35 nm were previously obtained by using high-molecular-weight PS-*b*-P2VP-*b*-PEO triblock copolymers with different PS block lengths as the templates. In this triblock copolymer, the P2VP block served as an efficient metal-binding block, even more effective than PEO. The PEO block helped to stabilize the micelle *via* steric repulsion and the hydrophobic PS block formed the core of the micelle and controlled the size of the mesopores. The PS-*b*-P2VP-*b*-PEO copolymer was dissolved in a DMF and water mixture, generating core–shell-corona type spherical micelles. The protonated P2VP shells served as binding sites for $PtCl_4^{2-}$ ions. The addition of an ascorbic acid solution initiated both the Pt deposition and the micelle assembly. The surface of the Pt nanospheres became decorated with spherical micelles which were converted into mesopores upon a simple calcination at 250 °C in air.[226] Compared to noble metals, such as Pd and Pt, the preparation of mesoporous Rh particles by chemical reduction is more challenging due to its much higher surface energy. Therefore, the successful synthesis of mesoporous Rh requires a careful control of the reaction kinetics. Yamauchi and co-workers successfully synthesized mesoporous Rh particles with an average pore size of 11 nm by employing PMMA-*b*-PEO, Na_3RhCl_6, and ascorbic acid as soft template, Rh precursor and reducing agent, respectively (Fig. 15i).[221] In a mixed solution of DMF/H_2O, PMMA-*b*-PEO formed spherical micelles which interacted with the Rh species, $[Rh(H_2O)_{3-x}Cl_{6-x}]^{(3-x)-}$, through hydrogen bonding and ion–dipole interactions on the PEO coronae of the micelles. These interactions led to an increase in the concentration of Rh complexes around the micelles and drove the reaction further. With the addition of an ascorbic acid solution, the reduction of Rh species in close proximity of the micelles combined with the PEO–Rh metal interactions promoted the formation of the mesostructured Rh particles. The obtained Rh NPs (Fig. 15j and k) possessed uniform and closely packed spherical porous structures with an average pore size of 10 nm, a pore wall thickness of 11 nm, and an SSA of 50 m^2 g^{-1}.[221] Multicomponent metallic alloys have also attracted significant research interest. Various mesoporous bimetallic alloys, including RhCu,[228] PtCu,[229] PtPd,[230] and PtCo,[231] have been achieved. Taking PdPt spheres as an example,[222] mesoporous bimetallic PdPt spheres were previously synthesized in an aqueous solution containing both Pd and Pt precursors, with F127 as the pore-directing agent (Fig. 15l, top side). In addition, F127 also acted as a protective agent for preventing the aggregation of the formed bimetallic spheres. The metal precursors could be incorporated into the PEO regions of the F127 micelles by coordination interactions. Following the reduction of the metal precursors, metal nuclei were generated and grew further by interacting with the dissolved metal species, and mesoporous nanospheres were subsequently constructed through the close packing of the micelle/metal nanohybrids. By controlling the reduction rate, monodispersed mesoporous PdPt nanospheres were finally formed (Fig. 15m), with a uniform pore size of 18.5 ± 0.5 nm, a wall thickness of 8.0 ± 0.5 nm, and an SSA of 29.9 m^2 g^{-1}. Similarly, the nanoprecipitation method has also been utilized for synthesizing mesoporous trimetallic alloy nanospheres, such as PdPtCu (Fig. 15l, bottom, and Fig. 15n).[222]

By employing solution-based nanoprecipitation methods and spherical compound BCP templates, mesoporous metallic compounds, including metal oxides,[232] metal carbides,[233] and heteropolyacids,[234] have also been constructed. Moreover, by combining the precursors of carbon and metallic compounds, metallic compound NPs decorated on supporting mesoporous carbon frameworks can be constructed, which have the advantages of each component, while avoiding the aggregation of metal species.[235–237] In one example, ordered mesoporous iron–nitrogen doped carbon with an open porous structure was constructed using F127 as the pore-directing agent and phenol/formaldehyde (P-MF) and melamine as carbon and nitrogen sources, respectively.[236] Soluble P-MF was first mixed with F127 in water to form P-MF/F127 composite micelles through hydrogen bonding. Then, a stoichiometric amount of $FeCl_3$ was introduced into this system and Fe^{3+} doped P-MF/F127 complex micelles as Fe–N/C precursors were formed. The subsequent hydrothermal treatment induced further rearrangement and polymerization of the complex micelles and the resulting Fe–N/C precursors were subsequently pyrolyzed at 700–900 °C. The obtained porous particles showed a rhombic dodecahedral shape with an $Im\bar{3}m$ bcc symmetry, alongside SSAs of 741.6–1166.3 $m^2\ g^{-1}$ and pore volumes of 0.75–1.37 $cm^3\ g^{-1}$. All samples showed a bimodal pore size distribution: around 2.5–3.5 nm and 4.0–5.5 nm, where the larger mesopores originated from the P-MF/F127 micelle template, and the smaller ones were attributed to the intra-wall pores.[236] Yamauchi's group reported the assembly of Mo_2C nanocrystals onto the surfaces of mesoporous hollow carbon particles.[233] In this work, the soft template was PS-*b*-PEO, $(NH_4)_6Mo_7O_{24}{\cdot}4H_2O$ was used as the Mo source, and dopamine hydrochloride (DA) acted as both coordination ligand and N-containing carbon precursor. The addition of ammonia initiated the polymerization of DA to polydopamine (PDA) that interacted with both MoO_4^{2-} and PS-*b*-PEO micelles to form MoO_4^{2-}/PDA/PS-*b*-PEO composite nanosheets (Mo–PDA–PS), which further assembled into 3D spherical architectures. The carbonization of PDA, during which the micelle template was also removed, drove a reaction between the Mo-containing components and carbonaceous species, yielding ultrafine molybdenum carbide (Mo_2C) NPs. Eventually, hollow NPs composed of Mo_2C/N-doped carbon porous nanosheets with embedded Mo_2C NPs (~2 nm in diameter) were formed, with a uniform pore size of 10 nm and an SSA of 212 $m^2\ g^{-1}$.[233]

Employing cylindrical micelles as the template, Zhao and coworkers first reported mesoporous carbon particles with cylindrical pores in 2007. They obtained cubic mesoporous carbon single-crystals of rhombdodecahedron with a uniform pore size of 5 μm by aqueous organic–organic self-assembly of F127 and phenol/formaldehyde resols.[238] Inspired by this work, several mesoporous materials with highly ordered hexagonal mesostructures have been achieved.[239,240] Deng and coworkers prepared mesoporous carbon particles in aqueous solution *via* hydrothermal treatment (Fig. 16a).[239] In their work, F127 was used as the pore-directing agent and phenol/formaldehyde (PF) resols were used as the carbon precursor. Hexamethylenetetramine (HMT) was employed to replace formaldehyde during the polymerization of PF resols because it was stable in aqueous solution and could slowly release formaldehyde and ammonia. The organic–organic self-assembly could be well controlled upon the introduction of HMT, which played a crucial role in the construction of RF-based mesoporous carbons with an ordered hexagonal mesophase (Fig. 16b and c). The resultant mesoporous carbon particles exhibit a spherical morphology with a pore diameter of 4.7 nm, a high SSA of 1483 $m^2\ g^{-1}$ and a total pore volume of 0.96 $cm^3\ g^{-1}$.[239] Through similar aqueous

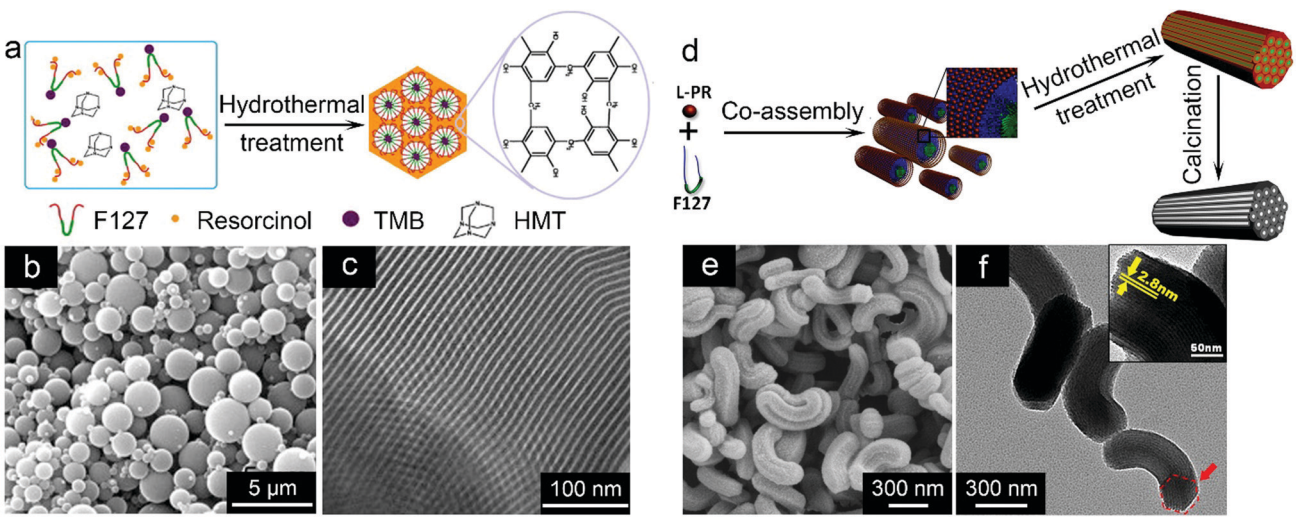

Fig. 16 Synthesis of mesoporous carbon particles with an ordered hexagonal mesophase with the assistance of BCP templates in aqueous solutions. (a) Schematic illustration of the formation of ordered mesostructured RF/F127 composites. (b) SEM and (c) TEM images of the mesoporous carbons with an ordered hexagonal mesostructure. (a–c) Reproduced with permission.[239] Copyright 2011, Elsevier. (d) Schematic illustration of the preparation of rod-like carbon particles with ordered hexagonal mesostructure. (e) SEM and (TEM) images of the rod-like carbon particles with a hexagonal mesophase. (d–f) Reproduced with permission.[240] Copyright 2012, Elsevier.

self-assembly with F127 as the pore-directing template and the assistance of hydrothermal treatment, Xue and coworkers synthesized interesting rod-like carbon particles with an ordered hexagonal mesostructure by precisely tuning the added amount of F127 (Fig. 16d–f).[240]

By using BCP vesicles as templates, Mai and co-workers prepared bowl-like N-doped carbon hollow particles templated by PS-*b*-PEO "kippah" vesicles in solution (Fig. 17a).[241] In this case, dopamine was employed as the carbon precursor, which was adsorbed in the PEO coronae of the vesicles *via* hydrogen bonding. After the polymerization of dopamine and pyrolysis of the resulting vesicle-polydopamine particles at 900 °C under nitrogen atmosphere, bowl-shaped N-doped carbon hollow NPs were obtained. The bowl-like carbon NPs (Fig. 17b and c) possessed an average diameter of 450 nm, uniform carbon shell thickness of 23 nm, and high SSA of 370 m^2 g^{-1}.[241] Compared to their spherical counterpart, the bowl-shaped hollow particles exhibited increased packing density,[242] thus reducing the volume of the resulting electrodes.

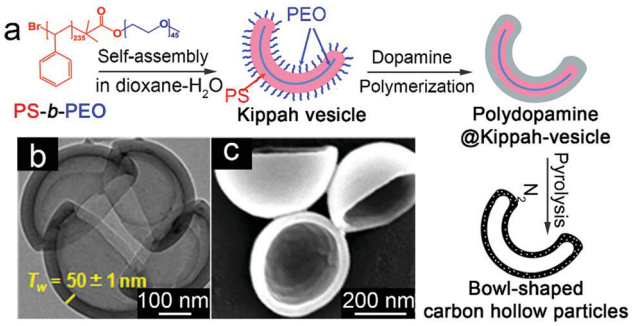

Fig. 17 BCP vesicle-templating synthesis of bowl-shaped mesoporous carbon particles in solution. (a) Schematic illustration of the preparation of bowl-shaped nitrogen-doped carbon using "kippah" vesicles as the template. (b) TEM and (c) SEM images of the bowl-shaped nitrogen-doped carbon hollow particles. Reproduced with permission.[241] Copyright 2016, Royal Society of Chemistry.

The fabrication of 3D porous particles with bicontinuous structures through BCP self-assembly in solution has so far been rarely reported due to the difficulty in finding appropriate self-assembly conditions for the formation of bicontinuous structures of BCPs.[38,243–251] These complex mesophases have been primarily documented in BCP colloidal particles thus far. Mai and coworkers demonstrated the tunable self-assembly of PS-*b*-PEO copolymers into mesoporous polymer cubosomes with inverse $Im\bar{3}m$ or $Pn\bar{3}m$ mesophases (Fig. 18a–e).[38] They plotted a new morphological phase diagram for the solution self-assembly of PS-*b*-PEO through the initial copolymer concentration against the volume fraction of the PS block. This study affords a simple system and method for the controllable

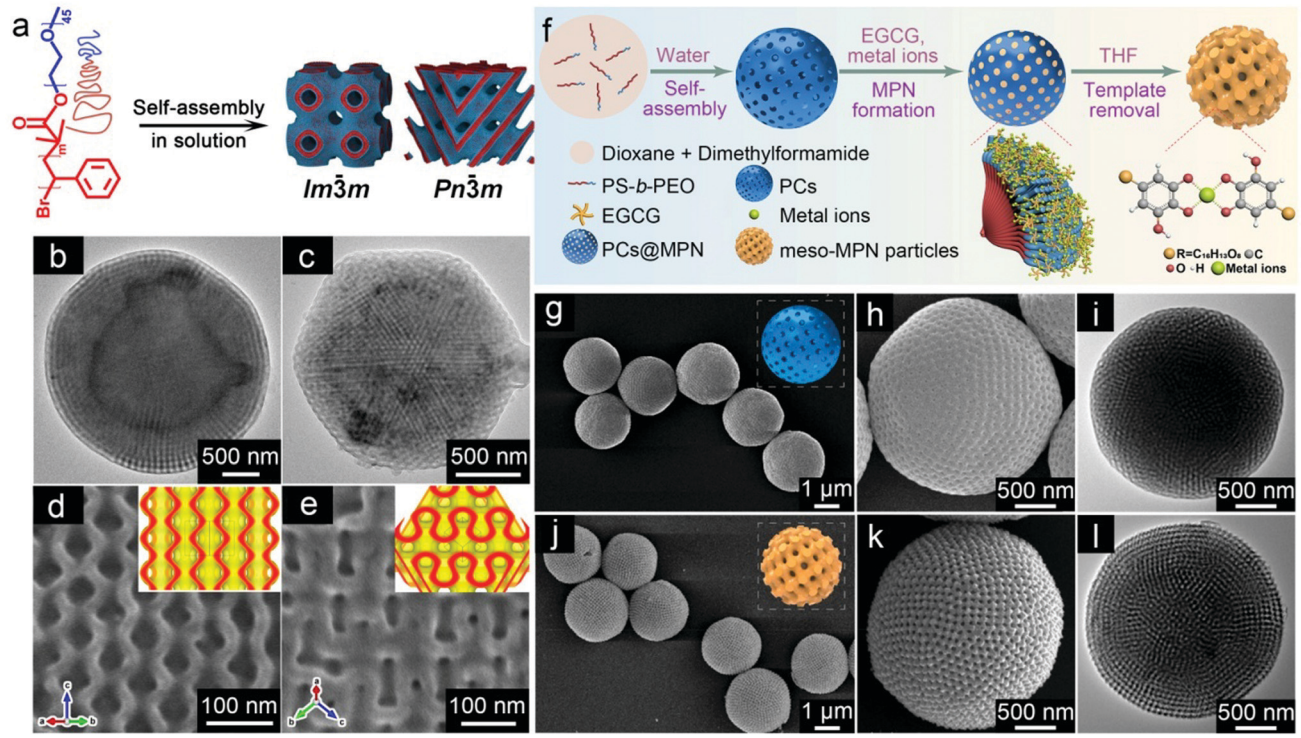

Fig. 18 Polymer cubosomes with DP and DD bicontinuous structures and functional materials prepared with the polymer cubosomes as the templates. (a) Controlled self-assembly of PS-*b*-PEO into ordered polymer cubosomes with bicontinuous structures. (b and c) TEM and (d and e) SEM images of (b and d) $Im\bar{3}m$ cubosomes formed by PS_{209}-*b*-PEO_{45} and (c and e) $Pn\bar{3}m$ cubosomes formed by PS_{236}-*b*-PEO_{45}. (a–e) Reproduced with permission.[38] Copyright 2017, Wiley-VCH. (f) Preparation of meso-MPN particles using polymer cubosomes as the templates. (g and h) SEM and (i) TEM images of PS-*b*-PEO cubosomes with an $Im\bar{3}m$ bicontinuous mesostructure. (j and k) SEM and (l) TEM images of meso-MPN particles with a $Pm\bar{3}m$ bicontinuous structure. (f–l) Reproduced with permission.[252] Copyright 2019, American Chemical Society.

preparation and fundamental studies of ordered bicontinuous structures, and provides desirable templates for the synthesis of electrochemically active porous energy materials with bicontinuous architectures. Although rarely reported, several functional materials including TiO_2 and metal–phenolic hybrids with ordered bicontinuous structures have been achieved by using bicontinuous-structured polymer cubosomes as soft templates.[252,253] Very recently, Lin *et al.* reported the fabrication of bicontinuous metal–phenolic networks (MPNs) with a single primitive cubic ($Pm\bar{3}m$) mesophase using polymer cubosomes ($Im\bar{3}m$) as sacrificial templates (Fig. 18f–l).[252] They also employed PS-*b*-PEO as the self-assembly precursor for the construction of $Im\bar{3}m$ polymer cubosomes with a bicontinuous structure (Fig. 18g–i). The subsequent filling of metal and phenolic precursors into the large mesopores of the cubosomes, followed by their cross-linking and then removal of the BCP template, produced meso-MPN particles with a single primitive bicontinuous network (Fig. 18j–l). Through this general approach, various metal and phenolic precursors were utilized to construct a wide range of bicontinuous meso-MPNs, which hold great promise in ESC applications.[252]

3.3.2.2 Porous monoliths. Porous monoliths, which are usually demanded in bulk mass electrodes of energy storage devices, can offer high storage capacity and long-term durability. Hyper-crosslinking of BCP assemblies is an effective approach to construct porous monoliths.[254–257] Matyjaszewski and co-workers previously constructed mesoporous polymeric and carbonaceous monoliths through the hyper-crosslinking of BCP micelles (Fig. 19a).[258] In their study, PMMA-*b*-PS copolymers first self-assembled into spherical micelles consisting of a PMMA core and a PS corona in a mixed solvent of carbon tetrachloride and cyclohexane. The resulting micelles were used as building blocks for the formation of polymeric frameworks by the hyper-crosslinking of the PS blocks *via* the Friedel–Crafts reaction. The intramicellar hyper-crosslinking of the PS chains in the coronae produced micropores while the intermicellar hyper-cross-linking resulted in a 3D interconnected polymeric framework containing numerous mesopores. The resulting cross-linked polymer agglomerates were converted to mesoporous carbons by pyrolysis, during which the PMMA cores decomposed leaving behind hollow holes, while the crosslinked PS domains were converted to carbon. The obtained mesoporous carbon (Fig. 19b and c) possessed a mean pore diameter of 16 nm, an average shell thickness of 6 nm, a high SSA of 829 $m^2\ g^{-1}$, and a total pore volume of 1.07 $cm^3\ g^{-1}$.[258]

Mesoporous monoliths with ordered pore structures can also be prepared by BCP-templated methods in solutions.[259,260] In a typical study by Wu and coworkers, polyethylene glycol (PEG) homopolymer was added to induce the self-assembly of phenol/formaldehyde (PF) resol and Pluronic P123 (Fig. 19d).[259] PEG has good compatibility with both of the self-assembly precursors in aqueous solution, and thus could enhance the interaction between the PF resol and P123, leading to the formation of a

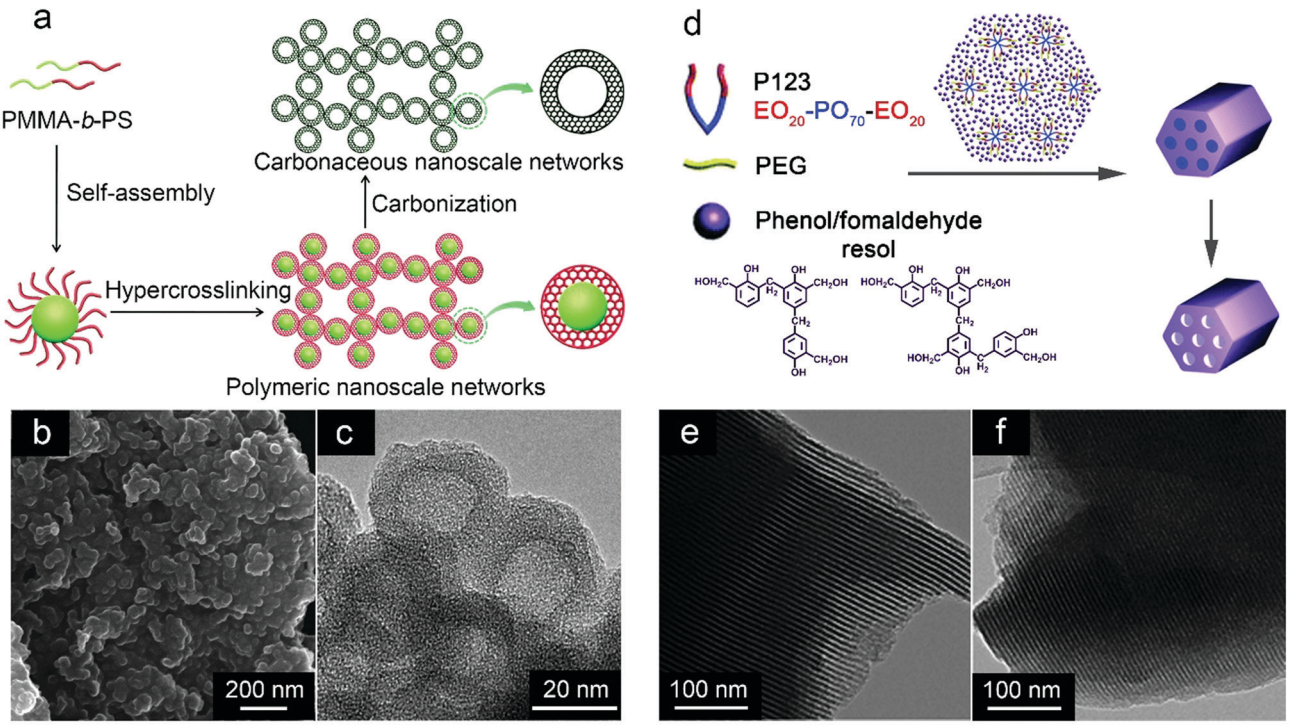

Fig. 19 BCP micelle-templating fabrication of mesoporous monoliths in solution. (a) Schematic illustration of preparation of polymeric nanoscale networks and carbonaceous nanoscale networks through the hyper-crosslinking of BCP micelles. (b) SEM and (c) TEM images of carbonaceous nanoscale networks from $PMMA_{191}$-*b*-PS_{312}. (a–c) Reproduced with permission.[258] Copyright 2014, Royal Society of Chemistry. (d) Schematic diagram of preparation of ordered mesoporous polymers with 2D hexagonal structures through the PEG-induced self-assembly procedure. (e and f) TEM images of (e) ordered mesoporous polymers and (f) ordered mesoporous carbons. (d–f) Reproduced with permission.[259] Copyright 2013, Royal Society of Chemistry.

2D hexagonal ordered mesostructure. Through a simple mixing of P123, PEG, and PF resol in an aqueous solution and reaction at 65 °C for 120 h, ordered aggregates composed of polymerized RF resol/PEG/P123 were obtained. Following further heating at 350 °C for 3 hours, the decomposition of P123 and PEG occurred, leading to the formation of a mesoporous polymer with a 2D hexagonal ordered mesostructure (Fig. 19e). After carbonization, ordered mesoporous carbon was obtained with an average pore size of around 9 nm and an SSA of 563 m^2 g^{-1} (Fig. 19f).[259] Moreover, ordered mesoporous resorcinol/formaldehyde (RF) resin-derived carbon materials with an $Im\bar{3}m$ symmetry could also be prepared by controlling the kinetics of the polymerization of the RF resin.[261]

3.4 Interfacial self-assembly in solution

In general, interfacial self-assembly[262,263] involves the non-covalent packing of BCP micelles associated with organic/inorganic precursors at soft or solid surfaces of different dimensional substrates.[264–266] The subsequent polymerization or cross-linking of the precursors and the removal of BCP templates yield mesoporous materials of different dimensions. This strategy opens pathways for achieving tunable construction of porous heterostructures and controlling their dimensionality. The wide range of interface suppliers (including many 1D–3D functional materials), BCP pore-creating templates, and precursors enable the production of a variety of mesoporous materials with tailorable dimensions and pore structures for potential applications in ESC systems.

3.4.1 1D materials. 1D nanomaterials (*e.g.*, nanowires, nanofibers or nanotubes) have gained enormous interest due to their well-controlled dimensions and axial charge transport.[267–272] Porous 1D materials can further combine the advantages of various pore structures with a specific dimension, affording them direct pathways for charge transfer and larger surface areas for achieving maximum contact between the electrolyte and the electrode.[269,273] Furthermore, they possess excellent mechanical flexibility and the ability to resist volume variation, which are desirable for flexible micro-electrodes.[274,275] In principle, almost all 1D materials can be employed as interface suppliers if suitable interfacial interactions are utilized. In recent years, much effort has been devoted to the utilization of 1D carbon materials,[276–278] metals,[279] and metal oxides[280] as the interface suppliers for the construction of 1D porous nanohybrids *via* interfacial self-assembly approaches.

By using carbon nanotubes (CNTs) as the 1D template and PS-*b*-PEO as the pore-creating agent, Liu *et al.* designed an effective strategy for the construction of 1D porous conducting polymer/carbon nanohybrids (Fig. 20a and b).[276] The approach involved the co-assembly of CNTs with oxygen-containing functional groups (such as –COOH and –OH) on the surface, pyrrole molecules and PS-*b*-PEO spherical micelles in an aqueous solution. Through hydrogen bonding, the pyrrole molecules were adsorbed in the PEO coronae of the micelles, which further packed tightly on the surface of the CNTs. After the polymerization of pyrrole molecules and the removal of the BCP template, 1D mesoporous polypyrrole/CNT (PPy/CNT) hybrid was produced with a mean pore diameter of 12 nm.[276]

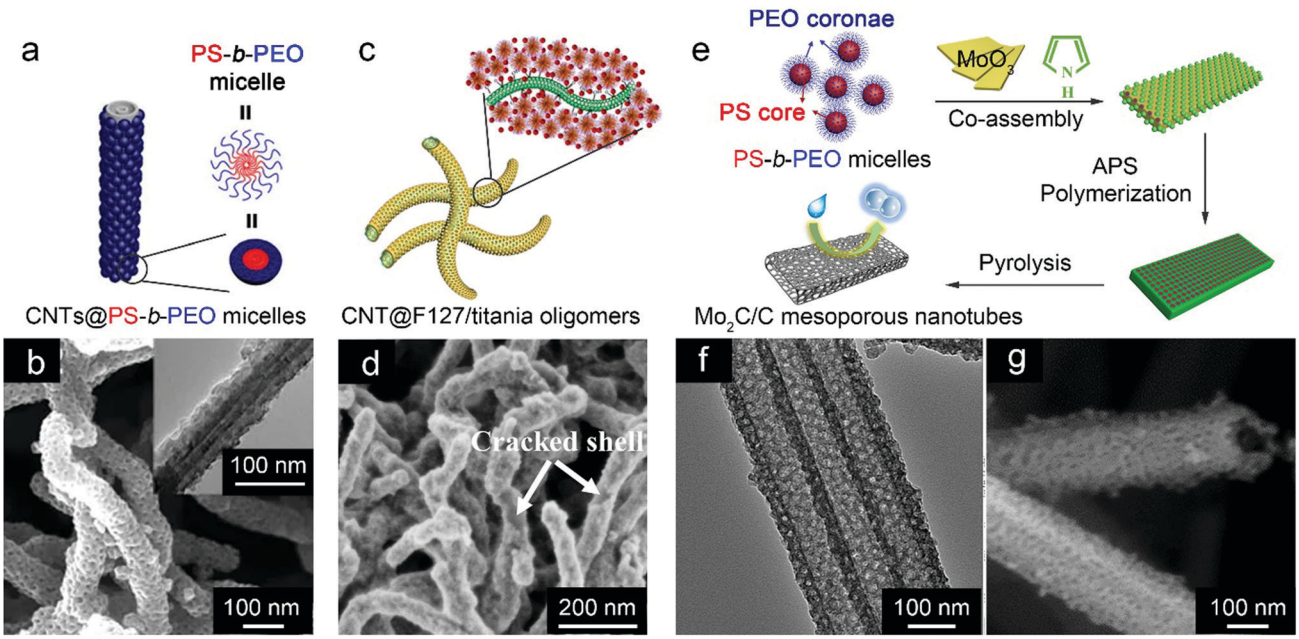

Fig. 20 1D mesoporous nanomaterials prepared *via* interfacial self-assembly in solution. (a) Illustration of carbon nanotubes (CNTs) wrapped by PS-*b*-PEO micelles. (b) SEM image of mesoporous PPy shells on CNTs (inset: TEM image). (a and b) Reproduced with permission.[276] Copyright 2015, Nature Publishing Group. (c) Schematic representation of the preparation of the flexible mesoporous CNT@TiO_2 hybrids with a thin mesoporous anatase shell. (d) SEM image of the flexible mesoporous TiO_2/CNT hybrids. (c and d) Reproduced with permission.[278] Copyright 2016, Elsevier. (e) Schematic diagram of the synthesis of Mo_2C/C hybrid mesoporous nanotubes by a dual-template self-assembly approach. (f) TEM and (g) SEM images of the Mo_2C/C mesoporous nanotubes. (e–g) Reproduced with permission.[280] Copyright 2018, American Chemical Society.

Through a similar strategy, Liu *et al.* prepared mesoporous TiO_2/CNT hybrid nanotubes by coating an ultrathin mesoporous crystalline TiO_2 shell (~20 nm in thickness) on CNTs (Fig. 20c and d).[278] The obtained flexible hybrid nanotubes exhibited uniform accessible mesopores (6.2 nm) and a high SSA of 137 $m^2\ g^{-1}$.

Mai and colleagues synthesized mesoporous Mo_2C/carbon hybrid nanotubes by using MoO_3 nanobelts as both 1D template and the Mo_2C precursor (Fig. 20e).[280] In an aqueous solution, the interfacial self-assembly of PS-*b*-PEO spherical micelles containing pyrrole molecules in the PEO coronae resulted in the close packing of the micelles on the MoO_3 nanobelts. After the polymerization of pyrrole, initiated by ammonium persulphate (APS), ammonia was added to convert MoO_3 to MoO_4^{2-} ($MoO_3 + 2NH_3{\cdot}H_2O \rightarrow 2NH_4^+ + MoO_4^{2-} + H_2O$), which was then absorbed in the PPy network through Mo–N coordination. The amount of ammonia controlled the mass of etched MoO_3 and consequently the loading content of Mo_2C particles in the final hybrid nanotubes. The pyrolysis at 800 °C under nitrogen atmosphere converted PPy to N-doped carbon and Mo species to Mo_2C NPs, which were embedded within the carbon domain, thus generating mesoporous Mo_2C/carbon hybrid nanotubes (Fig. 20f and g) with uniform spherical pores (~18 nm in diameter), an average wall thickness of 18 nm, a maximum SSA of 377 $m^2\ g^{-1}$, and an optimum Mo_2C content of 40 wt%.[280]

3.4.2 2D materials. The growth of mesoporous layers on the surface of 2D materials may lead to various mesoporous nanosheets.[44,197,264,281,282] In particular, patterning mesoporous electrochemically active moieties on freestanding nanosheets, such as graphene oxide (GO) and other inorganic nanosheets (*e.g.*, TiO_2, MoS_2, *etc.*)[283–285] can generate 2D sandwich-structured mesoporous nanohybrids.[276,286,287] This methodology may prevent the aggregation of pristine nanosheets and increase their surface areas, which are desirable for enhancing the electrochemical performance in ESC devices.[197,288–290] As such, great efforts have been devoted to fabricating 2D sandwich-structured porous nanohybrids through interfacial self-assembly protocols.

In 2015, Zhao and colleagues reported a general strategy to grow single-layer ultrathin mesoporous carbon films by interfacial self-assembly of BCP micelles on various substrates (Fig. 21a).[281] The resulting mesoporous films possessed only a single layer of mesopores, while they could grow up to inch size in the plane. By this strategy, ultrathin mesoporous carbon films on different types (*e.g.*, metal oxides, carbon) of substrates with various morphologies (*e.g.*, flexible and patterned substrates)

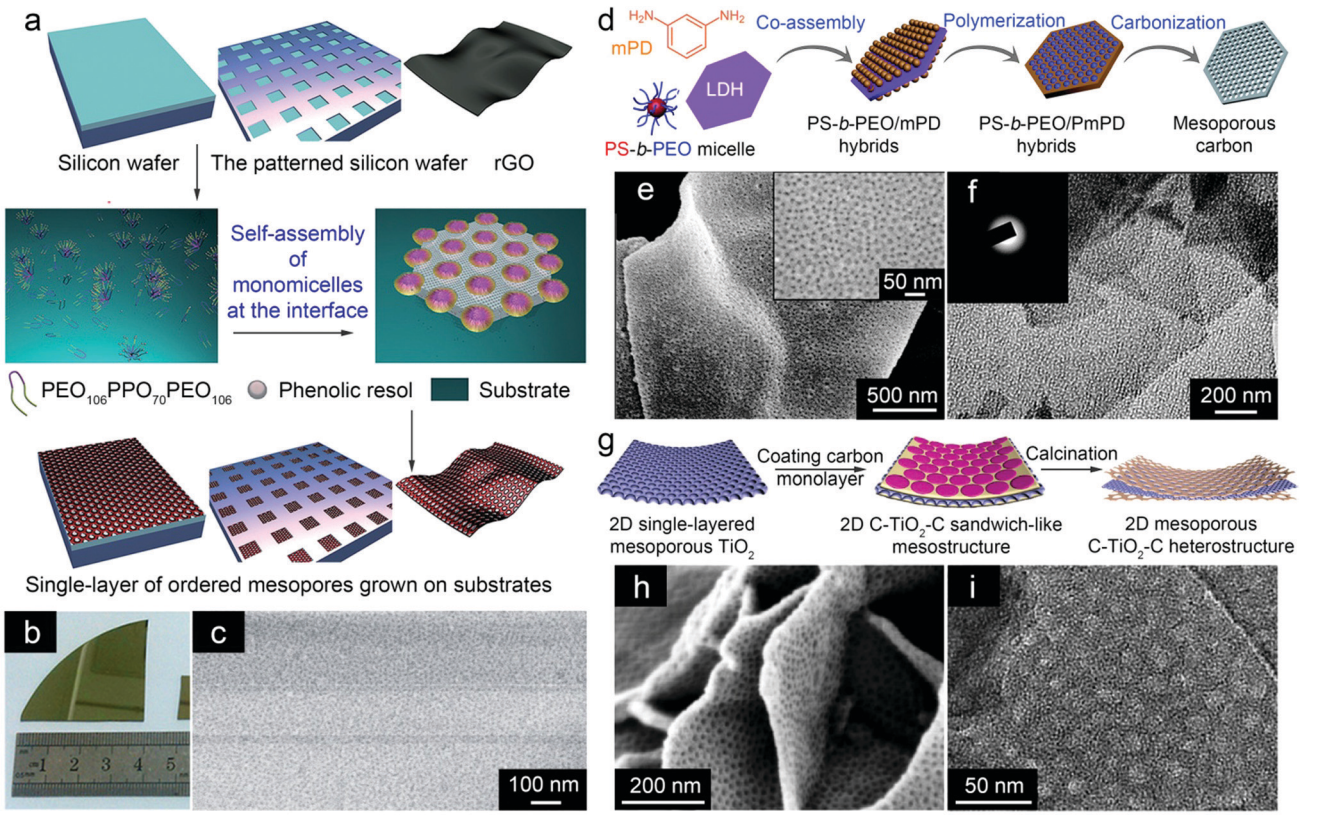

Fig. 21 2D mesoporous films or nanosheets prepared by interfacial self-assembly in solution. (a) Interfacial self-assembly of monomicelles to form single-layer mesoporous polymer/carbon thin films on various 2D substrates. (b) Optical images of large-scale mesostructures grown on silicon wafer surfaces. (c) HR-SEM image of ordered mesoporous carbon structures on silicon wafer surfaces. (a–c) Reproduced with permission.[281] Copyright 2015, Wiley-VCH. (d) Schematic illustration of a dual-template self-assembly strategy for the preparation of holey mesoporous carbon nanosheets. (e) SEM and (f) TEM images of N-doped mesoporous hexagonal carbon nanosheets. (d–f) Reproduced with permission.[291] Copyright 2018, Royal Society of Chemistry. (g) Bottom-up synthesis of a 2D monolayered mesoporous carbon@TiO_2@carbon heterostructure. (h) SEM and (i) TEM images of the carbon@TiO_2@carbon heterostructure. (g–i) Reproduced with permission.[292] Copyright 2019, American Chemical Society.

were obtained. Taking the coating of a mesoporous carbon layer on a 2D silicon wafer modified with Al_2O_3 as an example (Fig. 21b), in an aqueous solution F127 and phenolic resol molecules first co-assembled into spherical composite monomicelles, which were further adsorbed on the surface of the Al_2O_3 substrate *via* electrostatic attraction and hydrogen bonding. Under hydrothermal treatment at 130 °C, the resol molecules covering the micelles were polymerized. After carbonization at 700 °C, the F127 template was removed and an ordered mesoporous carbon layer was achieved on the Al_2O_3 substrate. The mesoporous carbon films had an area of 1×1 cm^2 to one-quarter of a 3 inch depending on the scale of the silicon wafer substrates (Fig. 21b and c). The carbon films could be transferred to other substrates by a stamp transfer method. The mesoporous films exhibited a uniform pore size of 9 nm and an average thickness of *ca.* 1 nm.[281] The key to controlling the thickness of the nanosheets was the low concentration of monomicelle close-packing assembly.[264] At a low concentration, heterogeneous nucleation of monomicelles on the substrate *via* electrostatic attraction was superior to the close-stacking of monomicelles by spontaneous nucleation. Therefore, a single layer of the monomicelles was formed on the substrate, which enabled the formation of ultrathin nanosheets. The interfacial self-assembly of monomicelles has also been demonstrated on flexible substrates, such as GO. In 2016, Lou and coworkers reported the interfacial self-assembly of monolayers of F127/polydopamine composite micelles on both sides of GO nanosheets through hydrogen bonding.[287] The tightly packed composite micelles were converted into mesoporous carbon layers sandwiching GO sheets through pyrolysis under nitrogen atmosphere.

As an example of utilizing free-standing inorganic nanosheets as the 2D template, Mai and colleagues reported the synthesis of 2D mesoporous carbon sheets using layered double hydroxide (LDH) sheets as a sacrificial template, as LDH could be dissolved in an acidic solution (Fig. 21d).[291] PS-*b*-PEO spherical micelles with *m*-phenylenediamine monomers adsorbed in the PEO corona were attracted to the surface of LDH nanosheets through hydrogen bonding and electrostatic interactions. After the polymerization of *m*-phenylenediamine, 2D freestanding poly(*m*-phenylenediamine) nanosheets with holey pores were obtained through the self-sacrifice of the LDH template, which could be dissolved gradually by the acid formed during the polymerization of *m*-phenylenediamine. The obtained carbon nanosheets had an average pore size of 16 nm and an SSA of 256 m^2 g^{-1} (Fig. 21e and f).[291] In another interesting example, Zhao's group reported the construction of a 2D sandwich-like mesoporous carbon@TiO_2@carbon heterostructure (Fig. 21g).[292] They first prepared mesoporous TiO_2 nanosheets through a solution-based nanoprecipitation method. Then, two monolayers of F127/dopamine composite micelles were coated on both surfaces of the mesoporous TiO_2 nanosheets. Following the polymerization of dopamine and subsequent carbonization, a 2D mesoporous carbon@TiO_2@carbon sandwich-like heterostructure (Fig. 21h and i) was formed. The mesopore sizes of the exterior carbon and interior titania layers were approximately 15 and 3 nm, respectively. The surface area and pore volume of the 2D heterostructure were 267 m^2 g^{-1} and 0.34 cm^3 g^{-1}, respectively.[292]

Building on a similar principle, the growth of 2D mesoporous conducting polymers on 2D freestanding surfaces has been achieved as well.[276] In 2015, Liu *et al.* developed a universal strategy for coating freestanding nanosheets with mesoporous conducting polymers in aqueous solutions (Fig. 22a–i).[276] In their approach, a series of ultrathin freestanding nanosheets, including GO, MoS_2, TiO_2, and exfoliated graphene, were used as the 2D templates. The co-assembly of PS-*b*-PEO spherical micelles and pyrrole monomers on the surfaces of these nanosheets through hydrogen bonding or electrostatic interactions resulted in the tight packing of the micelles with pyrrole molecules in the PEO corona on the nanosheets. Following polymerization of the pyrrole monomers, PPy networks were generated. The subsequent removal of the BCP template by solvent dissolution gave rise to sandwich-structured mesoporous hybrid nanosheets. The thickness, pore size, and SSA of the resulting hybrid nanosheets could be tailored by simply adjusting the PS block length of the PS-*b*-PEO template.[276]

Mai's group extended the interfacial self-assembly concept to 2D soft material surfaces. They employed lamellae formed by small-molecule surfactants as the 2D template for synthesizing monolayer mesoporous conducting polymer nanosheets.[286,293] For example, octadecylamine was utilized to form ultrathin lamellae in an ethanol/H_2O mixture (Fig. 22j).[293] On the other side, PS-*b*-PEO copolymers self-assembled into spherical micelles in a THF/H_2O mixed solvent. After mixing the solutions of the micelles and the lamellae, the micelles could be adsorbed on both surfaces of the lipid lamellae, driven by the hydrogen bonding between the PEO chains and $-NH_2$ groups. Subsequently, pyrrole monomers were added into the mixed solution, which could be adsorbed in the PEO domains and then polymerized into a PPy polymeric network after the addition of a catalyst. The removal of the BCP templates by solvent washing yielded monolayer mesoporous PPy nanosheets. By selecting PS-*b*-PEO templates with different PS block lengths, the resultant PPy nanosheets (Fig. 22k and l) were endowed with tunable thicknesses (25–30 nm), pore sizes (6.8–13.6 nm) and SSAs (73–96 m^2 g^{-1}).[293] By virtue of precise structural control and easy template removal, the interfacial self-assembly on 2D lipid bilayers provided a versatile platform for the construction of 2D freestanding monolayer mesoporous materials.

During the synthesis of mesoporous carbons or conducting polymers, the incorporation of metallic or metal oxide species into the mesoporous layers can be accompanied during the interfacial self-assembly.[11,294,295] For instance, Mai and colleagues synthesized 2D sandwich-like mesoporous carbon nanosheets with incorporated Mo_2C NPs in the co-assembly process of GO, PS-*b*-PEO, and pyrrole monomers.[294] When the polymeric micelles, coupled with pyrrole molecules that were adsorbed on the PEO domain, were closely packed on both surfaces of GO through hydrogen bonding, the Mo source ($Mo_7O_{24}^{6-}$ ions) was co-adsorbed with pyrrole molecules *via* the Mo–N coordination. Then, pyrrole molecules on the GO surface were polymerized into continuous PPy networks, yielding PPy–$Mo_7O_{24}^{6-}$/copolymer/GO composite nanosheets. After pyrolysis of the 2D nanocomposites, sandwich-structured mesoporous N-doped carbon/Mo_2C/reduced

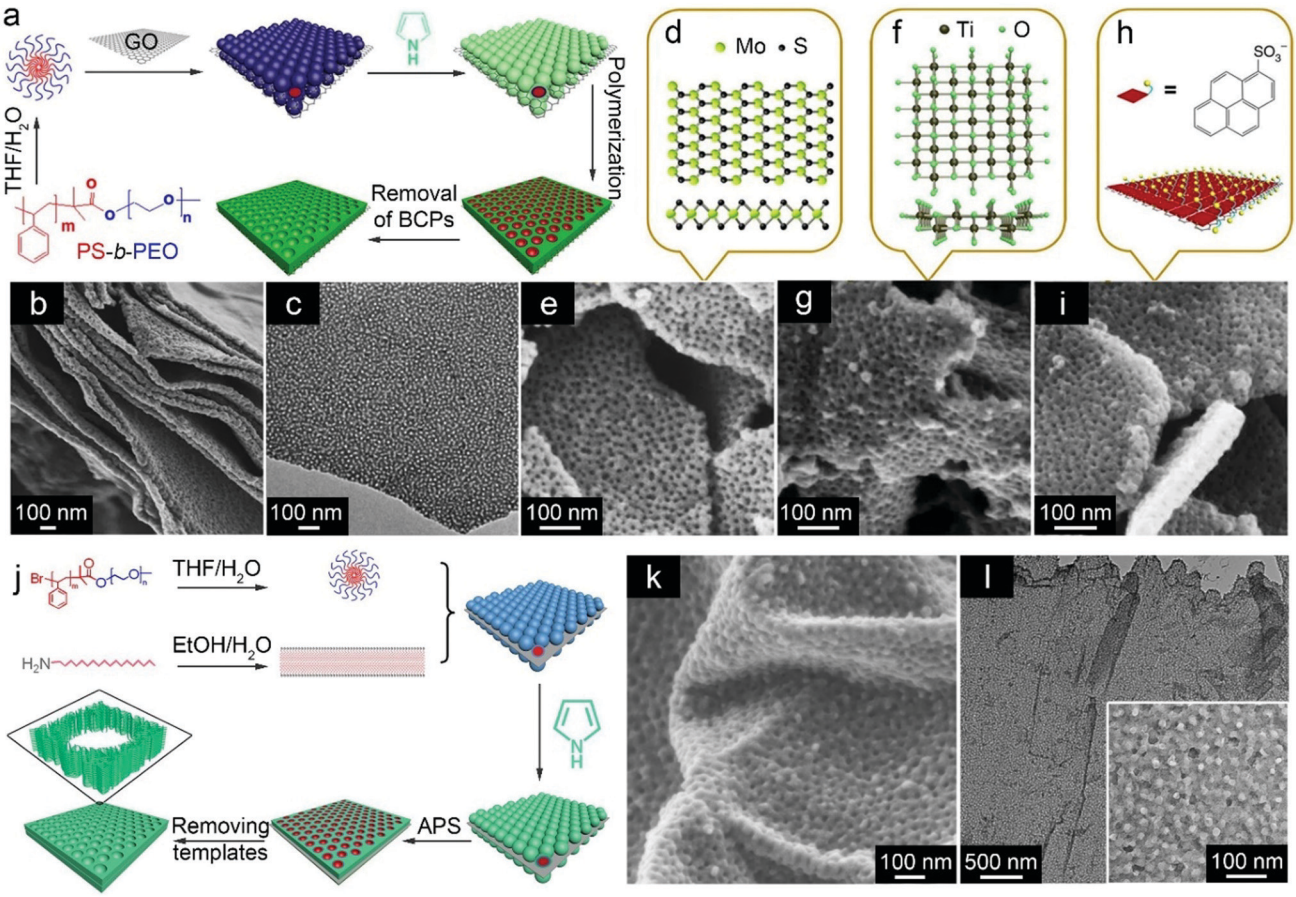

Fig. 22 2D mesoporous conducting polymers synthesized *via* interfacial self-assembly in solution. (a) Patterning 2D surfaces with mesoporous conducting polymer nanosheets. (b) SEM and (c) TEM images of the formed mesoporous PPy nanosheets on the GO substrate. (d) Structure of MoS_2 nanosheets (top view, upper; side view, lower) and (e) SEM image of large-pore mesoporous PPy layers on MoS_2 nanosheets. (f) Structure of TiO_2 nanosheets in the [010] (upper) and [001] (lower) directions and (g) SEM image of large-pore mesoporous PPy nanosheets on TiO_2. (h) Illustration of the 1-pyrenesulfonic acid sodium salt-modified exfoliated graphene surfaces. (i) SEM image of large-pore mesoporous PPy nanosheets on exfoliated graphene nanosheets following modification with 1-pyrenesulfonic acid sodium salt. (a–i) Reproduced with permission.[276] Copyright 2015, Nature Publishing Group. (j) Schematic illustration of the synthesis of 2D mesoporous PPy nanosheets using 2D lipid bilayers as the 2D templates. (k) SEM and (l) TEM images of the mesoporous PPy nanosheets. (j–l) Reproduced with permission.[293] Copyright 2016, Wiley-VCH.

graphene oxide (mNC–Mo_2C@rGO) nanohybrids with well-defined spherical pores were produced. The prepared mNC–Mo_2C@rGO nanosheets with embedded small Mo_2C NPs (with a small average diameter of ~4 nm) possessed average pore sizes of ~13 nm and large SSAs of up to 389 $m^2 g^{-1}$.[294] In another case, the polymerization of pyrrole monomers on both sides of GO was triggered by $FeCl_3$, which could be simultaneously adsorbed on the resulting PPy network through Fe–N coordination.[11] The resulting mesoporous PPy/rGO nanosheets with incorporated Fe_2O_3 NPs possessed tunable pore sizes (14–23 nm), mean thicknesses (34–52 nm), and SSAs (111–248 $m^2 g^{-1}$), depending on the PS block length of the PS-*b*-PEO template.[11] 2D mesoporous metal nanosheets have also been achieved by interfacial self-assembly strategy. Xu and coworkers recently reported the synthesis of ultra-thin mesoporous Pt nanosheets by combining a highly ordered arrangement of BCP micelles on a silicon substrate and a suitably designed chemical reduction.[296] They employed the co-assembly of PS-*b*-P2VP-*b*-PEO and Pt precursor (H_2PtCl_6) to form composite spherical micelles through a dialysis method, and then the composite micelles were spin-coated on a silicon substrate in a well-ordered monolayer fashion. Next, a two-step reduction procedure using dimethylaminobenzaldehyde vapor (for nucleation) and ascorbic acid (for further growth) as the reduction agents was implemented, which enabled a complete Pt deposition and consequently the formation of continuous Pt nanosheets. Eventually, mesoporous Pt nanosheets were obtained after the removal of the BCP micelles.[296]

When employed as electrode materials, the stacking of mesoporous nanosheets with spherical pores could impede the smooth in-plane mass transport. This problem can be overcome by introducing in-plane cylindrical pores on the surface of nanosheets by taking advantage of an interfacial self-assembly strategy, which was demonstrated by Mai and colleagues (Fig. 23).[12] The strategy involves the co-assembly of P123 cylindrical micelles, monomers (*e.g.*, pyrrole, aniline, or dopamine), and GO in a mixed solvent system (Fig. 23a). Driven by hydrogen bonding, the cylindrical micelles tightly packed on the GO surface, while adsorbing the monomers in the PEO domains. The subsequent polymerization

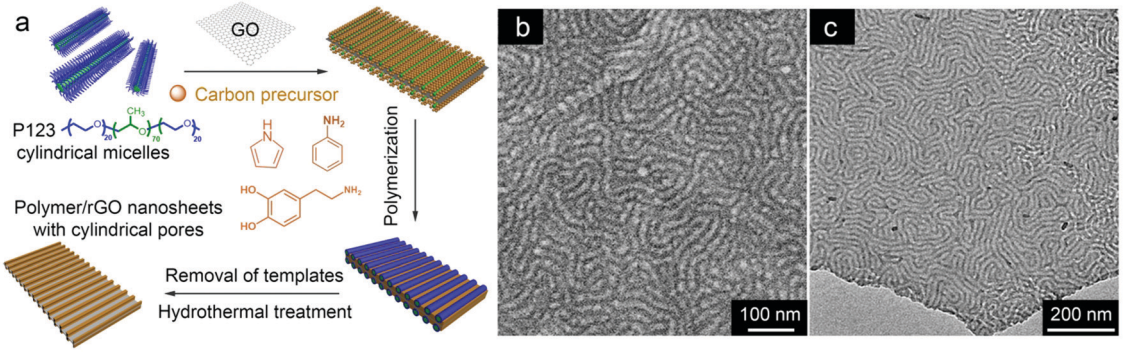

Fig. 23 Interfacial self-assembly engineering of 2D mesoporous nanosheets with in-plane cylindrical pores. (a) Schematic illustration of the fabrication of 2D mesoporous polymer/rGO nanosheets with in-plane cylindrical pores by an interface self-assembly strategy. (b) SEM and (c) TEM images of the resulting sandwich-like mesoporous PPy/rGO nanosheets with in-plane cylindrical pores on both surfaces. Reproduced with permission.[12] Copyright 2019, Wiley-VCH.

of the monomers led to the formation of a continuous polymeric network. After the removal of the P123 template and subsequent hydrothermal treatment, mesoporous polymeric monolayers with cylindrical mesopores on the surface of rGO were achieved (Fig. 23b and c). The resulting 2D sandwich-like nanohybrids had average pore diameters of ~12 nm and high SSAs of up to 157 $m^2 g^{-1}$. They also demonstrated that the parallel cylindrical mesopores offered in-plane pathways for smoother and faster ion diffusion compared with spherical pores, affording the nanohybrids great potential applications in 2D planar energy storage devices.[12] In another study, they also demonstrated the interfacial self-assembly of cylindrical micelles on the surface of 2D inorganic hard templates (*e.g.*, MoS_2) to fabricate various mesoporous nanohybrids with in-plane cylindrical pores, thus demonstrating the universality of this methodology.[10]

3.4.3 3D materials. Similar to the synthesis of 1D or 2D mesoporous materials, 3D mesoporous materials can be constructed by using 3D templates, such as inorganic particles, 3D aerogels, *etc.*, while the mesopores originate from BCP micelles.[297–300] For instance, core–shell structures can be easily obtained through coating mesoporous layers on the surfaces of diverse 3D polymeric or inorganic particles, producing various core–shell functional materials.[287,301–304] Taking a recent classical study as an example, Lan *et al.* demonstrated a precise manner for constructing core–shell functional nanoparticles by coating single-layer ordered mesoporous crystalline TiO_2 on various inorganic particles, including SiO_2 nanospheres, carbon nanospheres, and Fe_2O_3 ellipsoids (Fig. 24a).[304] First, titania oligomer composite monomicelles formed from Pluronic F127 and tetrabutyl titanate were prepared in a hydrochloric acid/THF solution through the slow evaporation of THF. A sol–gel process was then initiated by mixing the titania monomicelles and inorganic particles (as the final cores) in ethanol/glycerol mixed solvent under stirring. High-viscosity glycerol as a co-solvent enabled the monomicellar self-assembly in a spatially confined direction, and decreased the hydrolysis and condensation rates of titania oligomers by adhering to the titania monomicelles. As a result, the formed TiO_2 shells (Fig. 24b) possessed a monolayer of mesopores, a high surface area (119 $m^2 g^{-1}$), and a large mean mesopore size (9.8 nm). Moreover, the precise control by this confined assembly approach enabled the formation of TiO_2 shells containing one to five mesoporous layers (Fig. 24b–f), and the mesopore diameter could be tuned from 4.7 to 18.4 nm by changing the amount of the swelling agent (trimethylbenzene).[304]

Based on similar principles for the synthesis of core–shell structures, hollow or yolk–shell structures can be constructed by completely or partially etching the core materials. Yamauchi and co-workers reported the formation of mesoporous hollow N-doped carbon spheres, where they used silica NPs as the hard template, PS-*b*-PEO as the soft template for generating mesopores in the shell, and dopamine as the N-rich carbon precursor.[301] As shown in Fig. 24g–j, the principle for the preparation of mesoporous carbon spheres is similar to the previously introduced monomicelle close-packing assembly approach for fabricating 1D or 2D mesoporous materials, except for the used template. After the formation of core–shell nanospheres with N-doped mesoporous carbon shells, the silica templates were etched with hydrofluoric acid, yielding N-doped hollow carbon spheres (Fig. 24j), which had inner cores of approximately 350 nm in size, mesoporous carbon shells with a mean pore size of 20 nm, and a high SSA of 427 $m^2 g^{-1}$.[301] Using a similar strategy, hollow mesoporous metal particles could also be fabricated.[305,306] Taking the preparation of trimetallic PtPdCo polyhedra with hollow cavities as an example,[305] in the first step, Pd@PtPdCo core–shell mesoporous nanopolyhedra (Pd@PtPdCo MNPs) were first prepared by a simple chemical reduction reaction. During this step, Pd@PtPdCo MNPs were prepared by a one-step co-reduction, in which the mixture of the precursors of Pt, Pd, and Co interacted with F127 micelles to form metal precursor/F127 composite micelles. Here, F127 served as both pore-forming and protective agents for preventing particle aggregation. In the second step, the Pd cores of the Pd@PtPdCo MNPs were selectively etched to produce trimetallic PtPdCo nanopolyhedra with hollow cavities with an average diameter of 105 nm and well-defined mesoporous structure.[305] By controlling the degree of etching, Lou's group constructed mesoporous yolk–shell structures.[287] In a typical study, the F127–dopamine composite micelles first interacted with Fe_2O_3 quasi-cubes to form core–shell

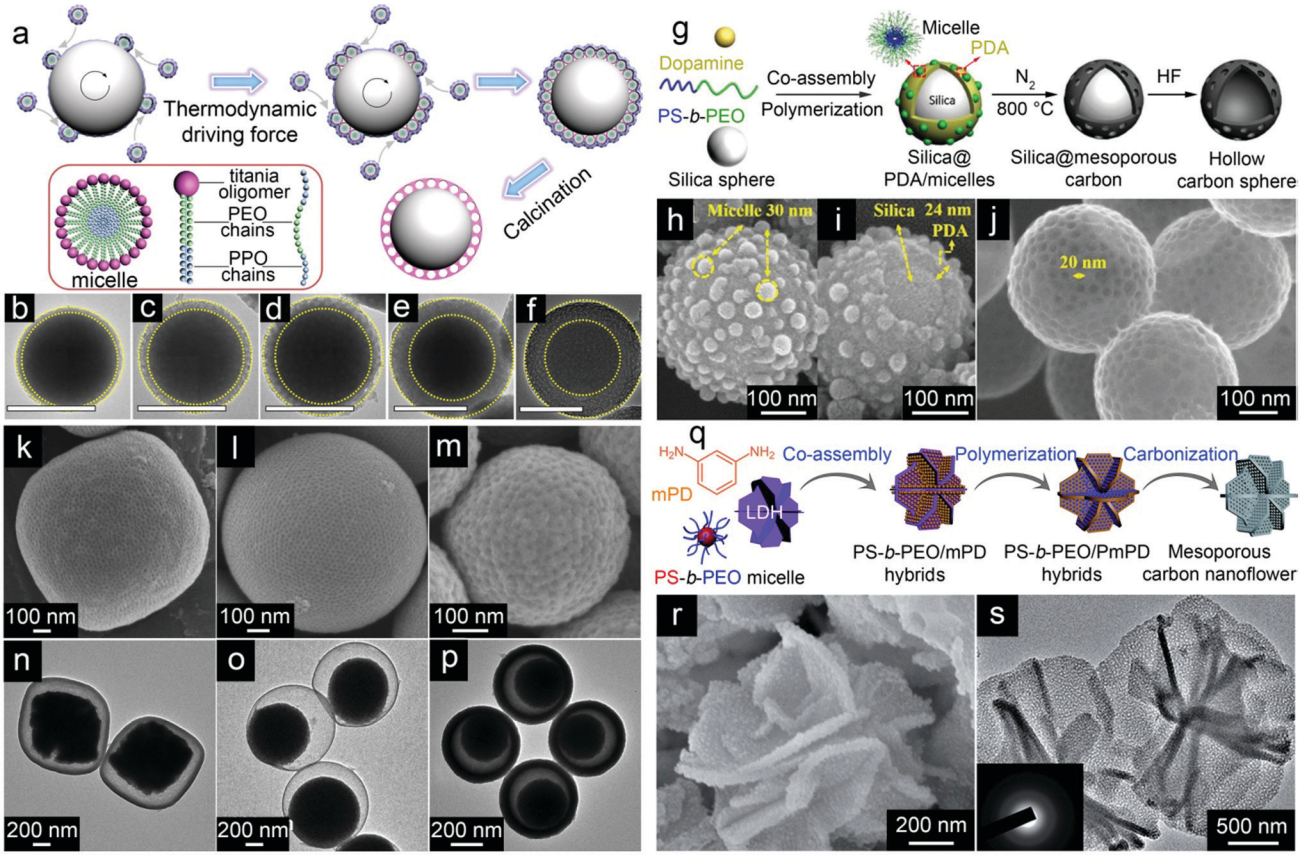

Fig. 24 3D mesoporous particles prepared through interfacial self-assembly in solution. (a) Schematic illustration of coating single-layer mesoporous titania on silica spheres *via* confined interfacial monomicelle assembly. (b–f) TEM images of SiO_2@$mTiO_2$ core–shell structures with TiO_2 shells consisting of one to five mesoporous layers. All scale bars represent 200 nm. (a–f) Reproduced with permission.[304] Copyright 2019, Elsevier. (g) Schematic illustration of the preparation of nitrogen-doped hollow carbon spheres. (h and i) SEM images of the silica@PDA/micelles. (j) SEM image of nitrogen-doped hollow carbon spheres. (g–j) Reproduced with permission.[301] Copyright 2016, Royal Society of Chemistry. (k) SEM and (n) TEM images of Fe_2O_3@ mesoporous carbon yolk–shell colloidosome hybrids. (l) SEM and (o) TEM images of SiO_2@mesoporous carbon yolk–shell colloidosome hybrids. (m) SEM and (p) TEM images of SiO_2@TiO_2@mesoporous carbon yolk–double-shell colloidosome hybrids. (k–p) Reproduced with permission.[287] Copyright 2016, Wiley-VCH. (q) Schematic illustration of a dual-template self-assembly strategy towards holey mesoporous carbon nanoflowers. (r) SEM image of PS-*b*-PEO/PmPD nanoflower composites. (s) TEM image of 3D N-doped carbon nanoflowers. (q–s) Reproduced with permission.[291] Copyright 2018, Royal Society of Chemistry.

Fe_2O_3@F127–dopamine quasi-cubic nanohybrids. After the polymerization of dopamine monomers and subsequent thermal treatment, the F127 template was removed and core–shell Fe_2O_3@ mesoporous carbon particles were formed. Next, the partial etching of the quasi-cubic Fe_2O_3 template produced yolk–shell carbon/Fe_2O_3 hybrids with uniform mesopores (Fig. 24k and n). Similarly, by using different 3D particles such as silica spheres and SiO_2@TiO_2 spheres, SiO_2@mesoporous carbon yolk–shell colloidosome hybrids (Fig. 24l and o) and SiO_2@TiO_2@mesoporous carbon yolk–double–shell colloidosome hybrids (Fig. 24m and p) were also achieved.[287]

Alternatively, 3D frameworks consisting of 2D nanosheets may provide ideal templates to make 3D mesoporous materials. Tian *et al.* synthesized 3D carbon nanoflowers consisting of mesoporous carbon nanosheets by employing layered double hydroxide (LDH) nanoflowers as sacrificial 3D templates, PS-*b*-PEO as the pore-creating template and *m*-phenylenediamine as the carbon precursor (Fig. 24q–s).[291] The nanosheet-assembled LDH nanoflowers were prepared by co-precipitation method, which involved the use of nickel and manganese salts as the metal precursors and hexamethylenetetramine as a hydrolyzing agent. Based on the monomicelle close-packing assembly principle, 3D mesoporous carbon nanoflowers with holey pores were produced by sacrificing the LDH nanoflowers. The resulting 3D carbon nanoflower (Fig. 24s) possessed uniform mesopores of 15 nm and a high SSA of 266 $m^2\ g^{-1}$.[291] Liu's group employed graphene aerogels for the preparation of mesoporous carbon monoliths.[307] Graphene aerogels prepared from the hydrothermal treatment of GO typically exhibit macroporosity and good mechanical stability. By tuning the weight ratio of the F127/resol composite micelles to the graphene aerogels, porous graphene aerogels with well-defined in-plane spherical mesopores or cylindrical pores were obtained after carbonization, which had uniform pore sizes of *ca.* 9 nm and SSAs of *ca.* 250 $m^2\ g^{-1}$.[307]

3.5 Emulsion-templating method

Instead of the rigid templates mentioned above, the emulsion-templating method offers a flexible way for incorporating highly

interconnected pores into materials, which largely enhances the mass transport.[190,308–310] The emulsion-templating method has several advantages, including easy removal of the template, feasibility for large-scale production, and environmental friendliness. In emulsion systems, the inner and outer interfaces of emulsion droplets possess two different environments. During the synthesis of mesoporous materials, amphiphilic BCPs serve as both surfactants for stabilizing the emulsion and mesopore-creating agents. Precursor molecules are cross-linked or polymerized within the emulsion droplets or oil/water interfaces owing to the space-confinement effect. The removal of the emulsion and BCPs leads to the production of porous materials with hierarchical porous structures, in which macropores are templated by the emulsion droplets, while the mesopores are constructed by the BCP templates.

Controlling the solubility of precursors in oil and water phases and the interfacial tension on the surface of emulsion droplets provides opportunities for fabricating iso- or anisotropic porous particles that are difficult to prepare by other solution-based protocols.[311–314] For example, Dai and co-workers prepared N-doped porous multichambered carbon microspheres by employing Pluronic F127 and sodium dodecyl benzene sulfonate (SDBS) as dual surfactants, and 2,6-diaminopyridine (DAP) and formaldehyde as carbon precursors (Fig. 25a–e).[77] The multichamber polymers were prepared *via* a two-step polymerization. The first step was the formation of cytoskeleton-like prepolymer of DAP and formaldehyde (donated as DAP-F) microspheres by the dual surfactants. F127 was used as the steric stabilizer to prevent the aggregation of polymer particles. The NH_2 groups of DAP decreased the area of head groups of the negatively charged anionic surfactant SDBS by reducing the electrostatic repulsion of the surfactant, which resulted in the formation of large chambers in DAP-F spheres (Fig. 25b). The second step of polymerization was induced by the addition of acetic acid, which accelerated the

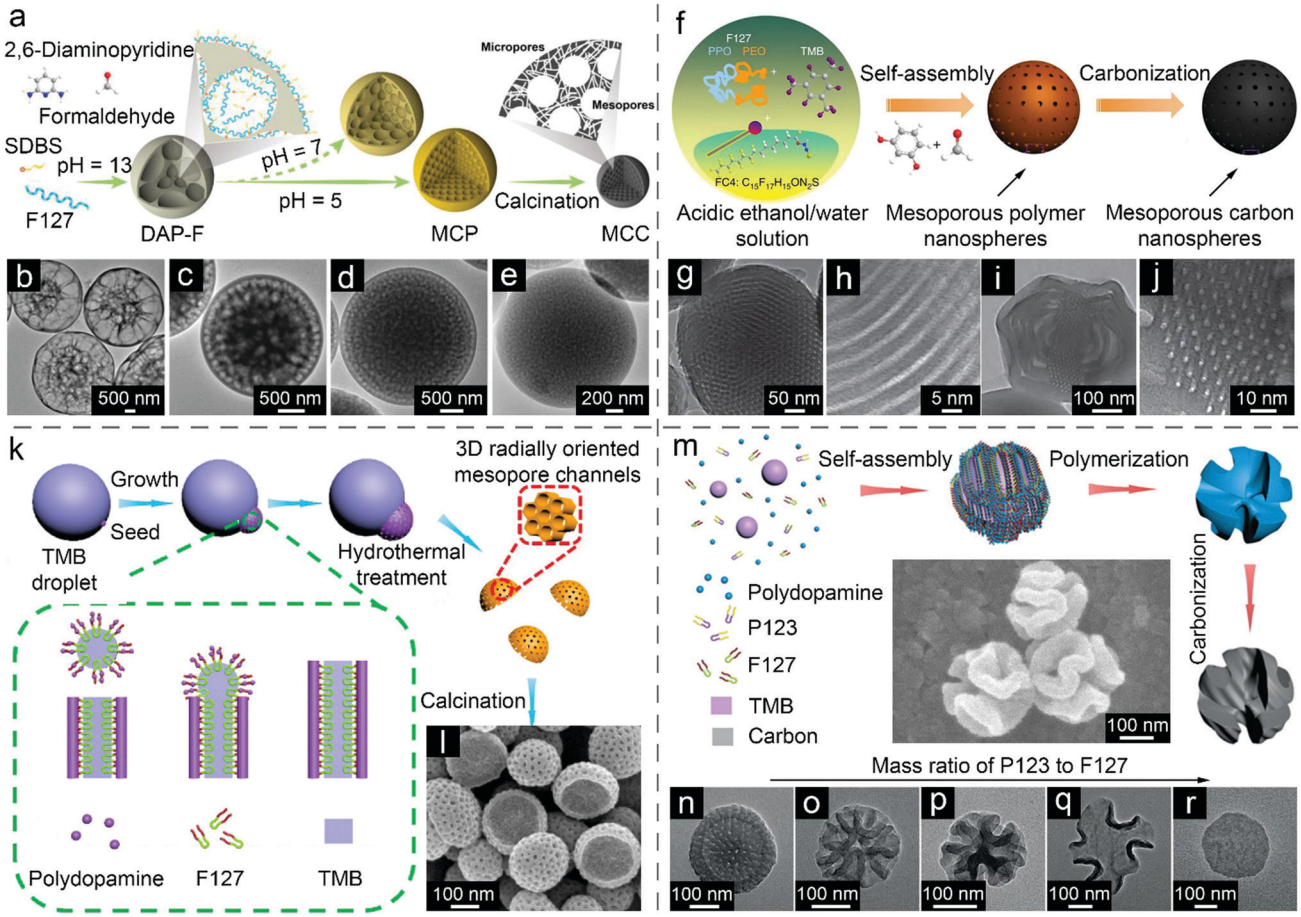

Fig. 25 Emulsion-templating synthesis of iso- or anisotropic mesoporous nanoparticles. (a) Illustration of the synthesis of N-doped multichamber carbons. (b–e) TEM images of (b) cytoskeleton-like prepolymer microspheres, (c) multichamber polymer microspheres formed at pH = 7, (d) multichamber polymer microspheres formed at pH = 5, and (e) N-doped multichamber carbon microspheres. (a–e) Reproduced with permission.[77] Copyright 2019, Wiley-VCH. (f) Schematic illustration of the synthesis of mesoporous carbon nanospheres *via* the self-assembly of mesoporous polymer spheres followed by carbonization. (g–j) TEM images of the mesoporous nanospheres with (g and h) 2D hexagonal (*p6mm*) symmetry and (i and j) the multilayer concave hollow nanospheres. (f–j) Reproduced with permission.[315] Copyright 2013, Nature Publishing Group. (k) Schematic illustration of the formation process of bowl-like mesoporous particles. (l) SEM image of the bowl-like mesoporous carbon particles. (k and l) Reproduced with permission.[76] Copyright 2016, American Chemical Society. (m) Schematic illustration of the formation of walnut-shaped particles. (n–r) TEM images of polydopamine particles prepared with different mass ratios of P123 to F123: (n) 0 : 1, (o) 1 : 15, (p) 1 : 3, (q) 1 : 1, and (r) 5 : 3. (m–r) Reproduced with permission.[316] Copyright 2018, Wiley-VCH.

cross-linking of the DAP-F prepolymer. The confinement of polymerization in microspheres resulted in the space partition of large chambers and the formation of rich chambers inside them. The average diameter of the multichambered polymers could be tuned in the range of 250–3091 nm by varying the mass ratio of SDBS and F127. The multichambered polymers (Fig. 25d) were carbonized and activated by CO_2 to obtain multichambered carbon microspheres with microporous shells and high SSAs of up to 1797 $m^2\ g^{-1}$ (Fig. 25e).[77] On the other hand, emulsion droplets may assist with the formation of NPs with ordered mesophases.[315] Cationic fluorocarbon surfactant and Pluronic F127 were used as templates; ethanol and 1,3,5-trimethylbenzene (TMB) were employed as organic co-solvents; resorcinol and formaldehyde (RF) were selected as carbon precursors. By tuning the interfacial energy and interactions between the composites in the emulsion system, as well as the polymerization rate of the carbon precursors, mesoporous RF resin spheres with two main morphologies were obtained by the self-assembly of RF together with emulsion droplets through hydrogen bonding (Fig. 25f). After calcination at 800 °C under N_2 flow, mesoporous carbon NPs with different morphologies were obtained, including mesoporous nanospheres with 2D hexagonal (*p6mm*) symmetry (Fig. 25g and h) and multilayered concave hollow nanospheres (Fig. 25i and j). The mesoporous carbon nanospheres had an average pore size of 3 nm and SSAs of 640–857 $m^2\ g^{-1}$. Interestingly, the mesoporous carbon nanospheres with 2D hexagonal symmetry could be transformed into multilayered concave hollow nanospheres by increasing the amount of ethanol or TMB, the concentration of surfactant, or decreasing the initial reaction temperature, due to the thermodynamic change of hydrophobicity of the surfactants, which accordingly altered their packing parameters in the assemblies.[315]

Emulsion droplets also provide desirable templates for the construction of anisotropic NPs.[317–323] For example, Lou's group demonstrated an emulsion-induced interface anisotropic self-assembly strategy to achieve uniform bowl-like mesoporous carbon particles with radially-oriented mesochannels.[76] In this case, the emulsion system is formed by sonication of two immiscible liquids, including 1,3,5-trimethylbenzene (TMB) and water (Fig. 25k). Then, F127, TMB, and dopamine formed composite micelles through the hydrogen bonding between F127 and polydopamine and the swelling effect of TMB on PPO chains of F127. After the addition of the swelling agent, island-shaped mesostructured polydopamine seeds assembled by F127/TMB/polydopamine composite micelles were generated at the TMB/water interface. Then, the cooperative self-assembly of the composite micelles drove the oriented growth of mesochannels from the micelles along the radial direction within the particles, generating bowl-like polydopamine particles with radially oriented mesopores (Fig. 25l). After carbonization, the as-formed carbon NPs exhibited mesochannels with an average diameter of ~8 nm and a high SSA of 619 $m^2\ g^{-1}$.[76] In a related study, this group prepared walnut-shaped N-doped carbon NPs with ultra-large channels through the addition of extra P123 in the above-discussed system (Fig. 25m).[316] By finely tuning the packing parameters of P123 and F127, a series of anisotropic N-doped carbon NPs were obtained (Fig. 25n–r). When the P123/F127 mass ratio was increased from 0:1 to 1:15 and then to 1:3, the resulting mesoporous particles transformed from a bowl-like structure with 2D hexagonal columnar channels (Fig. 25n) to a dendritic architecture with radially-oriented mesochannels (Fig. 25o), and then to walnut-shaped particles with a bicontinuous pore structure (Fig. 25p). When the P123/F127 mass ratio was further increased to 1:1 and 5:3, nonporous crumpled nanosheets (Fig. 25q) and nanodisks (Fig. 25r) were formed, respectively. The resulting carbon NPs possessed porous structures. Taking the walnut-shaped particles as an example, they had pore sizes in the range of 13–50 nm and an SSA of 150 $m^2\ g^{-1}$.[316]

Nanoparticle-stabilized emulsions, namely, Pickering emulsions, have also been employed as templates for the synthesis of mesoporous materials. Yang and coworkers developed a novel method to synthesize mesoporous carbon microspheres (MCMs) with controlled interior structures, based on BCP assembly within the droplet-confined space in Pickering emulsion (Fig. 26).[324] Water droplets in silica NP-stabilized Pickering emulsions were used as spherical templates (Fig. 26a). With the co-assembly of phenolic resol and F127, the polymerization of phenolic resol both at the toluene/water interface and inside the water droplets yielded polymeric microspheres with big outer crusts and inner ordered mesostructures. The slight change of each variable in the emulsion system could induce rich evolution of particle morphology (Fig. 26b). By adjusting the synthetic parameters, the enclosed liquid mixture of oil, water, and nanomicelle composites underwent microphase changes, resulting in a library of MCMs,

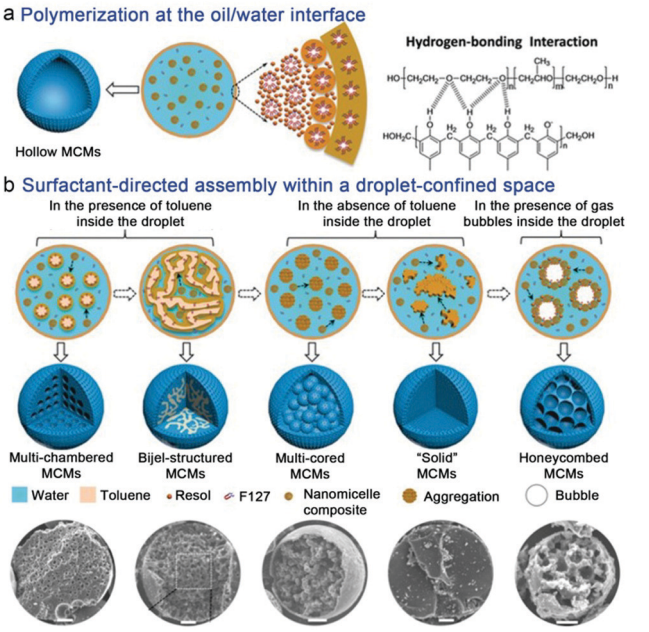

Fig. 26 Synthesis of mesoporous carbon microspheres with the assistance of Pickering emulsion as the template. (a) Schematic illustration of the interfacial polymerization of phenolic resol in the presence of Pluronic F127 at the toluene/water interface. (b) Schematic illustration of evolution of interior-structured MCMs and their corresponding SEM images. Scale bar: 10 mm. Reproduced with permission.[324] Copyright 2018, Wiley-VCH.

including multi-chambered, bijel-structured, multi-cored, and honeycombed MCMs.[324]

4. Applications of BCP-templated mesoporous materials

Mesoporous materials exhibit a diversity of potential applications in ESC devices, such as rechargeable batteries,[269] supercapacitors,[325] electro- or photo-catalysis,[194] and solar cells.[2] Compared with microporous materials, mesoporous materials have shown some incomparable advantages. Although microporous materials have large surface area, many micropores are closed or exhibit narrow bottle-necks, which are difficult to immerse by electrolyte, especially large-sized organic electrolyte molecules, leading to poor utilization of the surface area. In addition, smaller pores (<0.5 nm) are usually inaccessible by hydrated ions, leading to the poor wettability of microporous materials.[326–328] In contrast, the large mesopores of mesoporous materials may provide faster ion/electrolyte transport pathways, which are favorable for achieving high capacitive performance at high current densities. Based on these reasons, many mesoporous materials show better electrochemical performance in ESC devices compared to their microporous counterparts.[329–331] Furthermore, for some energy storage applications requiring the incorporation of metal or metal oxide nanoparticles, such as electrode materials of batteries and supercapacitors, mesoporous materials with large mesopores are desirable loading carriers as the sizes of the nanoparticles are generally larger than the scale of micropores. Meanwhile, porous structures can better accommodate strain relaxation and prevent structural collapse during repeated electrochemical or electrocatalytic cycling. On the other hand, the dimensionality of the materials determines their potential applications in ESC devices. For example, 1D materials are suitable for the construction of fiber- or wire-like electrodes in weavable or wearable devices.[267,332] 2D materials have received enormous interest in 2D flexible planar devices due to their high areal packing density, short mass transport distance, and good flexibility.[333,334] 3D materials are usually dominant in energy devices with relatively large volume electrodes, which provide more opportunities for controlling the device functionality and performance.[297] In this section, we introduce typical applications of mesoporous materials with different dimensionalities and/or pore architectures in ESC devices.

4.1 Rechargeable batteries

The rapid development of various modern applications, from portable electronics to automobiles, has brought increasing demands for rechargeable batteries. In this subsection, we introduce the utilization of mesoporous materials as electrode materials in two popular types of secondary batteries, including alkali metal-ion batteries (*e.g.*, $Li^+/Na^+/K^+$ batteries) and lithium–sulfur batteries (Li–S), with the focus on the discussion of the contributions of mesoporous structures to the electrochemical performance of these batteries.

4.1.1 Alkali metal-ion batteries. Rechargeable alkali metal-ion ($Li^+/Na^+/K^+$) batteries have gained widespread attention since their inception, in view of numerous advantages such as high discharge voltage, small size, and light weight.[335]

4.1.1.1 Lithium-ion batteries (LIBs). LIBs are currently the most popular alkali metal-ion batteries owing to their ease of manufacturing and widespread applications. Typical LIBs are operated by exchanging Li ions between the graphite anode and a lithium-intercalated compound cathode (*e.g.*, $LiMO_2$, M = Co, Ni, Mn).[269,274] The faster transport of Li^+ between/inside the electrodes (both anode and cathode) during the charge/discharge process can make it easier to achieve a high power density. In LIBs, the characteristic time (τ_{eq}) for the diffusion of lithium ions through an electrode material is determined by the square of the characteristic diffusion length (l) and diffusion coefficient (D) according to eqn (1):[336]

$$\tau_{eq} = \frac{l^2}{D} \quad (1)$$

To decrease the diffusion time, one can either increase the diffusion coefficient (*e.g.*, by utilizing better Li^+ conductor) or decrease the diffusion length (by employing nanosized electrode). The latter approach avoids changes in the battery chemistry and has a larger impact on the diffusion time because of the square relationship and has therefore attracted the attention of many researchers in recent years. One of the most effective approaches for achieving nanosized active materials is the utilization of porous electrodes. Although microporous materials with high surface areas are desirable as LIB electrodes, the high surface area also provides defects on the surface, which can increase the reactivity with the electrolyte, thus resulting in undesired side reactions, such as a solid electrolyte interface (SEI) reaction.[2] Furthermore, the ionic motion in such small pores can be very slow, which would seriously limit the power density of LIBs.[337] Mesoporous materials with suitable surface areas and pore sizes are an ideal alternative. The interconnected pores in mesoporous electrodes can facilitate improved electrolyte and Li-ion transport, while the mesoporous structure can accommodate the strain relaxation during the charge/discharge process.[274,338]

Due to the unique crystal structures of intercalated lithium compounds and multiple cations or anions, mesoporous cathodes are hard to achieve with most of them being metal oxides or metal oxide-containing materials.[2] For example, $LiFePO_4$ (LFP) has been widely commercialized as a cathode material for LIBs due to its superior cyclability and inherent safety.[339] However, the low electrical conductivity of $LiFeO_4$ (around 10^{-11} S cm^{-1} compared with 10^{-3} S cm^{-1} for $LiCoO_2$ and 10^{-5} S cm^{-1} for $LiMn_2O_4$) has impeded its capacitive performance.[340] Embedding LFP particles in porous conductive carbons has proven to be an effective way for enhancing the conductivity and improving the electrochemical performance of LFP-based cathodes.[340] Owing to their large pore size, high surface area, and good conductivity, mesoporous carbons are desirable loading carriers for large-sized active materials with sizes of over 2 nm and high theoretical capacity for LIBs, such as metal or metal oxide NPs.[40,143] Recently, P123-templated ordered mesoporous carbon (CMK-8) was successfully used as the host to distribute LFP NPs to produce hybrid

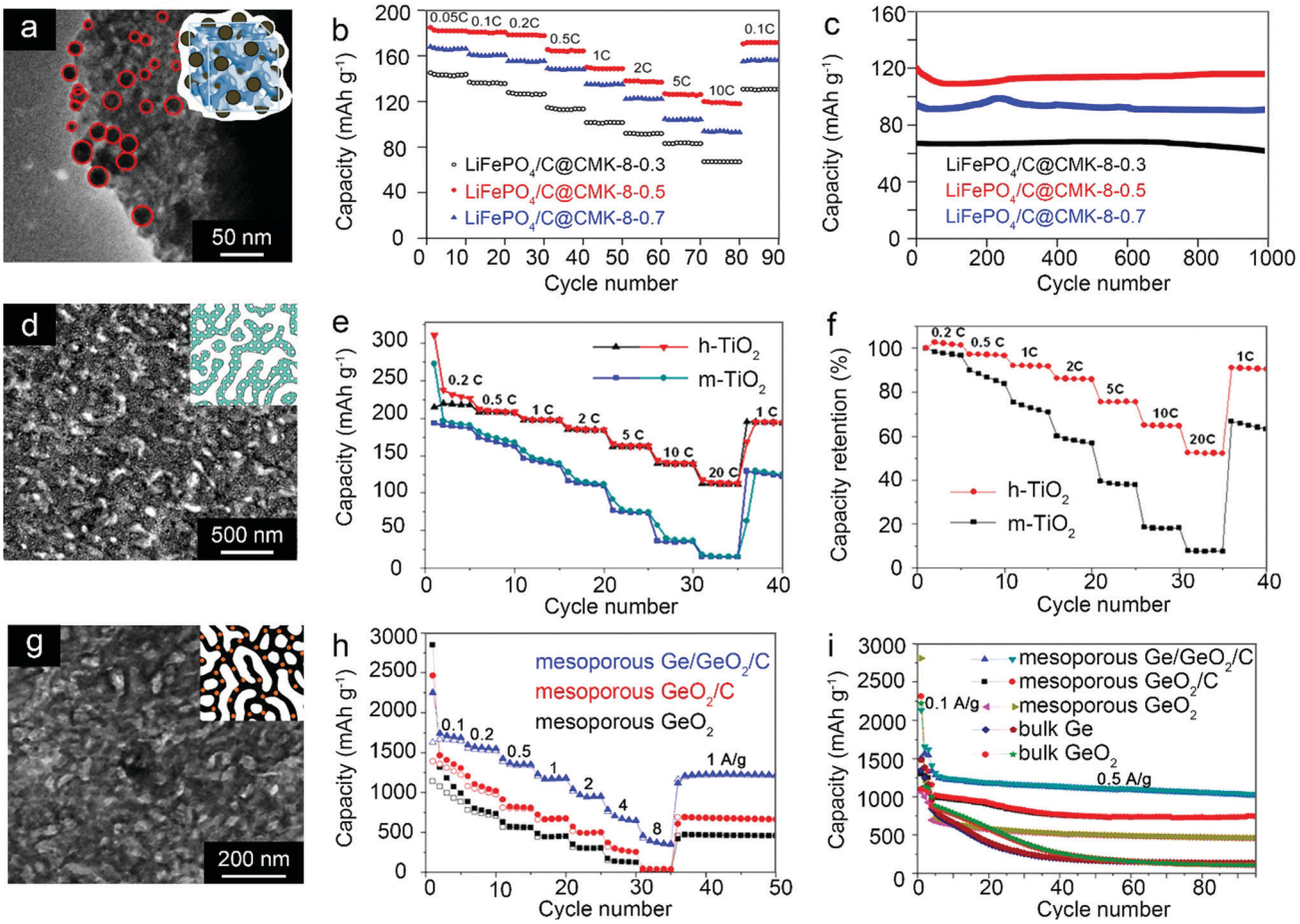

Fig. 27 Mesoporous cathode and anode materials with different pore structures for LIBs. (a) TEM image of $LiFePO_4$/C@CMK-8 hybrids with 50 wt% LFP NPs. (b) Rate capability and (c) long-term cycling performance of $LiFePO_4$/C@CMK-8-*X* (*X* refers to the content of LFP NPs, *X* = 0.3, 0.5, 0.7). (a–c) Reproduced with permission.[341] Copyright 2019, American Chemical Society. (d) TEM image of hierarchically porous titanium dioxide. (e) Charge–discharge capacity values and (f) capacity retention plots of h-TiO_2 and m-TiO_2 as anodes in lithium ion batteries at current densities between 0.2 and 20 C (1 C = 167.5 mA g^{-1}). (d–f) Reproduced with permission.[347] Copyright 2014, American Chemical Society. (g) TEM image of mesoporous Ge/GeO_2/C hybrids. (h) Rate capability and (i) cycling performance of mesoporous GeO_2, mesoporous GeO_2/C, and mesoporous Ge/GeO_2/C electrodes. (g–i) Reproduced with permission.[135] Copyright 2015, American Chemical Society.

porous cathodes for LIBs (Fig. 27a).[341] The resulting hybrid with an LFP content of 50% delivered a large capacity of 178.3 mA h g^{-1} at a current rate of 0.2 C (higher than the theoretical capacity of $LiFePO_4$), and long cycling stability with high capacity retention of 96.7% after 1000 cycles even at a large current density of 10 C (Fig. 27b and c). The excellent performance of this hybrid originated from the 3D cubic bicontinuous mesoporous architecture of CMK-8, which afforded a conductive skeleton for the well-distributed LFP NPs and large pores to store electrolyte, thus facilitating the rapid movement of Li ions.[341]

For LIBs, graphite is still the most frequently used anode material because of its low cost, good electrical conductivity, and high chemical stability. However, the low capacity of graphite (372 mA h g^{-1}) hinders the development of high energy density LIBs.[269] Mesoporous carbons are one of the most promising candidates to replace graphite as the mesoporous structure can enhance the transport of Li ions by shortening the diffusion length and providing large surface area.[342] For example, Zhao *et al.* synthesized mesoporous carbon with spherical mesopores (~9 nm) and high SSA (281 m^2 g^{-1}).[264] The large pore volume (~0.97 cm^3 g^{-1}) provides abundant mesopores to capture extra Li ions, thus leading to remarkable electrochemical properties as an anode material for LIBs, with high reversible capacities of 770 mA h g^{-1} at 100 mA g^{-1} and 255 mA h g^{-1} at 5 A g^{-1} (13.4 C).[264]

Kao *et al.* studied the effect of pore structure of two kinds of mesoporous carbons, CMK-3 with a 2D cylindrical pore structure and CMK-8 with a 3D bicontinuous architecture, on the Li-ion battery performance.[343] Although these two carbon materials have comparable SSAs (1168 m^2 g^{-1} for CMK-3 and 1131 m^2 g^{-1} for CMK-8), CMK-8 displayed larger pore volume (1.36 cm^3 g^{-1}) and smaller charge transfer resistance (~150 Ω) than CMK-3 (1.11 cm^3 g^{-1} and *ca.* 200 Ω, respectively). This finding demonstrates that the bicontinuous mesostructure of CMK-8 enabled faster mass transport and charge transfer than CMK-3, thus affording CMK-8 with better electrochemical performance with a reversible capacity of 569 mA h g^{-1} after 100 cycles at 100 mA g^{-1}, about 37.4% higher than that of the CMK-3 electrode.[343]

To pursue high energy density LIBs, porous metal oxides, such as titania, iron oxides, cobalt oxides, and nickel oxides, *etc.*, have been prepared as anode materials in view of their high theoretical capacities.[344] Among them, Ti-based oxides are of great interest because of their relatively high lithium insertion/extraction operation voltage (1.5–1.8 V *vs.* Li/Li^+), which alleviates the formation of solid electrolyte interface (SEI) layers and ensures the structural stability and safety of LIBs. Moreover, mesoporous Ti-based oxides (*e.g.*, TiO_2) are relatively easy to obtain by BCP-templated synthesis.[13,123,199,345,346]

Steiner *et al.* previously synthesized mesoporous TiO_2 microspheres (MTMs) with tunable pore size by using BCPs of different molecular weights.[123] The Pluronic P123 copolymer resulted in MTMs with relatively small mesopores (~3 nm, MTMs-S). The PS-*b*-PEO copolymers with larger molecular weights produced MTMs with medium-sized (~7 nm, MTMs-M) and large pores (~11 nm, MTMs-L). The battery test showed that MTMs exhibited improved rate performance and capacity retention compared to TiO_2 NPs. MTMs-M and MTMs-L displayed relatively higher rate performance at 10 C than MTMs-S because the larger pore space was more beneficial for achieving a faster transport of Li ions.[123]

Hierarchical porous structures combine the advantages of micropores (offer high specific area) and mesopores (provide large space for mass transport). Lee *et al.* developed combined meso-/macro-phase separation for the synthesis of hierarchically porous TiO_2 with continuous macropores (<100 nm) and mesopores (14.9 nm) as well as a large SSA of 116 $m^2 g^{-1}$ (Fig. 27d).[347] Compared with mesoporous TiO_2 (m-TiO_2) with only mesopores (16.9 nm) and a similar SSA (117 $m^2 g^{-1}$), the highly interconnected macropores in hierarchically porous TiO_2 provided enhanced wettability and facilitated mass transport of electrolyte ions, leading to a larger reversible capacity (113 mA h g^{-1} at 20 C) than that of m-TiO_2 (15 mA h g^{-1} at 20 C) (Fig. 27e). Meanwhile, the hierarchically porous TiO_2 also exhibited higher rate performance with a capacitance retention of 52.6% at 20 C, after the capacity values were normalized by their first discharge capacities, whereas m-TiO_2 retained only 8% (Fig. 27f).[347]

Based on the above reports, it is clear that both porous carbons and metal oxides can be utilized as anode materials for LIBs. However, their drawbacks are also obvious; for example, mesoporous carbons are limited by their low capacity, while metal oxides suffer from low conductivity and serious aggregation during the charge/discharge process. Fortunately, the combination of mesoporous carbons with metal oxides or other compounds with high theoretical capacities to make carbon-based nanocomposite anodes provides an ideal way to overcome these barriers.[135,143,278,348–350] These composite anode materials combine the good conductivity and large pore volume of porous carbon with the high capacity and rate capability of the supported materials.

Recently, Park *et al.* utilized N-doped ordered mesoporous carbon (N-CMK3) as a host to load SnO_2 NPs and obtained the SnO_2@N-CMK3 hybrid anode.[350] The composite exhibited a high SSA of 347 $m^2 g^{-1}$ with an average pore size of 3 nm and the size of the embedded SnO_2 particles was ~3.7 nm. The resulting SnO_2@N-CMK3 exhibited a high reversible capacity of 736 mA h g^{-1}, approaching the theoretical capacity of SnO_2 (782 mA h g^{-1}). Benefiting from the high SSA of the porous N-CMK3, the transport of Li ions across the interface was accelerated, leading to a high reversible capacity of 435 mA h g^{-1} at a high rate of 5 C, which was superior to the theoretical capacity of commercial graphite.

It has also been found that the introduction of a certain amount of metals into metal oxide/carbon hybrids can further improve their battery performance. For instance, Lee *et al.* synthesized mesoporous Ge/GeO_2/carbon composites with an average pore diameter of 44 nm (Fig. 27g).[135] By combining carbon and additional Ge metal NPs with GeO_2, the resultant Ge/GeO_2/carbon hybrid displayed enhanced Coulombic efficiency, high reversible capacity (1631 mA h g^{-1}), as well as high areal capacity (1.65 mA h cm^{-2}) and stable cycling life (Fig. 27h and i). This excellent performance originated from the synergetic effect of the mesoporous structure and the catalytic function of Ge. Specifically, the mesostructure provided uniformly distributed pores that could buffer mechanical strain and large surface area that offered high electrode–electrolyte contact area, while the metallic Ge particles served as an electrocatalyst for Li_2O decomposition and provided an electrically conductive network between the Ge metal and Li_2O for the reoxidation reaction ($Ge + 4.4Li = Li_{4.4}Ge$), thus increasing the overall capacity and Coulombic efficiency.[135]

While LIBs have been well commercialized and greatly improved people's life, the limited reserve (0.0017% in the Earth's crust), high cost (2300 \$\$ ton^{-1}), and uneven distribution of lithium resources have raised significant concerns about the long-term prospects of LIBs.[351] Therefore, researchers have been seeking other inexpensive alkali metals to replace lithium, based on analogous electrochemical storage mechanisms.[352] This began with the development of sodium-ion batteries (SIBs) and potassium-ion batteries (PIBs), which have much more natural storage (2.8% and 2.6% for Na and K, respectively) and much lower cost (200 and 1000 \$ ton^{-1} for Na and K, respectively).[351]

4.1.1.2 Sodium-ion batteries (SIBs). Compared to LIBs, SIBs exhibit an analogous mechanism during the charge/discharge operation, which involves the exchange of Na^+ ions between the layered anode and a sodium intercalation compound cathode.[353] However, the larger ionic radius (0.102 nm for Na^+ *vs.* 0.076 nm for Li^+) and the higher molar mass (23 g mol^{-1} for Na *vs.* 7 g mol^{-1} for Li) of Na bring about various problems and challenges in SIBs, including slow ion diffusion kinetics, high structural stress, and difficult coordination in the host lattice.[351] One of the ideal solutions is to utilize mesoporous electrodes, which can provide large pore volume to host as many as sodium ions, offer open tunnels for fast insertion/extraction of the larger sodium ions and accommodate the volume changes, thus improving the battery performance compared to other batteries utilizing microporous electrodes.[199,292,304,354]

For instance, Zhao *et al.* demonstrated the synthesis of single-layered mesoporous TiO_2 nanosheets with spherical pores along with length and width of around 500 nm, and thickness of about 5.5 nm.[199] These nanosheets possess high

SSAs (154–210 $m^2 g^{-1}$), large pore volumes (0.29–0.35 $cm^3 g^{-1}$), uniform mesopore channels (3.8–4.1 nm) and well-crystalline anatase mesopore walls. The abundant mesopores and high accessible SSAs make the TiO_2 nanosheets highly permeable for electrode–electrolyte contact externally and internally, thereby leading to rapid electrochemical reactions and providing high reversible sodium ion storage. In addition, the highly crystalline mesoporous anatase framework can effectively accommodate the volume changes during sodium insertion/extraction. Therefore, the SIBs made of these mesoporous TiO_2 nanosheets displayed high discharge specific capacity of 220 mA h g^{-1} at 100 mA g^{-1}, outstanding rate capability (stable reversible capacities from 0.1 to 10 A g^{-1}), as well as excellent cycling stability (44 mA h g^{-1} for 10 000 cycles at 10 A g^{-1}).[199] Next, they fabricated a monolayered 2D mesoporous–titania–mesoporous-carbon (C–TiO_2–C) vertical heterostructure with uniform mesopore sizes (4.1 nm for carbon layer and 10.2 nm for TiO_2 layer).[292] This 2D heterostructure exhibited highly reversible pseudocapacitance (96.4% of total charge storage at a sweep rate of 1 mV s^{-1}), and strong mechanical stability during rapid sodiation and desodiation processes.[292] Furthermore, this group also demonstrated the coating of single-layered mesoporous TiO_2 on a variety of nanomaterials, including SiO_2 nanospheres, CNTs, GO, carbon nanospheres, CdS nanowires, ZnS nanosheets, and α-Fe_2O_3 ellipsoids.[304] The ultrathin mesoporous TiO_2 monolayers, in combination with their high SSAs and highly crystalline nature, allowed the accommodation of volume expansion, improved contact with electrolyte, and shortened diffusion length during sodium insertion–extraction, thereby leading to excellent rate capability (the capacity retained at about 90 mA h g^{-1} after 50 000 cycles at 10 A g^{-1}) and superior cyclability for sodium-ion storage (capacity stabilized at around 160 mA h g^{-1} after 500 cycles at 1 A g^{-1}).[304] Apart from metal oxides, mesoporous conducting polymers (*e.g.* polypyrrole and polyaniline) have also been reported as ideal candidates for the accommodation of large Na ions because the redox reaction in conducting polymers usually involves doping/de-doping of electrolyte anions into/from the polymer chains, which is not influenced by the cationic species.[355–358] For example, Mai and colleagues synthesized 2D mesoporous polypyrrole (mPPy) nanosheets with well-defined spherical pores.[293] The resultant mPPy nanosheets exhibited controlled pore sizes in the range of 6.8–13.6 nm, ultrathin thicknesses of 25–30 nm and high SSAs of up to 96 $m^2 g^{-1}$, which enabled the fast transport of large Na ions when used as cathode materials of SIBs. As a result, the mPPy electrode exhibited high reversible discharge capacity of 123 mA h g^{-1} at 50 mA g^{-1}, and good stability with negligible capacity decay even at a high rate of 300 mA g^{-1}, thus demonstrating the advantages of the mesoporous structure.[293]

4.1.1.3 Potassium-ion batteries (PIBs). PIBs also exhibit a typical rocking-chair working mechanism similar to LIBs and SIBs, which involves the shuttle of K^+ between the cathode and the anode. Due to the violent reactivity of the K metal, it is unlikely to be directly used as an anode of PIBs. Thus, great effort has been devoted to the development of K-host materials.[359,360] The main problem is that the K ion has a larger size (0.138 nm) than those of Li (0.076 nm) and Na (0.102) ions, which hinders the intercalation of K^+ ions into the electrode materials and thus leads to low capacity, and poor rate performance and cyclability during the potassiation/depotassiation process.[359,360] To solve this problem, Guo *et al.* synthesized ordered mesoporous carbon (OMC) with a high SSA ($\sim$1089 $m^2 g^{-1}$) and uniform pore size ($\sim$6.5 nm).[361] The large mesopores increased the accessible surface area and offered more space to trap large-sized K ions. As a consequence, when employed as an anode of PIBs, the resultant OMC delivered high specific capacity of 257.4 mA h g^{-1} at a current density of 0.05 A g^{-1} and highly reversible capacity of 146.5 mA h g^{-1} for more than 1000 cycles at 1.0 A g^{-1}, which was superior to those of non-porous or microporous carbon counterparts.[361]

4.1.2 Lithium–sulfur batteries. Lithium–sulfur batteries (Li–S), which usually consist of a sulfur-containing cathode, a lithium metal anode, and a porous separator, adopt an overall electrochemical reaction: $S_8 + 16Li \leftrightarrow 8Li_2S$. Building on this reaction, the anode and cathode of LSBs exhibit high theoretical capacities of 3860 and 1672 mA h g^{-1}, respectively, providing a theoretical energy density of $\sim$2600 W h kg^{-1}, which is much higher than that of LIBs (387 W h kg^{-1}).[362] In addition, the high abundance and low cost of sulfur source make Li–S batteries more competitive than LIBs. Thus, they have been considered as a promising candidate for next-generation batteries. However, there are several barriers hindering the commercial development of Li–S batteries, including the poor conductivity of the sulfur host and lithium sulfide, large volume change of sulfur during the charge/discharge process, and easy loss of dissolved polysulfide intermediates.[362,363] To solve these problems, porous carbons have been widely used as host materials to fabricate carbon–sulfur cathodes due to their facile processability, high SSA, and good electrical conductivity.[315,364–367] Although microporous materials can confine polysulfides in micropores to enhance the cycling stability of Li–S batteries, the lithiation/delithiation reactions of polysulfides confined in the micropores are implemented *via* a solid–solid mechanism, leading to higher resistance than that generated in the solid–liquid–solid process in mesoporous materials.[368] Thus, most of the sulfur cathodes based on microporous structures always show lower voltage plateau ($<$1.0 V)[368] than that of mesoporous cathodes ($>$1.5 V),[369,370] which reduces the total energy density of the cell. Additionally, mesoporous materials with larger pore volumes can accommodate a larger amount of sulfur and achieve faster ion transport compared to microporous materials. Therefore, mesoporous materials have been regarded as prospective cathode materials for Li–S batteries.

A typical example of a carbon–sulfur cathode was achieved by infusing sulfur into ordered mesoporous carbon (OMC) with cylindrical pores, a large pore volume of 2.32 $cm^3 g^{-1}$, and a high SSA of 2445 $m^2 g^{-1}$ (Fig. 28a and b).[364] Interestingly, the resulting sulfur-incorporated OMC possessed a bimodal pore distribution with peaks at 6.0 nm and 3.1 nm. The large pore volume and connected channels of the prepared OMC enabled adequate sulfur loading and facilitated complete redox reactions of the active material, while the small pores with strong adsorption

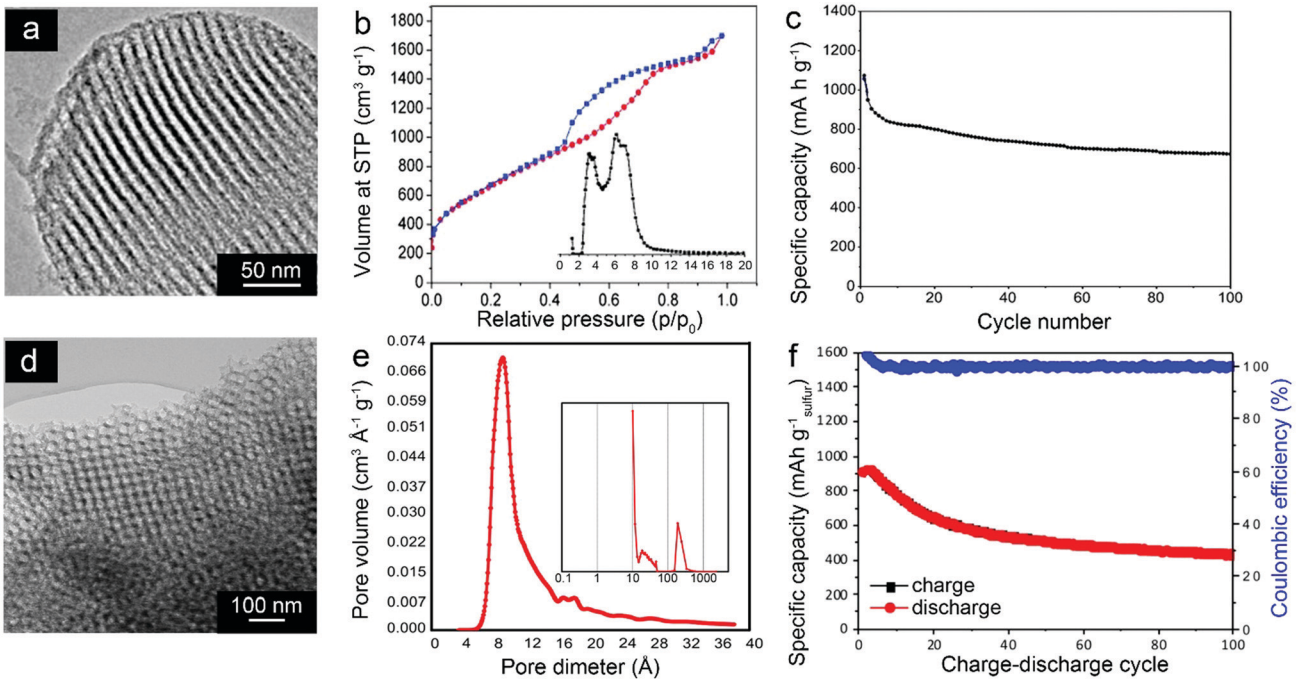

Fig. 28 Mesoporous cathode materials with different pore structures for Li–S batteries. (a) TEM micrograph of spherical OMC NPs showing a 2D-hexagonal structure. (b) Nitrogen sorption isotherm and pore size distribution (inset image) of the spherical OMC NPs. (c) Cycling stability of the C/S electrode with a 70 wt% sulfur content. (a–c) Reproduced with permission.[364] Copyright 2012, Wiley-VCH. (d) TEM image of highly porous gyroid carbon. (e) Micropore and mesopore (inset image) size distribution for the gyroid carbon. (f) Cycling performance of Li–S batteries assembled with the gyroid carbon cathode. (d–f) Reproduced with permission.[372] Copyright 2015, American Chemical Society.

capability for polysulfides could maintain a stable cycling performance.[371] As a result, the synthesized C–S hybrid with a high sulfur content of 70 wt% could achieve a high reversible discharge capacity of 1070 mA h g^{-1} and retained 65.4% of the initial capacitance after more than 100 cycles at 1 C (Fig. 28c).[364]

3D interconnected networks with uniform pores are highly desirable for high-performance Li–S batteries compared to cylindrical pores which typically exhibit only 1D continuity. For example, a bicontinuous double-gyroid carbon material with bimodal pores (1 and 20 nm) and large SSA (885 m^2 g^{-1}) was previously employed as a sulfur host to obtain C–S composite cathode materials for Li–S batteries (Fig. 28d and e).[372] The bimodal porous structure promoted high sulfur loading as well as the trapping of lithium polysulfides in the narrow micropores. Furthermore, the 3D ordered mesopores provided uniform accessibility of sulfur for the diffused Li ions throughout the structure. Therefore, LSBs assembled with such a gyroidal carbon cathode displayed a high discharge capacity of 800 mA h g^{-1} with good cyclability for more than 200 cycles and good rate performance with a high discharge capacity of 400 mA h g^{-1} at 1 C (Fig. 28f).[372]

4.2 Supercapacitors

As an important category of energy storage devices, supercapacitors (SCs) or electrochemical capacitors show some advantages over batteries, including high power density, long cycling life, wide working temperature range, and better safety at high rates.[3,61] Typically, SCs are made of two electrodes, an electrolyte, and a membrane separator, which separates the two electrodes from the electrolyte. Active materials are important part of electrodes in SCs and the general method for the construction of electrodes is casting the slurry consisting of active materials, conductive additives (carbon black) and binders on the current collector (*e.g.*, Ni foam, Al foil or carbon cloth). The specific capacitance of a SC is governed by the equation:[195]

$$C = \varepsilon_0 \varepsilon_r A_e / d \quad (2)$$

where A_e is the surface area of the electrode, d is the distance between the pair of electrodes, ε_0 is the permittivity of free space, ε_r is the relative permittivity of the dielectric material. For SCs, d is not a major variable, thus enlarging A_e is the primary pathway for increasing the capacitance and energy density of SCs. Mesoporous materials are known for their high SSA (*i.e.*, high A_e) and hence they are desirable as electrode materials for SCs.[195,333]

Although microporous materials have large surface areas, many of them show low capacitive performance compared to their mesoporous counterparts.[329–331,337,373,374] This is because of the fact that many inner micropores are closed or exhibit narrow bottle-necks, which are difficult to immerse by the electrolyte, leading to the poor utilization of the surface area.[328,337] The large mesopores of mesoporous materials are favorable achieving fast ion diffusion (especially large-sized ions) at high current densities and efficient utilization of SSAs. Moreover, some studies showed evidence that micropores smaller than 0.5 nm are not accessible to hydrated ions and that even pores under 1 nm might be too small, especially in the case of organic electrolytes,

where the size of the solvated ions is larger than 1 nm.[375] Therefore, most mesoporous materials have higher accessible SSAs and thus show better capacitive performance with higher energy and power densities compared to their microporous counterparts.

In SCs, charge storage and release occur at the interface between the electrode and electrolyte and there are two mechanisms for energy storage and release in SCs.[325] One is the non-Faradaic process in which no chemical redox reaction occurs and only physical charge separation originated from ionic adsorption or desorption takes place. The non-faradaic process is fast and durable. In contrast, the Faradaic process involves redox reactions at the surface of the electrode and electrons are transferred to or from the cathode or anode. This process is slower compared with the non-Faradaic process. Accordingly, SCs can be divided into two classical categories: electrochemical double layer capacitors (EDLCs) that follow the non-Faradaic mechanism, and pseudocapacitors which obey the Faradaic principle.[325]

4.2.1 Electrochemical double-layer capacitors. Porous carbon materials are classical electrodes for EDLCs. Previously, Wu and co-workers fabricated mesoporous carbon materials with highly ordered bcc mesostructures as well as uniform pore diameter of 3.2 nm and high SSAs between 311 and 637 $m^2 g^{-1}$ (Fig. 29a).[329] The cyclic voltammogram of the mesoporous carbon exhibited a rectangular-shaped pattern, which is a typical characteristic of

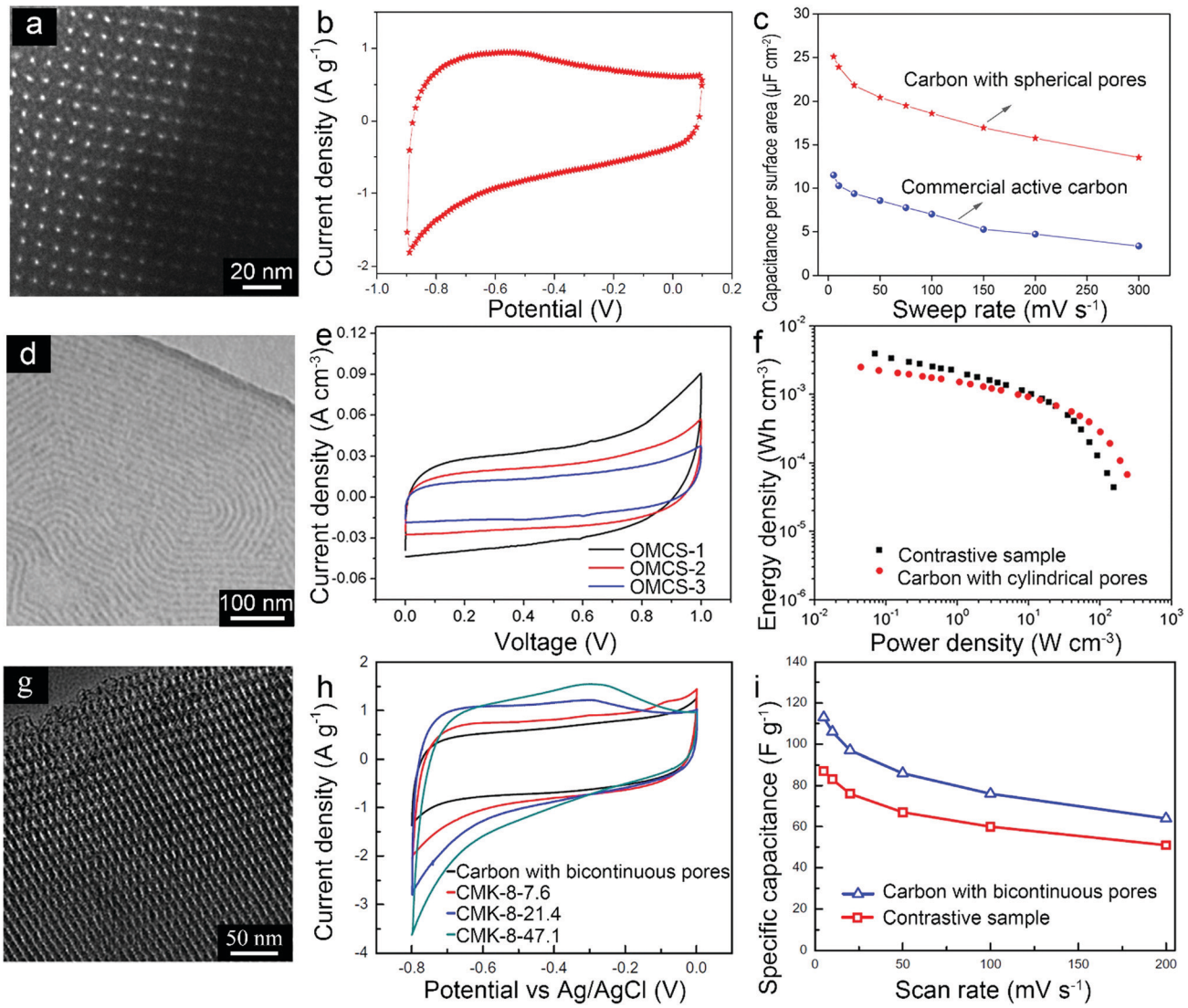

Fig. 29 Mesoporous carbons with different pore structures as electrode materials of EDLCs. (a) TEM image of mesoporous carbon with an ordered bcc mesostructure. (b) CV curve of the carbon sample with spherical pores. (c) Capacitances per surface area of the mesoporous carbon sample and commercial active carbon at various sweep rates. (a–c) Reproduced with permission.[329] Copyright 2013, American Chemical Society. (d) TEM image of well-defined hexagonal mesoporous carbon. (e) CV curves of the samples with cylindrical pores and the contrastive samples obtained at 1000 mV s^{-1}. (f) Ragone plots. (d–f) Reproduced with permission.[376] Copyright 2018, American Chemical Society. (g) TEM image of mesoporous carbon with a bicontinuous structure. (h) CV curves of the mesoporous carbon and the contrastive samples in 1 M Na_2SO_3 at a scan rate of 5 mV s^{-1}. (i) Specific capacitances of the mesoporous carbon and the contrastive samples at different scan rates. (g–i) Reproduced with permission.[377] Copyright 2015, Elsevier.

EDLCs (Fig. 29b). At a sweep rate of 10 mV s^{-1}, the specific capacitance of the OMC was 159 F g^{-1}, higher than that of commercial activated carbon (145 F g^{-1}) (Fig. 29c). The enhanced capacitive performance of the OMC was attributed to its ordered mesoporous structure. Unlike OMC, commercial activated carbon contained a large proportion of internalized disordered micropores. The inner micropores could hardly be accessed by the electrolyte due to the lack of suitable pathways for ion diffusion, leading to poor utilization of the inner pores of the materials.[329] Further, many studies have focused on the influence of pore size on the capacitance of EDLCs.[7,8] The specific capacitance of the OMC was decreased sharply with the increase of average pore diameter from 0.6 to 1 nm but increased linearly when the average pore size was enlarged from 1 to 5 nm and remained constant as the average pore size was enlarged further from 5 to 50 nm. When pores (>2 nm) in electrode materials are larger than twice the dimension of the solvated electrolyte ions, the contribution to capacitance is from the compact layers of ions residing on both adjacent pore walls. Therefore, the capacitance is positively associated with the surface area of porous electrode materials. By decreasing the pore size (1–2 nm) to less than twice the solvated ion size, the compact ion layers from neighboring pore walls became impinged and the surface area usable for the double-layer formation was reduced, which accounted for the decrease of specific capacitance with pore size. However, after decreasing the pore size (<1 nm) to a value approaching the crystallographic diameter of the ion, the solvation shell of ion becomes highly distorted as the ion is squeezed through the pore. Such distortion would allow closer approach of the ion center to the electrode surface, thereby improving the specific capacitance.

Carbon materials with cylindrical pores have also been studied as electrode materials of EDLCs. For instance, highly ordered mesoporous carbon with horizontally aligned (cylindrical) mesopore arrays was used as film-like electrodes in micro-supercapacitors.[376] The mesoporous carbon (Fig. 29d) had average pore size of 10 nm, SSA of 650 m^2 g^{-1}, and pore volume of 0.76 cm^3 g^{-1}. Cyclic voltammetry (CV) curves of the sample displayed nearly rectangular shapes, indicating the efficient EDLC behavior (Fig. 29e). This OMC displayed a specific capacitance of 163 F g^{-1} at a current density of 0.2 A g^{-1} and maintained >90% of the initial capacitance after 20 000 cycles at 1 V s^{-1}. The sample also exhibited good rate capability with a specific capacitance of 94 F g^{-1} at a high current density of 100 A g^{-1}. Compared to OMC with a spherical pore structure, the OMC with cylindrical pores exhibited a higher power density of 242 W cm^{-3} (Fig. 29f), because the parallel-aligned mesopores could provide pathways with lengths of over hundreds of nanometers, which facilitated the rapid movement of charge carriers in the material.[376]

The application of carbon materials with bicontinuous structures as electrode materials for EDLCs has been also documented. For example, previously reported bicontinuous mesoporous carbon with an $Ia\bar{3}d$ symmetry exhibited a uniform pore size of 3.8 nm, pore volume of 1.178 cm^3 g^{-1}, and high SSA of 992 m^2 g^{-1} (Fig. 29g).[377] This bicontinuous mesoporous carbon showed relatively flat, rectangular-shaped CV curves (Fig. 29h), which are typical features of EDLCs. The bicontinuous mesoporous carbon showed a specific capacitance of 113 F g^{-1} at a scan rate of 5 mV s^{-1}, which was higher than that (87 F g^{-1}) of the control sample with cylindrical mesopores (pore size of 3.8 nm and SSA of 554 m^2 g^{-1}) (Fig. 29i). The higher capacitance was primarily contributed by the larger surface area arising from the 3D continuous pore structure. In addition, the bicontinuous structure helped to prevent the mesostructure from collapsing during the charge/discharge process, thus affording the mesoporous carbon outstanding cycling stability.[377]

4.2.2 Pseudocapacitors. Unlike EDLCs, the charge storage mechanism of pseudocapacitors is based on the reversible redox reactions on the surface of the active materials.[195] Pseudocapacitors usually exhibit much higher capacitance than EDLCs. As of now, the developed electrode materials for pseudocapacitors are mainly based on transition metal oxides and hydroxides, metal sulfides, conducting polymers, and so on.[61,378] N-doped carbon materials are among the most commonly studied electrode materials, in which the doping of nitrogen atoms can improve the capacitive performance of carbon materials owing to the enhancement of wettability and the additional supply of pseodocapacitance.[96,379] For example, Mai's group synthesized a library of N-doped mesoporous carbon nanospheres (MCNSs) with different pore sizes using PS-*b*-PEO copolymers as soft templates (Fig. 30a).[9] By changing the length of the PS block, the average pore diameter could be tuned in the range of 8–38 nm, which resulted in controllable SSAs of 229–450 m^2 g^{-1} and pore volumes of 0.50–0.96 cm^3 g^{-1}. The optimized MCNS sample (MCNS-60) showed the highest specific capacitance of 350 F g^{-1} at a current density of 0.1 A g^{-1} in 1 M H_2SO_4, which was much higher than that of undoped carbon nanospheres. MCNS-60 also exhibited good capacitance retention as a high specific capacitance of 200 F g^{-1} could still be retained at a high current density of 2.0 A g^{-1} (Fig. 30b). The lack of apparent capacitance loss after 10 000 cycles at a high current density of 10 A g^{-1} indicated the outstanding cycling stability of the MCNSs (Fig. 30c). In addition, this work systematically studied the influence of large mesopore size (>5 nm) on the capacitive performance of MCNSs and demonstrated that their specific capacitance decreased linearly with increasing pore diameter, while the normalized capacitance by SSA remained nearly unchanged, revealing the relationship between the specific capacitance and average pore size of porous carbons.[9]

Recently, N-doped carbon materials with cylindrical pores were employed as electrode materials for pseudocapacitors (Fig. 30d).[380] The porous carbon had uniform pore diameter of 3.2 nm, large pore volume of 1 cm^3 g^{-1}, and high SSA of 1152 m^2 g^{-1}. It exhibited 43% capacitance retention when the current density was increased from 0.1 to 20 A g^{-1} (Fig. 30e). Such a rapid decrease in capacitance was attributed to the kinetic limitation of Faradaic reactions at high current densities, indicating a pseudocapacitive effect, which is different from EDLCs. Furthermore, the specific capacitance of the material reached 200 F g^{-1} at 1 A g^{-1}, with 98% capacitance retention after 5000 charge–discharge cycles (Fig. 30f).[380]

Bicontinuous structures with highly ordered mesostructures and total continuity in all three dimensions can provide exceptional

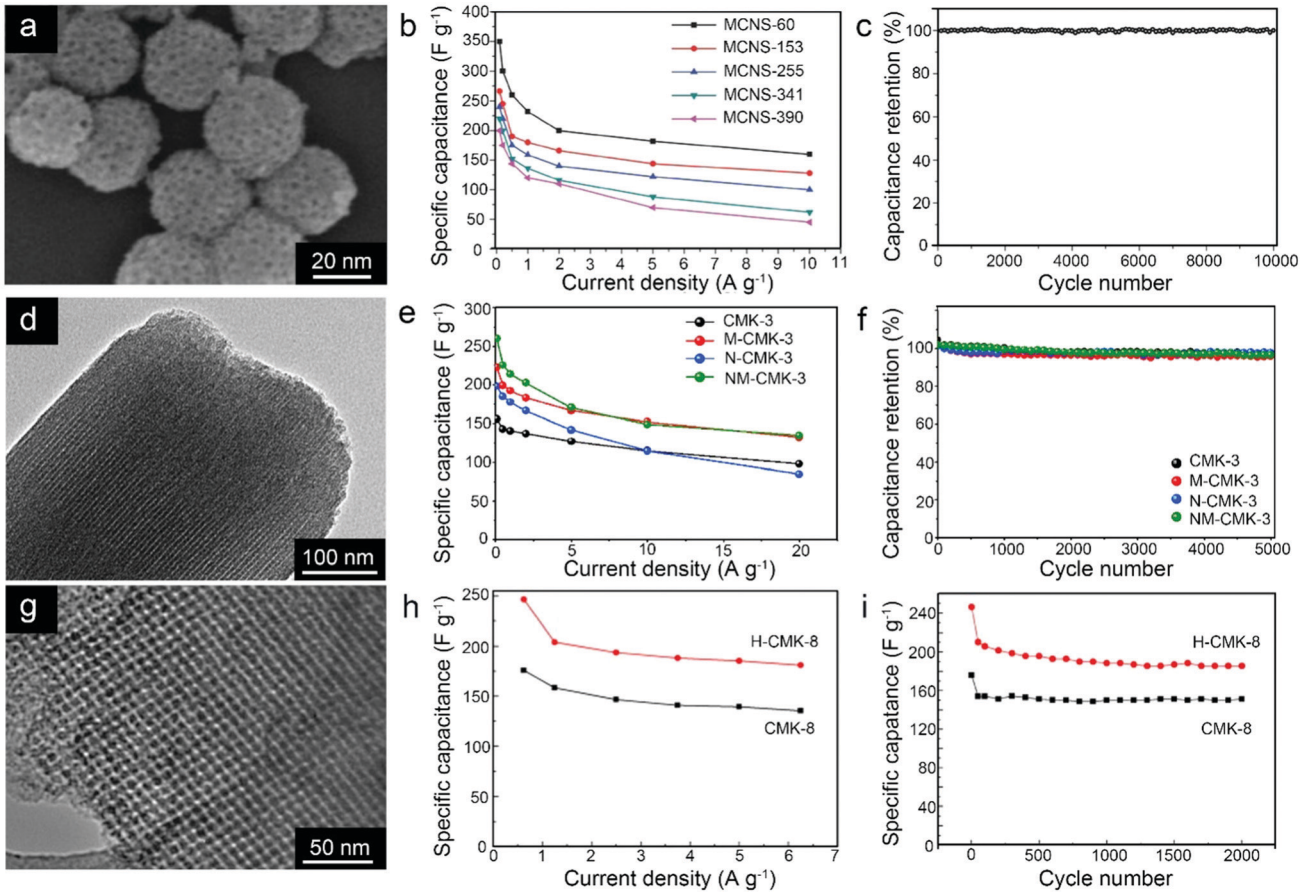

Fig. 30 Mesoporous carbon materials with different pore structures as electrodes of pseudocapacitors. (a) TEM image of nitrogen-doped carbon with spherical pores. (b) Capacitance retention with increasing current density for the various carbon samples with different pores sizes. (c) Cycling stability of MCNS-60 evaluated at a high current density of 10 A g^{-1}. (a–c) Reproduced with permission.[9] Copyright 2016, Wiley-VCH. (d) TEM image of mesoporous carbon with a cylindrical pore structure. (e) Rate performance of N-doped mesoporous carbon (N-CMK-3) with a cylindrical pore structure and the contrastive samples. (f) Cycling stability of N-CMK-3 and the contrastive samples at a current density of 1 A g^{-1}. (d–f) Reproduced with permission.[380] Copyright 2016, Elsevier. (g) TEM image of bicontinuous mesoporous carbon. (h) Specific capacitances of the gyroidal carbon (CMK-8) and acid-modified gyroidal carbon (H-CMK-8) electrodes as a function of discharging current density. (i) Cycling life of the CMK-8 and H-CMK-8 electrodes at a current density of 1.25 A g^{-1}. (g–i) Reproduced with permission.[381] Copyright 2011, Elsevier.

mass transport and minimize blockage of the channels in porous SC electrode materials. For instance, mesoporous carbon with a gyroid structure was previously synthesized (Fig. 30g).[381] After nitric acid treatment, the surface of the mesoporous carbon was functionalized with nitrogen and oxygen-containing groups, which contributed pseudocapacitance to enhance the overall capacitance of the mesoporous carbon. The gyroidal mesoporous carbon had average pore diameter of 4.8 nm, large pore volume of 1.38 cm^3 g^{-1} and high SSA of 1321 m^2 g^{-1}, leading to a high specific capacitance of 239 F g^{-1} at a current density of 2.4 A g^{-1} with good rate capability (74% capacitance retention) at a high current density of 6.25 A g^{-1} (Fig. 30h and i).[381]

Many transition metal oxides show pseudocapacitive behavior and they have been widely utilized as pseudocapacitor electrodes.[382] For instance, Steiner's group reported a vanadium pentoxide (V_2O_5) electrode with a bicontinuous double-gyroid structure, exhibiting 11.0 nm wide struts and high specific surface to volume ratio of 161.4 μm^{-1}.[383] The V_2O_5 electrode displayed a high initial capacitance of 442 F g^{-1} at a high current density of 10 A g^{-1} in 1.0 M $LiClO_4$ propylene carbonate electrolyte, which eventually stabilized at 155 F g^{-1} after 10 charge–discharge cycles. The high capacitance was contributed by the fast and efficient ion intercalation/extraction in the bicontinuous V_2O_5 electrode and the consequent Faradaic surface reactions.

Most recently, Mai and colleagues developed a universal interfacial self-assembly strategy for fabricating 2D nanohybrids with in-plane cylindrical pores.[12] They patterned 2D polymers (*e.g.*, PPy, polyaniline, and polydopamine) with cylindrical mesopores on graphene nanosheets to obtain mesoporous electrodes for planar microsupercapacitors (MSCs). The prepared 2D sandwich-like nanohybrids possessed average mesopore diameter of ~12 nm, uniform thickness of ~26 nm, and high SSA of 157 m^2 g^{-1}. Using mesoporous PPy/rGO (mPPy/rGO) nanosheets as an example, they exhibited cylindrical pores which could offer in-plane pathways in 2D porous materials (Fig. 31a and b). Therefore, the mPPy/rGO nanosheets exhibited a higher ion diffusion coefficient (6.8×10^{-8} cm^2 s^{-1}) than PPy/rGO nanosheets with spherical pores or without pores. The interdigitated

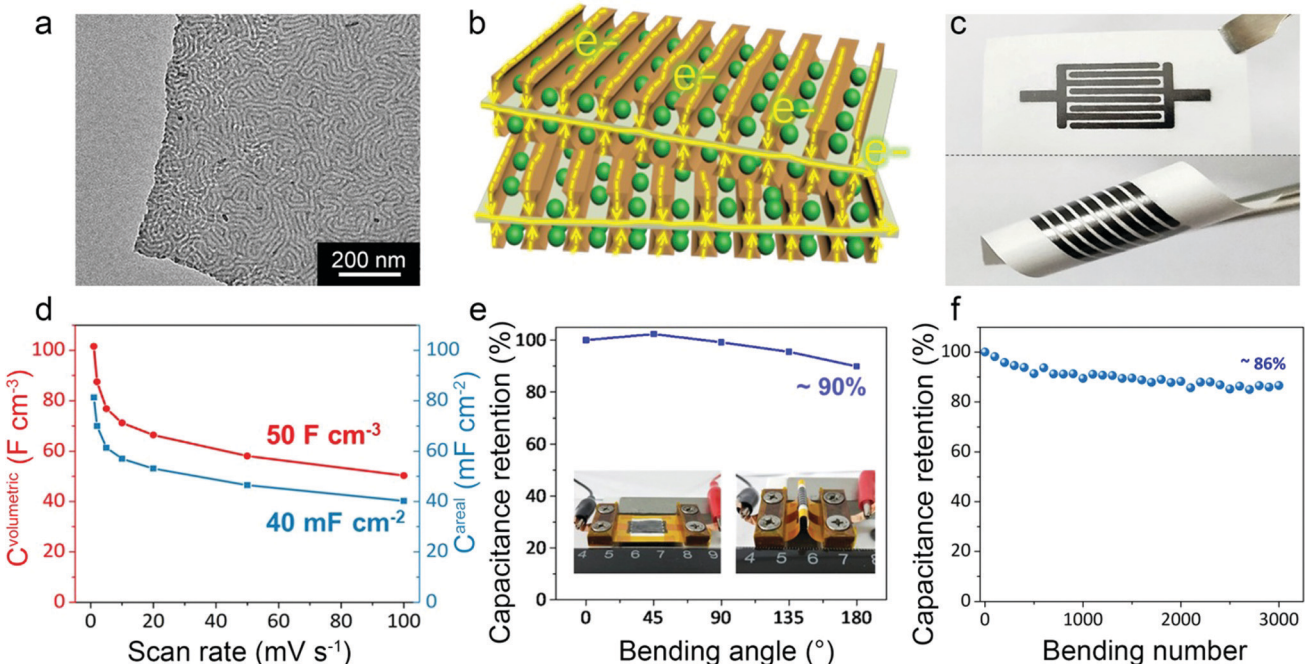

Fig. 31 Sandwich-structured mPPy/rGO nanosheets with in-plane cylindrical mesopores and their performance as electrodes of planar microsupercapacitors (MSCs). (a) TEM image of mPPy/rGO nanosheets with in-plane cylindrical pores. (b) A schematic illustration showing the role of the in-plane cylindrical mesopores in enhancing the electrochemical performance of MSCs. (c) Photographs of mPPy/rGO microelectrodes taken at flat (up) and bending (down) states. (d) Areal capacitance (blue) and volumetric capacitance (red) of mPPy/rGO-MSCs as a function of scan rate. (e) Evolution of the capacitance ratio as a function of bending angle. Insets show the digital photographs of the MSCs with bending angles of 0° and 180°. (f) Evolution of the capacitance retention as a function of bending number at bending angles of 0° and 90°. Reproduced with permission.[12] Copyright 2019, Wiley-VCH.

microelectrode, which was assembled from the combination of mPPy/rGO nanosheets and a H_2SO_4/polyvinyl alcohol gel electrolyte *via* mask-assisted filtration,[384] possessed a valid electrode area of 1.12 cm^2 and an average thickness of 7.1 μm (Fig. 31c). Benefiting from the large SSA and fast in-plane ion transport, the electrode delivered outstanding volumetric capacitance (102 F cm^{-3} at 1 mV s^{-1}) (Fig. 31d), high energy density (2.3 mW h cm^{-3}), and power density (500 mW cm^{-3}), outperforming some commercial energy storage devices (2.75 V/44 mF and 5.5 V/100 mF, <1 mW h cm^{-3}).[385–387] Furthermore, the MSC showed excellent flexibility as it could retain 90% of its initial capacitance at a bending angle of 180° (Fig. 31e) and *ca.* 86% of its initial capacitance after continuous bending from 0° to 90° for over 3000 cycles (Fig. 31f).[12]

4.3 Catalysts

Heterogeneous catalysis in the presence of electrocatalysts or photocatalysts has been considered as one of the most important research fields for energy conversion. The intrinsic properties of the catalysts, such as SSA, pore structure, particle size, and geometrical shape, greatly influence their catalytic performance.[194,388] In recent years, BCP-templated mesoporous materials have proven to be promising heterogeneous electrocatalysts or photocatalysts due to their abundant catalytic sites. In this subsection, we discuss the applications of BCP-templated mesoporous materials as photocatalysts and electrocatalysts.

4.3.1 Electrocatalytic oxygen reduction. The oxygen reduction reaction (ORR) is a key process in fuel cells (FCs), which generate electricity by electrochemical reduction of oxygen and oxidation of hydrogen.[389] The ORR process involves an oxygen diffusion cathode and reduction reaction that occurred on the surface of the electrocatalyst. Thus, the rational design of porous materials with high surface area and superior mass transport properties can lead to enhanced ORR performance. Mesoporous materials can provide better mass transport of protons and O_2 molecules to the active sites, which is not easily achieved by microporous materials due to the small openings (1–2 nm).[390,391] Furthermore, in mesoporous materials, the produced H_2O_2 can be released within a relatively short contact time due to the favorable mass transport in the mesoporous structure, thus leading to better selectivity to H_2O_2 in ORR compared to micropore-dominant materials.[330]

Although platinum (Pt)-based materials exhibit high activity for the ORR, the low abundance, high cost, and poor stability of Pt greatly impede the wide application Pt-based electrocatalysts for FCs.[389,392] Therefore, enormous efforts have been devoted to developing alternative non-platinum ORR electrocatalysts for FCs with low cost and high efficiency.[388,393]

One effective way is to fabricate Pt-based electrocatalysts by reducing the usage of Pt while maintaining the catalytic performance, including synthesizing mesoporous Pt catalysts with larger SSAs or fabricating Pt-based alloys by doping other metals.[21,200] For example, Yamauchi's group reported the controllable synthesis of mesoporous Pt nanospheres by using F127 as a pore-creating agent (Fig. 32a).[226] The resulting mesoporous Pt spheres exhibited an average pore diameter of 11 nm,

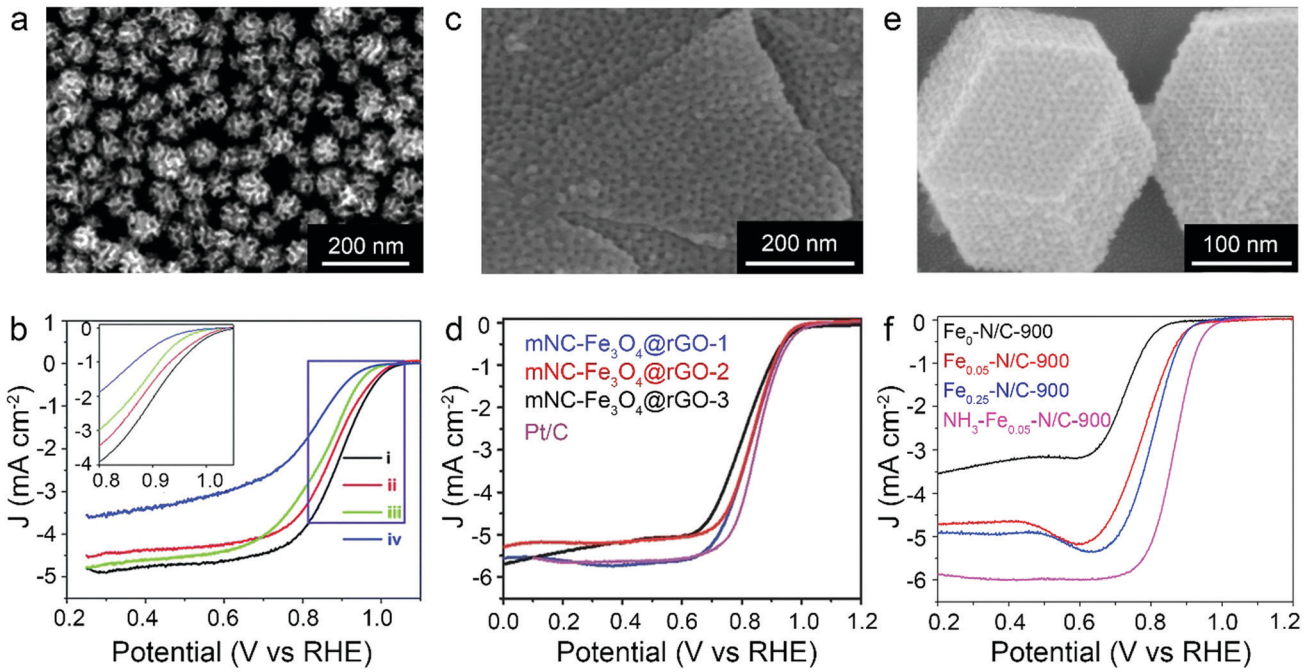

Fig. 32 Mesoporous hybrid materials of different structures for the ORR. (a) SEM image of mesoporous Pt NPs. (b) ORR polarization curves recorded in O_2-saturated 0.1 M $HClO_4$ solution with a sweep rate of 10 mV s^{-1} and a rotation rate of 1600 rpm [(i)–(iv) represents various samples: mesoporous Pt NPs with interconnected mesopores (i), dendritic Pt NPs (ii), PtC-20% catalyst (iii), and PtB catalyst (iv)]. (a and b) Reproduced with permission.[226] Copyright 2016, Royal Society of Chemistry. (c) SEM image of mNC–Fe_3O_4@rGO with a Fe_3O_4 loading content of 7.5 wt%. (d) Line sweep voltammetry (LSV) curves of mNC–Fe_3O_4@rGO-*X* catalysts (*X* stands for the number of samples, *X* = 1, 2, 3 for samples with Fe_3O_4 loading contents of 7.5 wt%, 7.6 wt% and 7.7 wt%, respectively) and commercial Pt/C at a scan rate of 10 mV s^{-1} with a rotation speed of 1600 rpm. (c and d) Reproduced with permission.[11] Copyright 2018, Wiley-VCH. (e) SEM image of the carbonized mesoporous $Fe_{0.25}$–N/C-900; (f) LSV curves of Fe_0–N/C-900, $Fe_{0.05}$–N/C-900, $Fe_{0.25}$–N/C-900 and NH_3–$Fe_{0.25}$–N/C-900. (e and f) Reproduced with permission.[236] Copyright 2017, Elsevier.

leading to a high electrocatalytic activity with a half-wave potential of 0.88 V *versus* reversible hydrogen electrode (RHE, all the reference potentials are *vs.* RHE unless specifically noted), which is more positive than those of Pt/C-20% (0.84 V) and Pt black (0.78 V) (Fig. 32b). As the well-defined mesoporous structure was less vulnerable to particle aggregation, the mesoporous Pt nanospheres showed excellent structural thermostability and retained most of their electrochemically active surface area after thermal treatment, in stark contrast to the low thermal stability of other Pt-based NPs due to the structural shrinkage.[226]

Another possible strategy to reduce the cost of the catalysts is to use non-precious metal catalysts. Carbon-based materials, which combine the advantages of both non-precious-metal containing materials and mesoporous carbons, have proven to be effective ORR electrocatalysts.[40,394] For example, Mai and colleagues prepared 2D sandwich-like mesoporous N-doped carbon/Fe_3O_4/rGO (mNC–Fe_3O_4@rGO) nanohybrids with a uniform pore size of 13 nm (Fig. 32c).[11] Benefiting from the high SSA (373 m^2 g^{-1}) and fast mass transport induced by the introduction of mesopores, the mNC–Fe_3O_4@rGO nanohybrids displayed a high half-wave-potential of 0.84 V and a limiting current density of 5.7 mA cm^{-2}, which are well comparable to those of the best commercial Pt/C catalyst (Fig. 32d).[11] In addition to doping metal oxides, other dopants, such as metal hydrates, metal carbides, non-noble metals or their alloys (*e.g.*, Pd, PdCo alloy), among others, have also been incorporated into mesoporous carbon materials as high performance ORR catalysts.[233,395] Particularly, a family of mesoporous Co-/N-doped or Fe-/N-doped carbon catalysts have been recently developed.[396–399] For example, Yamauchi *et al.* previously synthesized ordered mesoporous Fe-/N-doped carbons (Fe–N/C) possessing spherical pores with an average pore diameter of ~7.7 nm (Fig. 32e).[236] Due to the high content of pyridinic nitrogen (0.96 at%), high SSA (1643 m^2 g^{-1}), and large pore volume (1.54 cm^3 g^{-1}), the obtained Fe–N/C material showed excellent ORR performance with high onset potential of 1.02 V, half-wave potential of 0.87 V, and limited-diffusion current density of 5.98 mA cm^{-2} (Fig. 32f).[236]

Alternatively, by doping a single heteroatom (*e.g.*, N, P, S) or multiple heteroatoms into mesoporous carbon, improved ORR performance can be efficiently achieved since the heteroatom dopants can change the chemisorption of reactants and tune the chemical activity of the electrocatalyst.[400–402] Among various heteroatom-doped electrocatalysts, N-doped carbons have been extensively studied in recent years since the first report by Dai and co-workers on the synthesis of N-doped carbon nanotubes as potential electrocatalysts for the ORR.[403] Yamauchi's group previously reported the synthesis of N-doped mesoporous carbon spheres (NMCSs) with nitrogen content ranging between 7.3–7.7 wt% (Fig. 33a).[220] By increasing the PS block length of PS-*b*-PEO copolymers, the pore diameter of the NMCSs could be expanded from 5 to 16 nm, while the SSA was decreased from

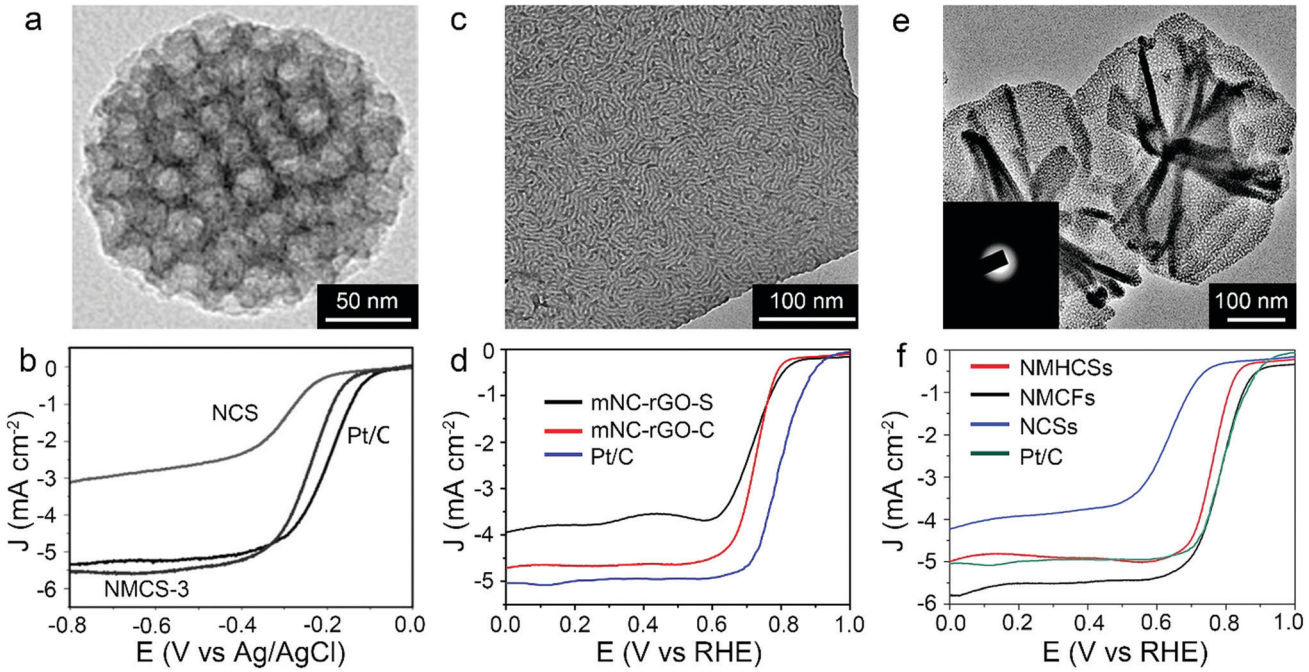

Fig. 33 Mesoporous metal-free materials of different structures for the ORR. (a) TEM image of N-doped mesoporous carbon spheres (NMCS). (b) Polarization curves of N-doped carbon spheres (NCS), NMCS, and Pt/C catalyst in O_2-saturated 0.1 M KOH solutions with a scan rate of 10 mV s^{-1} and a rotating rate of 1600 rpm. (a and b) Reproduced with permission.[220] Copyright 2015, Wiley-VCH. (c) TEM images of mNC–rGO–C. (d) RDE plots of mNC–rGO–C, mNC–rGO–S, and commercial Pt/C catalyst at a scan rate of 10 mV s^{-1} and a rotation rate of 1600 rpm. (c and d) Reproduced with permission.[404] (e) TEM image of NMCFs; the inset shows the SEAD pattern. (f) RDE plots of NMCSs, NMCFs, NCSs and a commercial Pt/C catalyst at a scan rate of 10 mV s^{-1} and a rotation rate of 1600 rpm. (e and f) Reproduced with permission.[291] Copyright 2018, Royal Society of Chemistry.

363 to 343 m^2 g^{-1}. The large mesopores and small dimensions (~200 nm) of the NMCSs contributed to the mass transport by reducing and smoothing the diffusion pathways, leading to high ORR electrocatalytic activity with onset potential of −0.11 V (*vs.* Ag/AgCl) and maximum current density of 6.2 mA cm^{-2} at a rotation rate of 1600 rpm in 0.1 M KOH (Fig. 33b).[220]

To investigate the effect of the pore structure of N-doped carbon on the ORR performance, Mai and co-workers coated mesoporous N-doped carbon layers with spherical or cylindrical pores on graphene nanosheets (denoted as mNC–rGO–S and mNC–rGO–C, respectively) (Fig. 33c).[404] The resulting 2D porous nanocomposites possessed similar N doping contents of ~2.6 wt%, average pore sizes of ~8 nm, and SSAs of ~420 m^2 g^{-1}. They demonstrated that the ion diffusion coefficient of the N-doped carbon nanosheets with cylindrical pores was approximately four times higher than that of their counterpart with spherical pores. Therefore, the former exhibited superior ORR catalytic performance in 0.1 M KOH, with half-wave-potential of +0.74 V and limiting current density of 4.8 mA cm^{-2} (Fig. 33d), comparable with those of commercial Pt/C catalyst.[404]

Furthermore, this group also synthesized N-doped mesoporous carbon nanosheets (NMCSs) and nanoflowers (NMCFs) with holey mesopores to study the influence of the packing mode of carbon nanosheets on their ORR performance (Fig. 33e).[291] The resulting NMCSs and NMCFs possessed similar holey pores (14 nm and 15 nm), SSAs (256 m^2 g^{-1} and 266 m^2 g^{-1}) and nitrogen contents (4.2 wt% and 4.4 wt%). The presence of holey pores enabled more efficient utilization of the active sites buried in the packing space of NMHCSs, thus leading to more positive half-wave potential ($E_{1/2}$ = 0.77 V) and higher limiting current density (J_L = 5.0 mA cm^{-2}) in 0.1 M KOH, outperforming those of N-doped carbon sheets lacking holey pores ($E_{1/2}$ = 0.67 V, J_L = 4.0 mA cm^{-2}) (Fig. 33f). Nevertheless, the holey pores would inevitably be partially blocked after the random stacking of porous carbon nanosheets. This problem can be avoided by the 3D packing pattern of holey porous carbon nanosheets in NMCFs, which enabled the direct cross-plane mass diffusion so that significantly more active sites could be accessible to oxygen and electrolyte, leading to better ORR performance of NMCFs ($E_{1/2}$ = 0.8 V and J_L = 5.5 mA cm^{-2}). This study unveiled the influence of the packing mode of 2D porous carbon nanomaterials on their ORR performance, which would be helpful for designing novel porous materials as high-performance ORR catalysts.[291]

4.3.2 Electrocatalysts for water splitting

4.3.2.1 Electrocatalytic hydrogen evolution. As one of the most renewable and clean energy carriers, hydrogen has been perceived as an ideal long-term solution to both energy crisis and environmental problems.[388,405,406] However, the traditional strategies to mass produce hydrogen, including steam reforming of fossil fuels, such as natural gas, petroleum, and coal, generate significant carbon emission and require high energy consumption. Since the coining of the term "hydrogen economy" by General Motors engineers in 1970, numerous studies have been performed with the major focus on developing advanced techniques to produce

hydrogen economically from clean and sustainable resources. Among various technologies, electrocatalytic water splitting represents one of the most promising solutions for producing hydrogen without environmental pollution.[405]

Although platinum-based materials are known as the state-of-the-art electrocatalysts for HER, their high cost and scarcity prevent their scale-up applications.[388] Recently, molybdenum-based materials (*e.g.*, molybdenum-based oxides,[407] carbides,[408] sulfides,[409] and phosphates[410]) have been considered as one of the potential substitutes for Pt-based catalysts because of their low cost, optimal hydrogen adsorption energy, and electronic density of states resembling those of Pt-based materials.[405] However, the poor conductivity and strong aggregation of Mo-based NPs typically lead to large impedance and reduction of active sites, which lower the HER performance. To solve these problems, making porous catalysts with high conductivity or combining NPs with porous conductive substrates can be effective because the introduction of the porous structure can increase the SSA of materials to expose more active sites and afford space to reserve electrolytes.[2]

Recently, Mai's group fabricated 2D sandwich-like mesoporous N-doped carbon/Mo_2C/rGO nanohybrids with well-defined spherical pores (denoted as mNC–Mo_2C@rGO) (Fig. 34a).[294] The mNC–Mo_2C@rGO nanosheets possessed high nitrogen contents (4.2–5.2 at%), suitable pore sizes (*ca.* 13 nm in diameter), large SSAs (389 m^2 g^{-1}) as well as good distribution of small Mo_2C NPs (4 nm average diameter). The content of the Mo_2C NPs is tunable by adjusting the feed amount of $Mo_7O_{24}^{6-}$, which was estimated to be 18.4 wt% for mNC–Mo_2C@rGO-1, 28.0 wt% for mNC–Mo_2C@rGO-2 and 42.4 wt% for mNC–Mo_2C@rGO-3, respectively. The unique structure and suitable loading content of Mo_2C NPs afforded the nanohybrid with excellent HER catalytic activity which was comparable to that of commercial Pt/C catalyst in 1.0 M KOH electrolyte, with small overpotential of 95 mV at 10 mA cm^{-2}, Tafel slope of 49.8 mV dec^{-1}, and excellent stability at 20 mA cm^{-2} for 60 hours (Fig. 34b and c).[294]

In another example, Suib *et al.* prepared mesoporous molybdenum oxide ($mMoO_{3-x}$) with large accessible pores (20–40 nm in diameter).[411] The resultant $mMoO_{3-x}$ had a much larger SSA (52 m^2 g^{-1}) than the commercial MoO_3 (2.0 m^2 g^{-1}), thus allowing for the exposure of more active sites to facilitate hydrogen production in alkaline solution. Benefiting from the mesoporous structure, the $mMoO_{3-x}$ only required a low overpotential (~0.14 V) to achieve a current density of 10 mA cm^{-2} in 0.1 M KOH, with a low Tafel slope of 56 mV dec^{-1} (comparable to that of Pt/C catalyst) and good stability for more than 12 hours at a large current density.[411]

4.3.2.2 Electrocatalytic oxygen evolution. The oxygen evolution reaction (OER), another half reaction of electrocatalytic water splitting, typically involves a multi-electron reaction pathway ($4OH^- \rightarrow O_2 + 4e^- + 2H_2O$ in alkaline media or $2H_2O \rightarrow 4H^+ + O_2 + 4e^-$ in acidic media), making the need for highly efficient electrocatalysts more urgent than that for hydrogen evolution

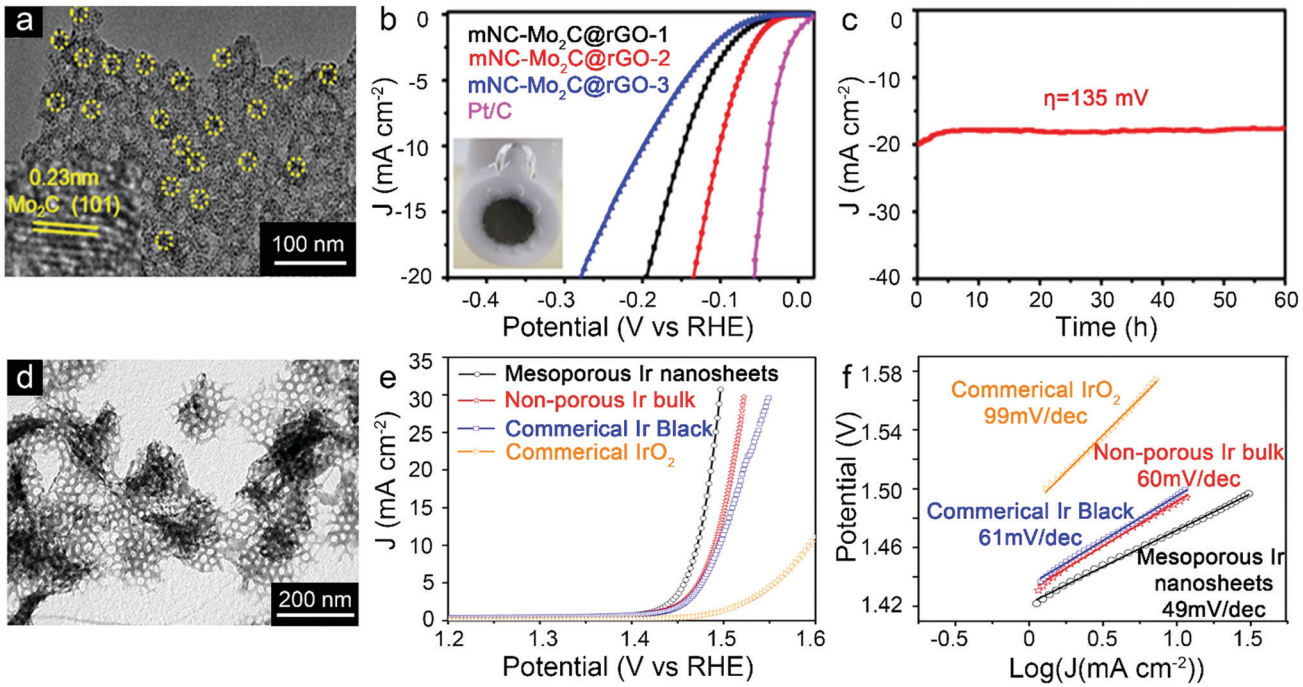

Fig. 34 Mesoporous materials for electrocatalytic water splitting. (a) TEM micrograph of mNC–Mo_2C@rGO-1; the inset shows a high resolution TEM image of the Mo_2C particles. (b) Polarization curves of the mNC–Mo_2C@rGO and Pt/C catalysts measured at a scan rate of 5 mV s^{-1} in 1.0 M KOH. (c) Long-term durability of mNC–Mo_2C@rGO-2 at a constant overpotential of 135 mV for 60 hours. (a–c) Reproduced with permission.[294] Copyright 2018, American Chemical Society. (d) TEM image of mesoporous Ir nanosheets; (e) polarization curves and (f) Tafel plots of mesoporous Ir nanosheets, non-porous bulk Ir, and commercial Ir black and IrO_2 catalysts examined in 0.5 M H_2SO_4 at a scan rate of 5 mV s^{-1}. (d–f) Reproduced with permission.[198] Copyright 2018, American Chemical Society.

reaction (HER).[388,412] To date, various catalysts, such as iron (Fe), cobalt (Co), nickel (Ni), their alloys (Ni–Co, Ni–Fe, Ni–Mo), oxides, nitrides and carbides, have been utilized as electrocatalysts for OER.[412] Although these non-precious metal-based catalysts possess several advantages over the benchmark IrO_2 or RuO_2 catalysts in terms of price and abundance, they still underperform in terms of both activity and stability.

The utilization of a porous IrO_2 or RuO_2 catalyst for the OER can lower the cost of the catalyst by reducing the usage of these expensive materials, while enhancing the catalytic efficiency by increasing the SSA.[413] For instance, Kraehnert *et al.* synthesized mesoporous IrO_2 film with spherical pores with an average pore diameter of ~16 nm and a high SSA of 140 $m^2\ g^{-1}$.[127] Compared with non-porous IrO_2 film, the optimized mesoporous IrO_2 film exhibited improved catalytic performance for OER with low overpotentials of about 0.21 V at 0.5 mA cm^{-2} and 1.58 V at 100 mA cm^{-2}.[127]

Furthermore, ultrathin Ir-based or Ru-based nanosheets with mesopores can improve the catalytic performance by increasing the SSA and improving accessibility to active sites. To this end, Yamauchi's group synthesized mesoporous Ir nanosheets with average diameter of 15 nm and SSA of 42 $m^2\ g^{-1}$ as an electrocatalyst for OER (Fig. 34d).[198] The mesoporous Ir nanosheets with abundant catalytically active sites exhibited excellent activity for OER with small onset potential of 1.41 V, low Tafel slope (49 mV dec^{-1}), and very low overpotential (1.5 V) at 10 mA cm^{-2}, superior to those of commercial Ir black and IrO_2 (Fig. 34e and f).[198]

4.3.3 Photocatalysts for water splitting

4.3.3.1 Photocatalytic hydrogen evolution. Photocatalytic water splitting is another promising strategy achieving the scalable and efficient production of hydrogen.[414,415] In 1972, Fujishima and Honda discovered that TiO_2 could function as a photoanode under ultraviolet (UV) irradiation to decompose H_2O into H_2 and O_2, thus opening a whole new area of photoelectrochemical water splitting.[416] Since then, TiO_2 has been regarded as a promising photocatalyst for water splitting.[417,418] Although various TiO_2-based photocatalysts for water splitting have been developed in the past few decades, they still suffer from the drawbacks of fast recombination of photogenerated electron–hole pairs and undesirable crystallites and architectures.[419,420] Fortunately, these drawbacks can be overcome by constructing ordered mesoporous structures.

For instance, Zhao and colleagues reported the synthesis of ordered mesoporous black TiO_2 (OMBT) with a 2D hexagonal mesostructure possessing average pore diameter of ~9.6 nm, large pore volume (0.24 $cm^3\ g^{-1}$), and highly crystalline anatase pore walls (Fig. 35a).[137] The prepared mesoporous black TiO_2 exhibited a high SSA of 124 $m^2\ g^{-1}$, higher than the SSAs of many previously reported TiO_2 black materials with irregular NPs (<50 $m^2\ g^{-1}$). The porous structure is rather important for hydrogenation as it provided a high surface area to facilitate H_2 gas diffusion into TiO_2 and promote interactions with its inner

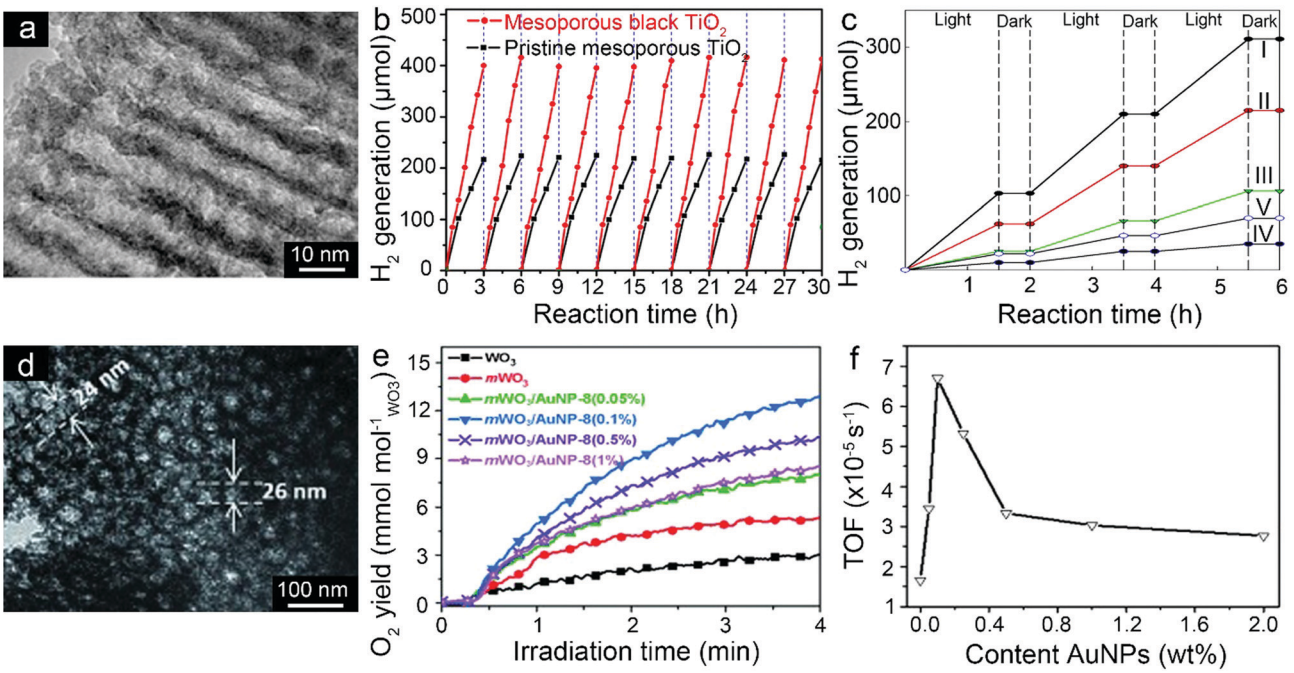

Fig. 35 Mesoporous materials for photocatalytic water splitting. (a) Representative TEM image ([110] plane) of ordered mesoporous black TiO_2 materials. (b) Cycling stability of photocatalytic hydrogen generation under air mass 1.5 (AM 1.5) for ordered mesoporous black TiO_2 (red) and pristine ordered mesoporous TiO_2 materials (black). (a and b) Reproduced with permission.[137] Copyright 2014, American Chemical Society. (c) Time course of H_2 evolution for mesoporous Nb_2O_5 calcined at 450 °C (I), 500 °C (II), 650 °C (III), commercial Nb_2O_5 (IV), and commercial TiO_2 (V). Reproduced with permission.[422] Copyright 2011, Elsevier. (d) TEM image of mWO_3/AuNP loaded with 0.1 wt% AuNPs (with an average diameter of 8 nm). (e) O_2 evolution curves using the mWO_3/AuNP hybrid catalysts with various loading contents of AuNPs. (f) Turnover frequency plot of the hybrid catalyst as a function of AuNP loading. (d–f) Reproduced with permission.[114] Copyright 2015, Wiley-VCH.

skeleton. Furthermore, the ordered mesostructure was sufficiently stable that it could be retained during the phase transition (from anatase to rutile) and crystal growth processes and during hydrogenation at 500 °C. The unique advantages of the mesoporous structure enabled OMBT to extend the photoresponse of the UV light to visible and infrared light regions, leading to a very high photocatalytic hydrogen evolution rate of 136.2 μmol h^{-1}, which was about two times higher than that of pristine OMT (76.6 μmol h^{-1}) (Fig. 35b). Additionally, many other strategies, such as changing the structural parameters (*e.g.*, size, shape, crystallinity, and porosity) of TiO_2-based materials, have been used to improve the catalytic performance.[137]

Many niobium-based compounds (*e.g.*, Nb_2O_5, $Sr_2Nb_2O_7$, $NiNbO_3$) have been reported to be effective photocatalysts for splitting water into H_2 and O_2 due to their beneficial electronic configuration (d^0 or d^{10}).[421] For example, Lin *et al.* synthesized mesoporous Nb_2O_5 with cylindrical pores of ~7.7 nm.[422] Due to the abundant active sites provided by its large SSA (108 m^2 g^{-1}), the synthesized mesoporous Nb_2O_5 exhibited a high generation rate of H_2 (328 μmol h^{-1} g^{-1}), nearly 39 times higher than that of non-porous Nb_2O_5 (Fig. 35c). The photocatalytic performance could be further improved by orders of magnitude by loading various metals or metal oxides (*e.g.*, Pt, Au, Cu, and NiO) into mesoporous Nb_2O_5 as co-catalysts. The mesoporous structure allowed these NPs to be well-distributed throughout the structure. Moreover, these metal NPs with strong negative potentials could significantly enhance the photocatalytic efficiency for the water splitting reaction.[422]

4.3.3.2 Photocatalytic oxygen evolution. Photocatalysts for water oxidation (or oxygen evolution) have also been investigated to improve the whole catalytic efficiency of photocatalytic water splitting.[388,423] In this field, noble-metal NPs (*e.g.*, Au and Ag) combined with mesoporous semiconducting catalysts (*e.g.*, TiO_2, CeO_2, and WO_3) are ideal candidates to achieve high performance for photochemical water splitting.[414] First, semiconducting catalysts with mesoporous structures can improve the transport of liquid educts and gaseous products into and out of the mesopores. Second, the incorporation of noble metal NPs into mesoporous catalysts can maximize the binding of reactants (such as water) and catalytic centers as well as shorten the diffusion distance of excitons.[114,164] For instance, He *et al.* prepared mesoporous tungsten oxide/Au NP (mWO_3/AuNP) hybrid catalysts possessing spherical pores with mean pore size of 25 nm and wall thickness of 18 nm (Fig. 35d).[114] When used as photocatalysts for water oxidation testing under visible light ($\lambda > 400$ nm), the mesostructured WO_3 catalyst kinetically enhanced the production rate of O_2, reaching a high amount of ~5.8 mmol mol_W^{-1} after 4 minutes, which was nearly twice that of non-porous WO_3 (~3.0 mmol mol_W^{-1}) (Fig. 35e). The moderate loading (~0.1 wt%) of Au NPs in the prepared mesoporous WO_3 maximized the binding of reactants (*e.g.*, water) with catalytic centers and shortened the exciton diffusion distance, thereby further improving the yield of O_2 up to ~13 mmol mol_W^{-1} after testing for 4 minutes, outperforming previously reported values.[424,425] Furthermore, the slope of the O_2 generation curve sharply increased and the turnover frequency (TOF) of mWO_3/AuNP-8 (0.1%) peaked at 6.73×10^{-5} s^{-1} (Fig. 35f), approximately four times higher than that of the pristine mesoporous WO_3 catalyst.[114]

4.4 Solar cells

Solar cells, which can directly convert solar energy into electrical energy through the photovoltaic effect, are one of the most promising energy conversion devices for the production of clean and sustainable energy.[426] Apart from traditional crystalline silicon solar cells, the emerging dye-sensitized solar cells (DSSCs) and perovskite solar cells (PSCs) have attracted tremendous interest as the third-generation solar cells, due to their high conversion efficiency, facile fabrication, and environmental friendliness.

4.4.1 Dye-sensitized solar cells. In a typical DSSC,[426] a dense TiO_2 layer (hole blocking layer) and a mesoporous semiconducting layer (*e.g.*, TiO_2, CeO_2, ZnO, NiO) are sequentially deposited on the conductive substrate as a photoanode, followed by adsorption of dye molecules and then the electrolyte is filled into the device. Subsequently, the mesoporous catalyst (as a counter electrode) is deposited on a conductive substrate for the electrocatalytic reduction of the electrolyte. High-performance DSSCs rely on a high interfacial area as charge carriers are generated only in the chemisorbed monolayer of the photoactive dye.[153] Mesoporous semiconducting materials, such as TiO_2, show great potential in DSSCs, because their high surface area enables the large-scale adsorption of dyes, which promotes the photogeneration of charge carriers and effectively reduces the charge recombination rate. In 1991, O'Regan and Grätzel fabricated a mesoporous TiO_2 film with a thickness of 10 μm as a photoanode for a DSSC which achieved a high conversion efficiency of 7.9%, 1000-fold higher than that of the non-porous TiO_2 film.[427] The high efficiency is contributed by the sufficient dye adsorption on the surface of the mesoporous TiO_2 film and the close bond between the monomolecular dye and the semiconductor film, which facilitated the trapping of light and increased the efficiency of electron injection. Benefiting from the large pore size and high pore volume, mesoporous TiO_2 also allows for effective post-deposition of semiconductor nanomaterials with a small bandgap inside the large, open mesopores, which is hard to achieve by micropores. For instance, Zhao *et al.* deposited cadmium sulfide quantum dots (5 nm in diameter) in mesoporous TiO_2, leading to excellent photoelectrochemical performance, with optimized photocurrent density of 6.03 mA cm^{-1} and high photoconversion efficiency of 3.9%.[428] Later, mesoporous photoanodes synthesized by BCP templates were reported for their capability for increasing the efficiency and long-term stability of DSSCs owing to the precise control of pore size, pore structure, and crystallinity.[145,429–434]

Liu *et al.* demonstrated the utilization of mesoporous TiO_2 microspheres with cylindrical pores as the photoanode.[435] The TiO_2 spheres (800 nm in average diameter) had radially oriented hexagonal mesochannels and highly crystalline anatase walls with uniform pore size of 5.5 nm, large accessible SSA (112 m^2 g^{-1}), and large pore volume (0.164 cm^3 g^{-1}) (Fig. 36a). The assembled DSSC employing the mesoporous TiO_2 microspheres as the photoanode film exhibited high short-circuit photocurrent density (J_{sc}) of

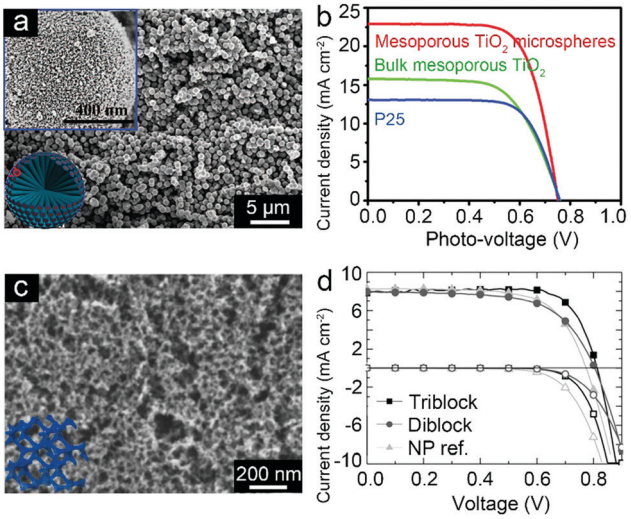

Fig. 36 Mesoporous TiO_2 with different pore structures as photoanodes of DSSCs. (a) SEM image of the mesoporous TiO_2 microspheres. Inset: SEM image of a single mesoporous TiO_2 microsphere and the corresponding structural scheme. (b) Current–voltage (J–V) curves of DSSCs fabricated using three different TiO_2 samples with N719 dye under AM 1.5 simulated sunlight with a power density of 100 mW cm^{-2}. (a and b) Reproduced with permission.[435] Copyright 2015, American Association for the Advancement of Science. (c) SEM image of a film consisting of a continuous TiO_2 network and the corresponding structural scheme. (d) J–V curves of solid-state DSSCs employing C220 as the dye sensitizer. (c and d) Reproduced with permission.[153] Copyright 2012, Wiley-VCH.

$\sim$22.91 mA cm^{-2} and open-circuit voltage (V_{oc}) of $\sim$0.75 V, leading to a power conversion efficiency (PCE) of $\sim$12.1% (Fig. 36b). In sharp contrast, the PCEs of DSSCs assembled using bulk and commercial TiO_2 were $\sim$7.6 and 6.8%, respectively. The higher performance was ascribed to the larger SSA of the mesoporous TiO_2, which enabled the loading of twice the amount of dyes compared with the bulk and commercial TiO_2. In addition, the DSSC assembled using the mesoporous TiO_2 microspheres showed good reliability verified by 15 individual solar cells, with a relatively close average PCE value of $\sim$12.1%.[435]

Metal oxides with bicontinuous porous structures can serve as highly porous photoanodes with extraordinary advantages in DSSCs. For example, Snaith and colleagues employed a mesoporous TiO_2 film with a gyroid structure as a photoanode material.[153] Compared to the traditional TiO_2 nanoparticle-based film, the mesoporous TiO_2 film with a 3D continuous network of anatase TiO_2 possessed higher porosity (61 vol%), larger internal SSA (161 m^2 g^{-1}), and larger pore size (21 nm in diameter), thus enabling high dye-loading capacity (Fig. 36c). The bicontinuous TiO_2 as a photoanode proved to be highly effective in solid-state DSSCs (Fig. 36d), with high J_{sc} of 7.9 mA cm^{-2}, V_{oc} of 0.81 V, and PCE of 5.0%, which is 16% higher than those of standard optimized TiO_2 nanoparticle-based device.[153]

4.4.2 Perovskite solar cells. As one of the most promising devices derived from DSSCs, organic–inorganic hybrid perovskite solar cells (PSCs) have a similar working principle to DSSCs.[436–438] The perovskite absorber performs the functions of light absorption and long-range charge transport, thereby eliminating the need for mesoporous semiconductors. Under illumination, the perovskite loaded in the porous scaffold generates electron–hole pairs, and then the electrons and holes are transported into the electron transport layer (*e.g.*, compact TiO_2) and the hole-transporting material, respectively. A number of advantages, including strong solar absorption and low non-radiative carrier recombination rates, endow perovskites with high performance for PSCs.[436,438]

Porous materials (*e.g.*, TiO_2, Al_2O_3) have been utilized as scaffolds to confine the growth of perovskite pigments.[439] For example, an interconnected porous structure with uniform pore size was previously used for the loading of perovskites.[440] Perovskite layers were prepared on the top of the porous TiO_2 layer and the as-formed perovskite crystals were confined in the pores of TiO_2. The porous morphology of TiO_2 with large pore size, high porosity, and good interconnectivity could facilitate the penetration of perovskites. By varying the pore size (30–70 nm) and film thickness (300–800 nm) of the porous TiO_2 layer, the optimum device performance was obtained with a mean pore size of 70 nm and a film thickness of 300 nm, which resulted in an excellent PCE of 11.9%. Furthermore, the performance of mesoporous TiO_2 films for PSCs can be improved by doping. For example, Nd-doped mesoporous TiO_2 electrodes with uniform pore size of 33 nm and thickness of 150 nm were used for the loading of perovskite pigments.[124,125] Substitutional Nd-doping increased the electron transport and reduced charge recombination in the mesoporous TiO_2, leading to much enhanced stability and performance of PSCs. The optimized doping concentration of 0.3% Nd endowed the PSC with a V_{oc} of 1.13 V, a J_{sc} of 22.3 mA cm^{-2}, and a stabilized PCE of $>$18%. The replacement of mesoporous TiO_2 with an insulating Al_2O_3 scaffold has proven to increase the open-circuit voltage of the PSC device because the deep electron traps in non-stoichiometric TiO_2 could reduce the splitting of the quasi-Fermi levels under illumination. For example, a series of methylammonium lead tri-iodide/chloride perovskites loaded in mesoporous Al_2O_3 have been utilized in PSCs, which resulted in apparently enhanced PSC performance.[434] The perovskite-Al_2O_3 films had interconnected pores in both in-plane and out-of-plane directions with mean pore diameter of 36 nm and film thicknesses between 70–80 nm, resulting in a V_{oc} of 0.96 V, a J_{sc} of 19.7 mA cm^{-2}, and a stable PCE greater than 9%.[434]

5. Summary and outlook

This article summarizes the progress and achievements in BCP self-assembly guided synthesis of mesoporous materials for ESC applications over the last 10 years. First, we introduce the basic principles of the self-assembly of BCPs both in the bulk and in solution, which provide guidance for the controllable preparation of a wide range of ordered self-assembled structures by adjusting the packing parameter of the BCP chains. With the various ordered structures as the soft templates, the BCP self-assembly guided synthetic strategy offers flexible control over the morphology and pore size/shape of mesoporous materials. Second, the currently prevalent synthetic strategies are discussed, which include bulk self-assembly, EISA, nanoprecipitation,

interfacial self-assembly, and emulsion-templating self-assembly. Through these elegant protocols, a diversity of mesoporous materials with tunable dimensionalities and morphologies have been achieved, including 1D porous nanocylinders/nanotubes, 2D porous nanosheets/films, and 3D porous (hollow) spheres/cubes/anisotropic particles/monoliths, among others. Meanwhile, the flexible pore structure control leads to the creation of spherical, cylindrical, bicontinuous and hierarchical pores with tailorable sizes, which may balance the relation between effective surface area and pore volume, ultimately governing the functional performance of mesoporous materials. Third, this paper overviews the potential applications of mesoporous materials in various ESC systems, including secondary batteries, supercapacitors, electro- or photo-catalysis, and solar cells. In these ESC applications, mesoporous materials can provide a large amount of active sites, fast diffusion of electrolyte ions, and good accommodation of volume expansion during the repeated cycling. Compared with micropores, for example, mesoporous materials with larger pore sizes enable the loading or adsorption of large-sized molecules or species, *e.g.* ions, organic electrolyte molecules and NPs, *etc.*, which are required by many ESC devices. Although microporous materials have large surface areas, most of the micropores are closed or exhibit narrow bottle-necks, which are difficult to contact by electrolyte, leading to poor utilization of the surface area. Furthermore, micropores are generally inaccessible to hydrated/solvated ions, leading to the poor wettablity of microporous materials. These problems can be solved by introducing mesopores to enhance the energy density and power capability of energy storage devices or catalytic performance of porous catalysts. On the other hand, the difference in pore structure may result in different mass transport modes in the interior of materials, thus affecting the effective surface areas and the amount of accessible active sites. For instance, cylindrical pores facilitate smoother and faster mass transport pathways compared to spherical pores. Particularly, in 2D materials, the in-plane cylindrical pores are favorable for promoting smooth mass and ion transport, which overcomes a common problem for 2D materials when they are tightly stacked. Further, bicontinuous structures with total continuity in all three dimensions can offer superior mass transport and provide highly accessible pore channels for electrolytes. Hierarchical porous materials combine the advantages of macro-, meso- and micropores, thus affording tailoring of the functional performance of mesoporous materials as per the requirements of different ESC devices.

In spite of the remarkable achievements in the field of BCP-templated mesoporous materials, there are still a myriad of challenges and also opportunities on the way. For example, (1) it is desirable and challenging to prepare mesoporous materials with new compositions such as metal carbides, nitrides, chalcogenides, phosphides and their hybrids, in view of their attractive properties and applications in various fields. For example, mesoporous niobium nitrides have proven to show excellent superconductor performance with a critical temperature of about 7–8 K. (2) It remains challenging to prepare bicontinuous mesoporous materials, in particular double diamond and double primitive structures, which have so far been limited to SiO_2, TiO_2, and Al_2O_3. It will be necessary to find appropriate self-assembly conditions and plot morphological phase diagrams for the controllable preparation of these bicontinuous structures. Moreover, it will be interesting to extend bicontinuous structures to a wider spectrum of mesoporous materials for ESC applications and investigate the effect of the pore architecture on their device performance. (3) For the important and versatile emulsion-templating method, most of the self-assembly mechanisms remain unclear, leading to difficulties in achieving the precise structural control of mesoporous materials. (4) Although large surface area and porosity of mesoporous materials can provide enhanced capacity or activity, these features may also lead to some disadvantages. For example, in rechargeable batteries, the high surface area of mesoporous materials may enhance the reactivity with the electrolyte and lead to uncontrolled solid electrolyte interface reactions. Moreover, mesoporous materials typically suffer from low volumetric energy and power densities when utilized in energy storage devices, such as batteries and supercapacitors. Similarly, in solar cell applications, the high surface area and defect-rich nature of mesoporous materials can lead to increased trap states and charge recombination, thereby lowering the overall conversion efficiency. To solve these problems, it is necessary to balance the different characteristics of mesoporous materials and optimize the performance of ESC devices. To this end, the structural, surface and electronic properties of mesoporous materials, as well as the charge transfer/storage mechanisms, need to be understood deeply *via* both substantial experiments and theoretical simulations. (5) It will also be challenging to make a breakthrough in the exploration of future applications for mesoporous materials. In energy storage systems, mesoporous materials have been widely studied for common rechargeable batteries and supercapacitors. In the near future, mesoporous materials can be developed for electrode materials of emerging state-of-the-art energy storage devices. For example, in high energy density metal–air batteries such as lithium–oxygen batteries, mesoporous materials are desirable to confine ultrafine NPs (*e.g.* metal oxides) with exposed active sites, while the mesopores can provide smooth transport of ions/electrons. In addition, it will be very interesting and promising to develop mesoporous materials as printable electrodes for 3D-printed energy devices such as batteries and supercapacitors. Another emerging energy storage device is the rechargeable desalination battery, which can store and release salt ions repeatedly through the charging and discharging process. This type of battery not only generates electricity from salinity differences, but also extracts sodium and chloride ions from seawater and produces fresh water. Based on similar operation principles of alkali metal-ion batteries or supercapacitors, mesoporous materials, such as carbons and metal oxides, exhibit great potential for this promising application. On the other hand, in some emerging energy conversion applications, *e.g.* electro/photocatalytic CO_2 or N_2 reduction to value-added chemicals or fuels, mesoporous materials, such as heteroatom- and/or metal-doped mesoporous carbons, metal carbides or chalcogenides, and hierarchically porous MOFs/COFs, hold great promise if their energy bands and electronic structures

can be well tuned. (6) To be commercially viable for energy applications, major challenges also involve the reduction of the high cost and the large-scale production of mesoporous materials. Laboratory-made BCPs and most of the currently employed precursors are expensive and difficult to produce in large amounts. Therefore, systematic studies on the manufacturing of low-cost BCPs and economic analysis on the fabrication of mesoporous materials need to be performed to increase their feasibility for industrial production.

Conflicts of interest

There are no conflicts to declare.

Acknowledgements

Y. M. is grateful for the financial support from the National Natural Science Foundation of China (21774076 and 51573091), the Program of the Shanghai Committee of Science and Technology (17JC1403200), the Program of Shanghai Academic Research Leader (19XD1421700), and the Program of Distinguished Professor of Special Appointment at Shanghai Institutions of Higher Learning. Y. Y. appreciates the Australian Research Council (ARC) for granting Future Fellowship (FT150100479) and Linkage (LP180100429).

References

1 M. C. Orilall and U. Wiesner, *Chem. Soc. Rev.*, 2011, **40**, 520–535.
2 W. Li, J. Liu and D. Zhao, *Nat. Rev. Mater.*, 2016, **1**, 16023.
3 M. R. Benzigar, S. N. Talapaneni, S. Joseph, K. Ramadass, G. Singh, J. Scaranto, U. Ravon, K. Al-Bahily and A. Vinu, *Chem. Soc. Rev.*, 2018, **47**, 2680–2721.
4 M. E. Davis, *Nature*, 2002, **417**, 813–821.
5 D. Wu, F. Xu, B. Sun, R. Fu, H. He and K. Matyjaszewski, *Chem. Rev.*, 2012, **112**, 3959–4015.
6 H. Sun, J. Zhu, D. Baumann, L. Peng, Y. Xu, I. Shakir, Y. Huang and X. Duan, *Nat. Rev. Mater.*, 2019, **4**, 45–60.
7 J. Chmiola, G. Yushin, Y. Gogotsi, C. Portet, P. Simon and P.-L. Taberna, *Science*, 2006, **313**, 1760–1763.
8 J. Huang, B. G. Sumpter and V. Meunier, *Angew. Chem., Int. Ed.*, 2008, **47**, 520–524.
9 H. Tian, Z. Lin, F. Xu, J. Zheng, X. Zhuang, Y. Mai and X. Feng, *Small*, 2016, **12**, 3155–3163.
10 H. Tian, S. Zhu, F. Xu, W. Mao, H. Wei, Y. Mai and X. Feng, *ACS Appl. Mater. Interfaces*, 2017, **9**, 43975–43982.
11 S. Zhu, H. Tian, N. Wang, B. Chen, Y. Mai and X. Feng, *Small*, 2018, **14**, 1702755.
12 H. Tian, J. Qin, D. Hou, Q. Li, C. Li, Z.-S. Wu and Y. Mai, *Angew. Chem., Int. Ed.*, 2019, **58**, 10173–10178.
13 N. Wang, D. Hou, Q. Li, P. Zhang, H. Wei and Y. Mai, *ACS Appl. Energy Mater.*, 2019, **2**, 5816–5823.
14 E. J. Crossland, M. Kamperman, M. Nedelcu, C. Ducati, U. Wiesner, D.-M. Smilgies, G. E. Toombes, M. A. Hillmyer, S. Ludwigs, U. Steiner and H. J. Snaith, *Nano Lett.*, 2008, **9**, 2807–2812.
15 J. Werner, G. Rodríguez-Calero, H. Abruña and U. Wiesner, *Energy Environ. Sci.*, 2018, **11**, 1261–1270.
16 H.-Y. Hsueh, C.-T. Yao and R.-M. Ho, *Chem. Soc. Rev.*, 2015, **44**, 1974–2018.
17 L. Borchardt, Q.-L. Zhu, M. E. Casco, R. Berger, X. Zhuang, S. Kaskel, X. Feng and Q. Xu, *Mater. Today*, 2017, **20**, 592–610.
18 J. Wu, F. Xu, S. Li, P. Ma, X. Zhang, Q. Liu, R. Fu and D. Wu, *Adv. Mater.*, 2019, **31**, 1802922.
19 X. Fei, W. Li, Z. Shao, S. Seeger, D. Zhao and X. Chen, *J. Am. Chem. Soc.*, 2014, **136**, 15781–15786.
20 N. D. Petkovich and A. Stein, *Chem. Soc. Rev.*, 2013, **42**, 3721–3739.
21 V. Malgras, H. Ataee-Esfahani, H. Wang, B. Jiang, C. Li, K. C. W. Wu, J. H. Kim and Y. Yamauchi, *Adv. Mater.*, 2016, **28**, 993–1010.
22 K. S. Lakhi, D.-H. Park, K. Al-Bahily, W. Cha, B. Viswanathan, J.-H. Choy and A. Vinu, *Chem. Soc. Rev.*, 2017, **46**, 72–101.
23 Y. Deng, J. Wei, Z. Sun and D. Zhao, *Chem. Soc. Rev.*, 2013, **42**, 4054–4070.
24 W. Li, Q. Yue, Y. Deng and D. Zhao, *Adv. Mater.*, 2013, **25**, 5129–5152.
25 S. S. Han, J. L. Mendoza-Cortés and W. A. Goddard III, *Chem. Soc. Rev.*, 2009, **38**, 1460–1476.
26 S. M. Rogge, A. Bavykina, J. Hajek, H. Garcia, A. I. Olivos-Suarez, A. Sepúlveda-Escribano, A. Vimont, G. Clet, P. Bazin, F. Kapteijn, M. Daturi, E. V. Ramos-Fernandez, F. X. Llabrés i Xamena, V. Van Speybroeck and J. Gascon, *Chem. Soc. Rev.*, 2017, **46**, 3134–3184.
27 M. Zhao, Y. Huang, Y. Peng, Z. Huang, Q. Ma and H. Zhang, *Chem. Soc. Rev.*, 2018, **47**, 6267–6295.
28 S.-Y. Ding and W. Wang, *Chem. Soc. Rev.*, 2013, **42**, 548–568.
29 S. Dalapati, C. Gu and D. Jiang, *Small*, 2016, **12**, 6513–6527.
30 C. S. Diercks and O. M. Yaghi, *Science*, 2017, **355**, eaal1585.
31 J. L. Segura, M. J. Mancheno and F. Zamora, *Chem. Soc. Rev.*, 2016, **45**, 5635–5671.
32 A. K. Mandal, J. Mahmood and J. B. Baek, *ChemNanoMat*, 2017, **3**, 373–391.
33 Y. Zheng, L. Lin, X. Ye, F. Guo and X. Wang, *Angew. Chem., Int. Ed.*, 2014, **53**, 11926–11930.
34 B. Lin, G. Yang and L. Wang, *Angew. Chem., Int. Ed.*, 2019, **58**, 4587–4591.
35 Y. Ren, Z. Ma and P. G. Bruce, *Chem. Soc. Rev.*, 2012, **41**, 4909–4927.
36 A. Blanazs, S. P. Armes and A. J. Ryan, *Macromol. Rapid Commun.*, 2009, **30**, 267–277.
37 Y. Mai and A. Eisenberg, *Chem. Soc. Rev.*, 2012, **41**, 5969–5985.
38 Z. Lin, S. Liu, W. Mao, H. Tian, N. Wang, N. Zhang, F. Tian, L. Han, X. Feng and Y. Mai, *Angew. Chem., Int. Ed.*, 2017, **56**, 7135–7140.
39 M. Templin, A. Franck, A. Du Chesne, H. Leist, Y. Zhang, R. Ulrich, V. Schädler and U. Wiesner, *Science*, 1997, **278**, 1795–1798.
40 J. Wei, Z. Sun, W. Luo, Y. Li, A. A. Elzatahry, A. M. Al-Enizi, Y. Deng and D. Zhao, *J. Am. Chem. Soc.*, 2017, **139**, 1706–1713.
41 J. Lee, M. C. Orilall, S. C. Warren, M. Kamperman, F. J. DiSalvo and U. Wiesner, *Nat. Mater.*, 2008, **7**, 222–228.

42 Y. Li, W. Luo, N. Qin, J. Dong, J. Wei, W. Li, S. Feng, J. Chen, J. Xu, A. A. Elzatahry, M. H. Es-Saheb, Y. Deng and D. Zhao, *Angew. Chem., Int. Ed.*, 2014, **53**, 9035–9040.
43 Y. Zou, X. Zhou, Y. Zhu, X. Cheng, D. Zhao and Y. Deng, *Acc. Chem. Res.*, 2019, **52**, 714–725.
44 T. Zhao, A. Elzatahry, X. Li and D. Zhao, *Nat. Rev. Mater.*, 2019, 1–17.
45 Y. Zou, X. Zhou, J. Ma, X. Yang and Y. Deng, *Chem. Soc. Rev.*, 2020, **49**, 1173–1208.
46 F. S. Bates and G. H. Fredrickson, *Phys. Today*, 1999, **52**, 32–38.
47 C. J. Hawker and T. P. Russell, *MRS Bull.*, 2005, **30**, 952–966.
48 N. A. Lynd, A. J. Meuler and M. A. Hillmyer, *Prog. Polym. Sci.*, 2008, **33**, 875–893.
49 F. Xu, J. Zhang, P. Zhang, X. Luan and Y. Mai, *Mater. Chem. Front.*, 2019, **3**, 2283–2307.
50 R. L. Hailes, A. M. Oliver, J. Gwyther, G. R. Whittell and I. Manners, *Chem. Soc. Rev.*, 2016, **45**, 5358–5407.
51 J. Du and R. K. O'Reilly, *Chem. Soc. Rev.*, 2011, **40**, 2402–2416.
52 X. Zhang, L.-Y. Wang, J.-F. Xu, D.-Y. Chen, L.-Q. Shi, Y.-F. Zhou and Z.-H. Shen, *Acta Polym. Sin.*, 2019, **50**, 973–987.
53 F.-G. Xu, Y.-Y. Mai and Y.-F. Zhou, *Acta Polym. Sin.*, 2017, **2**, 274–282.
54 A. K. Khandpur, S. Foerster, F. S. Bates, I. W. Hamley, A. J. Ryan, W. Bras, K. Almdal and K. Mortensen, *Macromolecules*, 1995, **28**, 8796–8806.
55 M. W. Matsen and F. S. Bates, *Macromolecules*, 1996, **29**, 1091–1098.
56 F. S. Bates, *Science*, 1991, **251**, 898–905.
57 W. Zheng and Z.-G. Wang, *Macromolecules*, 1995, **28**, 7215–7223.
58 V. Abetz and R. Stadler, *Macromol. Symp.*, 1997, **113**, 19–26.
59 M. Li and C. K. Ober, *Mater. Today*, 2006, **9**, 30–39.
60 H.-C. Kim, S.-M. Park and W. D. Hinsberg, *Chem. Rev.*, 2009, **110**, 146–177.
61 Y. Zhai, Y. Dou, D. Zhao, P. F. Fulvio, R. T. Mayes and S. Dai, *Adv. Mater.*, 2011, **23**, 4828–4850.
62 D. G. Bucknall and H. L. Anderson, *Science*, 2003, **302**, 1904–1905.
63 D. E. Discher and F. Ahmed, *Annu. Rev. Biomed. Eng.*, 2006, **8**, 323–341.
64 J. N. Israelachvili, *Intermolecular and Surface Forces*, Elsevier, Amsterdam, 2011.
65 Y. Huang, Y. Mai, X. Yang, U. Beser, J. Liu, F. Zhang, D. Yan, K. Müllen and X. Feng, *J. Am. Chem. Soc.*, 2015, **137**, 11602–11605.
66 U. Tritschler, S. Pearce, J. Gwyther, G. R. Whittell and I. Manners, *Macromolecules*, 2017, **50**, 3439–3463.
67 D. Wu, F. Xu, Y. Huang, C. Chen, C. Yu, X. Feng, D. Yan and Y. Mai, *Macromolecules*, 2018, **51**, 161–172.
68 Y. Huang, W. T. Dou, F. Xu, H. B. Ru, Q. Gong, D. Wu, D. Yan, H. Tian, X. P. He, Y. Mai and X. Feng, *Angew. Chem., Int. Ed.*, 2018, **57**, 3366–3371.
69 F. Xu, C. Yu, A. Tries, H. Zhang, M. Kläui, K. Basse, M. R. Hansen, N. Bilbao, M. Bonn, H. I. Wang and Y. Mai, *J. Am. Chem. Soc.*, 2019, **141**, 10972–10977.
70 D. Gu and F. Schüth, *Chem. Soc. Rev.*, 2014, **43**, 313–344.
71 Y. Mai, F. Zhang and X. Feng, *Nanoscale*, 2014, **6**, 106–121.
72 T. Azzam and A. Eisenberg, *Angew. Chem., Int. Ed.*, 2006, **45**, 7443–7447.
73 D. Zhao, J. Feng, Q. Huo, N. Melosh, G. H. Fredrickson, B. F. Chmelka and G. D. Stucky, *Science*, 1998, **279**, 548–552.
74 S. Hudson, J. Cooney and E. Magner, *Angew. Chem., Int. Ed.*, 2008, **47**, 8582–8594.
75 P. Yang, D. Zhao, D. I. Margolese, B. F. Chmelka and G. D. Stucky, *Nature*, 1998, **396**, 152–155.
76 B. Y. Guan, L. Yu and X. W. Lou, *J. Am. Chem. Soc.*, 2016, **138**, 11306–11311.
77 T. Wang, Y. Sun, L. Zhang, K. Li, Y. Yi, S. Song, M. Li, Z. A. Qiao and S. Dai, *Adv. Mater.*, 2019, **31**, 1807876.
78 S. C. Warren, L. C. Messina, L. S. Slaughter, M. Kamperman, Q. Zhou, S. M. Gruner, F. J. DiSalvo and U. Wiesner, *Science*, 2008, **320**, 1748–1752.
79 M. Stefik, S. Guldin, S. Vignolini, U. Wiesner and U. Steiner, *Chem. Soc. Rev.*, 2015, **44**, 5076–5091.
80 K. Matyjaszewski, *Adv. Mater.*, 2018, **30**, 1706441.
81 J.-S. Wang and K. Matyjaszewski, *J. Am. Chem. Soc.*, 1995, **117**, 5614–5615.
82 M. Kato, M. Kamigaito, M. Sawamoto and T. Higashimura, *Macromolecules*, 1995, **28**, 1721–1723.
83 J. Chiefari, Y. Chong, F. Ercole, J. Krstina, J. Jeffery, T. P. Le, R. T. Mayadunne, G. F. Meijs, C. L. Moad, G. Moad and S. H. Thang, *Macromolecules*, 1998, **31**, 5559–5562.
84 R. Nicolaÿ, Y. Kwak and K. Matyjaszewski, *Chem. Commun.*, 2008, 5336–5338.
85 C. Boyer, V. Bulmus, T. P. Davis, V. Ladmiral, J. Liu and S. Perrier, *Chem. Rev.*, 2009, **109**, 5402–5436.
86 J. P. McGann, M. Zhong, E. K. Kim, S. Natesakhawat, M. Jaroniec, J. F. Whitacre, K. Matyjaszewski and T. Kowalewski, *Macromol. Chem. Phys.*, 2012, **213**, 1078–1090.
87 M. Zhong, S. Natesakhawat, J. P. Baltrus, D. Luebke, H. Nulwala, K. Matyjaszewski and T. Kowalewski, *Chem. Commun.*, 2012, **48**, 11516–11518.
88 M. Kopeć, R. Yuan, E. Gottlieb, C. M. Abreu, Y. Song, Z. Wang, J. F. Coelho, K. Matyjaszewski and T. Kowalewski, *Macromolecules*, 2017, **50**, 2759–2767.
89 K. Yan, L.-B. Kong, Y.-H. Dai, M. Shi, K.-W. Shen, B. Hu, Y.-C. Luo and L. Kang, *J. Mater. Chem. A*, 2015, **3**, 22781–22793.
90 K. Yan, L.-B. Kong, K.-W. Shen, Y.-H. Dai, M. Shi, B. Hu, Y.-C. Luo and L. Kang, *Appl. Surf. Sci.*, 2016, **364**, 850–861.
91 Z. Zhou and G. Liu, *Small*, 2017, **13**, 1603107.
92 Z. Zhou, T. Liu, A. U. Khan and G. Liu, *Sci. Adv.*, 2019, **5**, eaau6852.
93 J. M. Serrano, T. Liu, A. U. Khan, B. Botset, B. J. Stovall, Z. Xu, D. Guo, K. Cao, X. Hao, S. Cheng and G. Liu, *Chem. Mater.*, 2019, **31**, 8898–8907.
94 Y. Lin, X. Wang, G. Qian and J. J. Watkins, *Chem. Mater.*, 2014, **26**, 2128–2137.
95 M. Lazzari, D. Scalarone, C. Vazquez-Vazquez and M. A. López-Quintela, *Macromol. Rapid Commun.*, 2008, **29**, 352–357.

96 Y. Liu, Z. Wang, W. Teng, H. Zhu, J. Wang, A. A. Elzatahry, D. Al-Dahyan, W. Li, Y. Deng and D. Zhao, *J. Mater. Chem. A*, 2018, **6**, 3162–3170.
97 M. Ogawa, *J. Am. Chem. Soc.*, 1994, **116**, 7941–7942.
98 Y. Lu, R. Ganguli, C. A. Drewien, M. T. Anderson, C. J. Brinker, W. Gong, Y. Guo, H. Soyez, B. Dunn, M. H. Huang and J. I. Zink, *Nature*, 1997, **389**, 364–368.
99 B. Tian, X. Liu, B. Tu, C. Yu, J. Fan, L. Wang, S. Xie, G. D. Stucky and D. Zhao, *Nat. Mater.*, 2003, **2**, 159–163.
100 C. Liang, K. Hong, G. A. Guiochon, J. W. Mays and S. Dai, *Angew. Chem., Int. Ed.*, 2004, **43**, 5785–5789.
101 Y. Meng, D. Gu, F. Zhang, Y. Shi, H. Yang, Z. Li, C. Yu, B. Tu and D. Zhao, *Angew. Chem., Int. Ed.*, 2005, **44**, 7053–7059.
102 Y. Yamauchi, A. Sugiyama, R. Morimoto, A. Takai and K. Kuroda, *Angew. Chem., Int. Ed.*, 2008, **47**, 5371–5373.
103 J. Wei, H. Wang, Y. Deng, Z. Sun, L. Shi, B. Tu, M. Luqman and D. Zhao, *J. Am. Chem. Soc.*, 2011, **133**, 20369–20377.
104 Q. Yue, M. Wang, J. Wei, Y. Deng, T. Liu, R. Che, B. Tu and D. Zhao, *Angew. Chem., Int. Ed.*, 2012, **51**, 10368–10372.
105 C. Wang, J. Wei, Q. Yue, W. Luo, Y. Li, M. Wang, Y. Deng and D. Zhao, *Angew. Chem., Int. Ed.*, 2013, **52**, 11603–11606.
106 W. Luo, T. Zhao, Y. Li, J. Wei, P. Xu, X. Li, Y. Wang, W. Zhang, A. A. Elzatahry, A. Alghamdi, Y. Deng, L. Wang, W. Jiang, Y. Liu, B. Kong and D. Zhao, *J. Am. Chem. Soc.*, 2016, **138**, 12586–12595.
107 Y. Wan and D. Zhao, *Chem. Rev.*, 2007, **107**, 2821–2860.
108 J. Zhang, Y. Deng, J. Wei, Z. Sun, D. Gu, H. Bongard, C. Liu, H. Wu, B. Tu, F. Schüth and D. Zhao, *Chem. Mater.*, 2009, **21**, 3996–4005.
109 J. Zhang, Y. Deng, D. Gu, S. Wang, L. She, R. Che, Z. S. Wang, B. Tu, S. Xie and D. Zhao, *Adv. Energy Mater.*, 2011, **1**, 241–248.
110 S. Guldin, S. Hüttner, P. Tiwana, M. C. Orilall, B. Ülgüt, M. Stefik, P. Docampo, M. Kolle, G. Divitini, C. Ducati, S. A. T. Redfern, H. J. Snaith, U. Wiesner, D. Eder and U. Steiner, *Energy Environ. Sci.*, 2011, **4**, 225–233.
111 C. Reitz, J. Haetge, C. Suchomski and T. Brezesinski, *Chem. Mater.*, 2013, **25**, 4633–4642.
112 J. Wei, D. Zhou, Z. Sun, Y. Deng, Y. Xia and D. Zhao, *Adv. Funct. Mater.*, 2013, **23**, 2322–2328.
113 J. Yu, M. Guo, F. Muhammad, A. Wang, F. Zhang, Q. Li and G. Zhu, *Carbon*, 2014, **69**, 502–514.
114 B. Liu, C. H. Kuo, J. Chen, Z. Luo, S. Thanneeru, W. Li, W. Song, S. Biswas, S. L. Suib and J. He, *Angew. Chem., Int. Ed.*, 2015, **54**, 9061–9065.
115 Z. Wang, Y. Zhu, W. Luo, Y. Ren, X. Cheng, P. Xu, X. Li, Y. Deng and D. Zhao, *Chem. Mater.*, 2016, **28**, 7773–7780.
116 Y. Zhu, Y. Zhao, J. Ma, X. Cheng, J. Xie, P. Xu, H. Liu, H. Liu, H. Zhang, M. Wu, A. A. Elzatahry, A. Alghamdi, Y. Deng and D. Zhao, *J. Am. Chem. Soc.*, 2017, **139**, 10365–10373.
117 Y. Zou, B. Yang, Y. Liu, Y. Ren, J. Ma, X. Zhou, X. Cheng and Y. Deng, *Adv. Funct. Mater.*, 2018, **28**, 1806214.
118 X. Xiao, L. Liu, J. Ma, Y. Ren, X. Cheng, Y. Zhu, D. Zhao, A. A. Elzatahry, A. Alghamdi and Y. Deng, *ACS Appl. Mater. Interfaces*, 2018, **10**, 1871–1880.
119 J. Ma, Y. Ren, X. Zhou, L. Liu, Y. Zhu, X. Cheng, P. Xu, X. Li, Y. Deng and D. Zhao, *Adv. Funct. Mater.*, 2018, **28**, 1705268.
120 E. Ortel, A. Fischer, L. Chuenchom, J. Polte, F. Emmerling, B. Smarsly and R. Kraehnert, *Small*, 2012, **8**, 298–309.
121 D. Chandra, T. Ohji, K. Kato and T. Kimura, *Phys. Chem. Chem. Phys.*, 2011, **13**, 12529–12535.
122 B. P. Bastakoti, S. Ishihara, S.-Y. Leo, K. Ariga, K. C.-W. Wu and Y. Yamauchi, *Langmuir*, 2014, **30**, 651–659.
123 M. G. Fischer, X. Hua, B. D. Wilts, I. Gunkel, T. M. Bennett and U. Steiner, *ACS Appl. Mater. Interfaces*, 2017, **9**, 22388–22397.
124 S. K. Pathak, A. Abate, P. Ruckdeschel, B. Roose, K. C. Gödel, Y. Vaynzof, A. Santhala, S. I. Watanabe, D. J. Hollman, N. Noel, A. Sepe, U. Wiesner, R. Friend, H. J. Snaith and U. Steiner, *Adv. Funct. Mater.*, 2014, **24**, 6046–6055.
125 B. Roose, K. C. Gödel, S. Pathak, A. Sadhanala, J. P. C. Baena, B. D. Wilts, H. J. Snaith, U. Wiesner, M. Grätzel, U. Steiner and A. Abate, *Adv. Energy Mater.*, 2016, **6**, 1501868.
126 J. Lee, Y. S. Jung, S. C. Warren, M. Kamperman, S. M. Oh, F. J. DiSalvo and U. Wiesner, *Macromol. Chem. Phys.*, 2011, **212**, 383–390.
127 E. Ortel, T. Reier, P. Strasser and R. Kraehnert, *Chem. Mater.*, 2011, **23**, 3201–3209.
128 B. P. Bastakoti, Y. Li, S. Guragain, M. Pramanik, S. M. Alshehri, T. Ahamad, Z. Liu and Y. Yamauchi, *Chem. – Eur. J.*, 2016, **22**, 7463–7467.
129 S. Tanaka, B. P. Bastakoti, Y. L. S. I. Yusa, D. Ishii, K. Kani, A. Fatehmulla, W. A. Farooq, M. J. Shiddiky, Y. Bando, Y. V. Kaneti, Y. Yamauchi and M. S. A. Hossain, *Eur. J. Inorg. Chem.*, 2017, 1328–1332.
130 M. G. Fischer, X. Hua, B. D. Wilts, E. Castillo-Martínez and U. Steiner, *ACS Appl. Mater. Interfaces*, 2018, **10**, 1646–1653.
131 P. Yang, D. Zhao, D. I. Margolese, B. F. Chmelka and G. D. Stucky, *Chem. Mater.*, 1999, **11**, 2813–2826.
132 D. Chen, Z. Li, Y. Wan, X. Tu, Y. Shi, Z. Chen, W. Shen, C. Yu, B. Tu and D. Zhao, *J. Mater. Chem.*, 2006, **16**, 1511–1519.
133 Y. Mai and A. Eisenberg, *Macromolecules*, 2011, **44**, 3179–3183.
134 Y. J. Cheng, S. Zhou, M. Wolkenhauer, G. G. Bumbu, S. Lenz, M. Memesa, S. Nett, S. Emmerling, W. Steffen and J. S. Gutmann, *Eur. J. Inorg. Chem.*, 2013, 1127–1133.
135 J. Hwang, C. Jo, M. G. Kim, J. Chun, E. Lim, S. Kim, S. Jeong, Y. Kim and J. Lee, *ACS Nano*, 2015, **9**, 5299–5309.
136 E. Kang, Y. S. Jung, G. H. Kim, J. Chun, U. Wiesner, A. C. Dillon, J. K. Kim and J. Lee, *Adv. Funct. Mater.*, 2011, **21**, 4349–4357.
137 W. Zhou, W. Li, J.-Q. Wang, Y. Qu, Y. Yang, Y. Xie, K. Zhang, L. Wang, H. Fu and D. Zhao, *J. Am. Chem. Soc.*, 2014, **136**, 9280–9283.
138 G. S. Armatas, G. Bilis and M. Louloudi, *J. Mater. Chem.*, 2011, **21**, 2997–3005.
139 Y. Zhang, H. Tan, H. Li, Y.-Q. Liu, F. C. Kartawidjaja, Z.-C. Yang and J. Wang, *Chem. Mater.*, 2011, **23**, 2745–2752.
140 Z.-X. Li, F.-B. Shi, T. Zhang, H.-S. Wu, L.-D. Sun and C.-H. Yan, *Chem. Commun.*, 2011, **47**, 8109–8111.

141 K. Zimny, T. Roques-Carmes, C. Carteret, M. Stébé and J. Blin, *New J. Chem.*, 2012, **116**, 6585–6594.
142 J. Shim, J. Lee, Y. Ye, J. Hwang, S.-K. Kim, T.-H. Lim, U. Wiesner and J. Lee, *ACS Nano*, 2012, **6**, 6870–6881.
143 J. Hwang, S. H. Woo, J. Shim, C. Jo, K. T. Lee and J. Lee, *ACS Nano*, 2013, **7**, 1036–1044.
144 S. Lee, M. Choun, Y. Ye, J. Lee, Y. Mun, E. Kang, J. Hwang, Y. H. Lee, C. H. Shin, S. H. Moon, S. K. Kim, E. Lee and J. Lee, *Angew. Chem., Int. Ed.*, 2015, **54**, 9230–9234.
145 Y. Liu, R. Che, G. Chen, J. Fan, Z. Sun, Z. Wu, M. Wang, B. Li, J. Wei, Y. Wei, G. Wang, G. Guan, A. A. Elzatahry, A. A. Bagabas, A. M. Al-Enizi, Y. Deng, H. Peng and D. Zhao, *Sci. Adv.*, 2015, **1**, e1500166.
146 J. Fan, X. Ran, Y. Ren, C. Wang, J. Yang, W. Teng, L. Zou, Y. Sun, B. Lu and Y. Deng, *Langmuir*, 2016, **32**, 9922–9929.
147 M. Pramanik, J. Lee, S. Tominaka, Y. Ide, J. H. Kim and Y. Yamauchi, *J. Mater. Chem. A*, 2016, **4**, 18091–18099.
148 G. H. Wang, Z. Cao, D. Gu, N. Pfänder, A. C. Swertz, B. Spliethoff, H. J. Bongard, C. Weidenthaler, W. Schmidt, R. Rinaldi and F. Sthüth, *Angew. Chem., Int. Ed.*, 2016, **55**, 8850–8855.
149 W. Gao, W. Li, Z. Xue, M. Pal, Y. Liu, C. Wang, J. Wang, S. Wang, X. Wan, Y. Liu and D. Zhao, *New J. Chem.*, 2016, **40**, 4200–4205.
150 Y. Ren, X. Zhou, W. Luo, P. Xu, Y. Zhu, X. Li, X. Cheng, Y. Deng and D. Zhao, *Chem. Mater.*, 2016, **28**, 7997–8005.
151 W. Dong, Y. Yao, L. Li, Y. Sun, W. Hua, G. Zhuang, D. Zhao, S. Yan and W. Song, *Appl. Catal., B*, 2017, **217**, 293–302.
152 L. Han and S. Che, *Adv. Mater.*, 2018, **30**, 1705708.
153 P. Docampo, M. Stefik, S. Guldin, R. Gunning, N. A. Yufa, N. Cai, P. Wang, U. Steiner, U. Wiesner and H. J. Snaith, *Adv. Energy Mater.*, 2012, **2**, 676–682.
154 M. Stefik, S. Wang, R. Hovden, H. Sai, M. W. Tate, D. A. Muller, U. Steiner, S. M. Gruner and U. Wiesner, *J. Mater. Chem.*, 2012, **22**, 1078–1087.
155 J. G. Werner, T. N. Hoheisel and U. Wiesner, *ACS Nano*, 2013, **8**, 731–743.
156 Z. Li, K. Hur, H. Sai, T. Higuchi, A. Takahara, H. Jinnai, S. M. Gruner and U. Wiesner, *Nat. Commun.*, 2014, **5**, 3247.
157 J. G. Werner, M. R. Scherer, U. Steiner and U. Wiesner, *Nanoscale*, 2014, **6**, 8736–8742.
158 S. W. Robbins, H. Sai, F. J. DiSalvo, S. M. Gruner and U. Wiesner, *ACS Nano*, 2014, **8**, 8217–8223.
159 J. G. Werner, S. S. Johnson, V. Vijay and U. Wiesner, *Chem. Mater.*, 2015, **27**, 3349–3357.
160 S. W. Robbins, P. A. Beaucage, H. Sai, K. W. Tan, J. G. Werner, J. P. Sethna, F. J. DiSalvo, S. M. Gruner, R. B. Van Dover and U. Wiesner, *Sci. Adv.*, 2016, **2**, e1501119.
161 Q. Zhang, F. Matsuoka, H. S. Suh, P. A. Beaucage, S. Xiong, D.-M. Smilgies, K. W. Tan, J. R. G. Werner, P. F. Nealey and U. B. Wiesner, *ACS Nano*, 2017, **12**, 347–358.
162 W. C. Chu, B. P. Bastakoti, Y. V. Kaneti, J. G. Li, H. R. Alamri, Z. A. Alothman, Y. Yamauchi and S. W. Kuo, *Chem. – Eur. J.*, 2017, **23**, 13734–13741.
163 H. Li, Y. Liu, X. Cao, L. Han, C. Jiang and S. Che, *Angew. Chem., Int. Ed.*, 2017, **56**, 806–811.
164 T. Weller, L. Deilmann, J. Timm, T. S. Dörr, P. A. Beaucage, A. S. Cherevan, U. B. Wiesner, D. Eder and R. Marschall, *Nanoscale*, 2018, **10**, 3225–3234.
165 Y. Liu, W. Teng, G. Chen, Z. Zhao, W. Zhang, B. Kong, W. N. Hozzein, A. A. Al-Khalaf, Y. Deng and D. Zhao, *Chem. Sci.*, 2018, **9**, 7705–7714.
166 A. Monnier, F. Schüth, Q. Huo, D. Kumar, D. Margolese, R. Maxwell, G. Stucky, M. Krishnamurty, P. Petroff, A. Firouzi, M. Janicke and B. F. Chmelka, *Science*, 1993, **261**, 1299–1303.
167 F. Zhang, Y. Meng, D. Gu, Y. Yan, C. Yu, B. Tu and D. Zhao, *J. Am. Chem. Soc.*, 2005, **127**, 13508–13509.
168 L. Han, D. Xu, Y. Liu, T. Ohsuna, Y. Yao, C. Jiang, Y. Mai, Y. Cao, Y. Duan and S. Che, *Chem. Mater.*, 2014, **26**, 7020–7028.
169 A. C. Finnefrock, R. Ulrich, A. Du Chesne, C. C. Honeker, K. Schumacher, K. K. Unger, S. M. Gruner and U. Wiesner, *Angew. Chem., Int. Ed.*, 2001, **40**, 1207–1211.
170 A. C. Finnefrock, R. Ulrich, G. E. Toombes, S. M. Gruner and U. Wiesner, *J. Am. Chem. Soc.*, 2003, **125**, 13084–13093.
171 A. Jain, G. E. Toombes, L. M. Hall, S. Mahajan, C. B. Garcia, W. Probst, S. M. Gruner and U. Wiesner, *Angew. Chem., Int. Ed.*, 2005, **44**, 1226–1229.
172 D. W. Wang, F. Li, M. Liu, G. Q. Lu and H. M. Cheng, *Angew. Chem., Int. Ed.*, 2008, **47**, 373–376.
173 K. Shen, L. Zhang, X. Chen, L. Liu, D. Zhang, Y. Han, J. Chen, J. Long, R. Luque, Y. Li and B. Chen, *Science*, 2018, **359**, 206–210.
174 P. Hu, C. Chen, R. Zeng, J. Xiang, Y. Huang, D. Hou, Q. Li and Y. Huang, *Nano Energy*, 2018, **50**, 376–382.
175 Z. Liang, H. Liu, J. Zeng, J. Zhou, H. Li and H. Xia, *Nanoscale Res. Lett.*, 2018, **13**, 314.
176 Z. Xu, X. Zhuang, C. Yang, J. Cao, Z. Yao, Y. Tang, J. Jiang, D. Wu and X. Feng, *Adv. Mater.*, 2016, **28**, 1981–1987.
177 H. Sai, K. W. Tan, K. Hur, E. Asenath-Smith, R. Hovden, Y. Jiang, M. Riccio, D. A. Muller, V. Elser, L. A. Estroff, S. M. Gruner and U. Wiesner, *Science*, 2013, **341**, 530–534.
178 J. Hwang, S. Kim, U. Wiesner and J. Lee, *Adv. Mater.*, 2018, **30**, 1801127.
179 C. Jo, J. Hwang, W. G. Lim, J. Lim, K. Hur and J. Lee, *Adv. Mater.*, 2018, **30**, 1703829.
180 S. Kim, M. Ju, J. Lee, J. Hwang and J. Lee, *J. Am. Chem. Soc.*, 2020, **142**, 9250–9257.
181 T.-Y. Ma, H. Li, Q.-F. Deng, L. Liu, T.-Z. Ren and Z.-Y. Yuan, *Chem. Mater.*, 2012, **24**, 2253–2255.
182 S. Gao, G. Gody, W. Zhao, S. Perrier, X. Peng, C. Ducati, D. Zhao and A. K. Cheetham, *Chem. Sci.*, 2013, **4**, 3573–3577.
183 J. Huwang, T. Heil, M. Antonietti and B. V. K. J. Schmidt, *J. Am. Chem. Soc.*, 2018, **140**, 2947–2956.
184 Z. Li, X. Xing, D. Meng, Z. Wang, J. Xue, J. Chu, M. Li and Y. Yang, *iScience*, 2019, **15**, 514–523.
185 M. Zhang, L. Li, Q. Lin, M. Tang, Y. Wu and C. Ke, *J. Am. Chem. Soc.*, 2019, **141**, 5154–5158.
186 Q. Wang and D. Astruc, *Chem. Rev.*, 2020, **120**, 1438–1511.
187 A. K. Mandal, J. Mahmood and J.-B. Baek, *ChemNanoMat*, 2017, **3**, 373–391.

188 R. Dong, W. Liu and J. Hao, *Acc. Chem. Res.*, 2012, **45**, 504–513.
189 M. Sasidharan and K. Nakashima, *Acc. Chem. Res.*, 2013, **47**, 157–167.
190 J. Liu, N. P. Wickramaratne, S. Z. Qiao and M. Jaroniec, *Nat. Mater.*, 2015, **14**, 763–774.
191 X. Huang, X. Qi, F. Boey and H. Zhang, *Chem. Soc. Rev.*, 2012, **41**, 666–686.
192 X. Zhang and Y. Xie, *Chem. Soc. Rev.*, 2013, **42**, 8187–8199.
193 H.-P. Cong, J.-F. Chen and S.-H. Yu, *Chem. Soc. Rev.*, 2014, **43**, 7295–7325.
194 D. Deng, K. Novoselov, Q. Fu, N. Zheng, Z. Tian and X. Bao, *Nat. Nanotechnol.*, 2016, **11**, 218–230.
195 B. Mendoza-Sánchez and Y. Gogotsi, *Adv. Mater.*, 2016, **28**, 6104–6135.
196 X. Zhuang, Y. Mai, D. Wu, F. Zhang and X. Feng, *Adv. Mater.*, 2015, **27**, 403–427.
197 Y. He, X. Zhuang, C. Lei, L. Lei, Y. Hou, Y. Mai and X. Feng, *Nano Today*, 2019, **24**, 103–119.
198 B. Jiang, Y. Guo, J. Kim, A. E. Whitten, K. Wood, K. Kani, A. E. Rowan, J. Henzie and Y. Yamauchi, *J. Am. Chem. Soc.*, 2018, **140**, 12434–12441.
199 K. Lan, Y. Liu, W. Zhang, Y. Liu, A. Elzatahry, R. Wang, Y. Xia, D. Al-Dhayan, N. Zheng and D. Zhao, *J. Am. Chem. Soc.*, 2018, **140**, 4135–4143.
200 C. Li, M. Iqbal, J. Lin, X. Luo, B. Jiang, V. Malgras, K. C.-W. Wu, J. Kim and Y. Yamauchi, *Acc. Chem. Res.*, 2018, **51**, 1764–1773.
201 C. Li, Ö. Dag, T. D. Dao, T. Nagao, Y. Sakamoto, T. Kimura, O. Terasaki and Y. Yamauchi, *Nat. Commun.*, 2015, **6**, 6608.
202 C. Li, B. Jiang, Z. Wang, Y. Li, M. S. A. Hossain, J. H. Kim, T. Takei, J. Henzie, Ö. Dag, Y. Bando and Y. Yamauchi, *Angew. Chem., Int. Ed.*, 2016, **55**, 12746–12750.
203 M. Iqbal, Y. V. Kaneti, K. Kashimura, M. Yoshino, B. Jiang, C. Li, B. Yuliarto, Y. Bando, Y. Sugahara and Y. Yamauchi, *Nanoscale Horiz.*, 2019, **4**, 960–968.
204 D. Baba, J. Kim, J. Henzie, C. Li, B. Jiang, Ö. Dag, Y. Yamauchi and T. Asahi, *Chem. Commun.*, 2018, **54**, 10347–10350.
205 C. Li, T. Sato and Y. Yamauchi, *Angew. Chem., Int. Ed.*, 2013, **52**, 8050–8053.
206 K. Kani, J. Kim, B. Jiang, M. S. A. Hossain, Y. Bando, J. Henzie and Y. Yamauchi, *Nanoscale*, 2019, **11**, 10581–10588.
207 C. Li, B. Jiang, H. Chen, M. Imura, L. Sang, V. Malgras, Y. Bando, T. Ahamad, S. M. Alshehri, S. Tominaka and Y. Yamauchi, *Nano Res.*, 2016, **9**, 1752–1762.
208 Y. Yamauchi, A. Tonegawa, M. Komatsu, H. Wang, L. Wang, Y. Nemoto, N. Suzuki and K. Kuroda, *J. Am. Chem. Soc.*, 2012, **134**, 5100–5109.
209 B. Jiang, C. Li, H. Qian, M. S. A. Hossain, V. Malgras and Y. Yamauchi, *Angew. Chem., Int. Ed.*, 2017, **56**, 7836–7841.
210 A. S. Nugraha, V. Malgras, M. Iqbal, B. Jiang, C. Li, Y. Bando, A. Alshehri, J. Kim, Y. Yamauchi and T. Asahi, *ACS Appl. Mater. Interfaces*, 2018, **10**, 23783–23791.
211 M. Iqbal, J. Kim, B. Yuliarto, B. Jiang, C. Li, O. M. Dag, V. Malgras and Y. Yamauchi, *ACS Appl. Mater. Interfaces*, 2018, **10**, 40623–40630.
212 A. S. Nugraha, V. Malgras, J. Kim, J. Bo, C. Li, M. Iqbal, Y. Yamauchi and T. Asahi, *Small Methods*, 2018, **2**, 1800283.
213 H. Sun, Y. Zhu, B. Yang, Y. Wang, Y. Wu and J. Du, *J. Mater. Chem. A*, 2016, **4**, 12088–12097.
214 X. Li, J. Iocozzia, Y. Chen, S. Zhao, X. Cui, W. Wang, H. Yu, S. Lin and Z. Lin, *Angew. Chem., Int. Ed.*, 2018, **57**, 2046–2070.
215 C. Li, T. Rasheed, H. Tian, P. Huang, Y. Mai, W. Huang and Y. Zhou, *ACS Macro Lett.*, 2019, **8**, 331–336.
216 Y. Li, H. Tan, T. Takei, M. S. A. Hossain, M. T. Islam, S. M. Alshehri, T. Ahamad, R. R. Salunkhe, S. Pradhan, J. Henzie, Y. Yamauchi and K. Ariga, *Eur. J. Inorg. Chem.*, 2017, 5413–5416.
217 Y. Li, H. Tan, R. R. Salunkhe, J. Tang, L. K. Shrestha, B. P. Bastakoti, H. Rong, T. Takei, J. Henzie, Y. Yamauchi and K. Ariga, *Chem. Commun.*, 2017, **53**, 236–239.
218 M. Sasidharan, N. Gunawardhana, C. Senthil and M. Yoshio, *J. Mater. Chem. A*, 2014, **2**, 7337–7344.
219 Y. Fang, D. Gu, Y. Zou, Z. Wu, F. Li, R. Che, Y. Deng, B. Tu and D. Zhao, *Angew. Chem., Int. Ed.*, 2010, **49**, 7987–7991.
220 J. Tang, J. Liu, C. Li, Y. Li, M. O. Tade, S. Dai and Y. Yamauchi, *Angew. Chem., Int. Ed.*, 2015, **54**, 588–593.
221 B. Jiang, C. Li, Ö. Dag, H. Abe, T. Takei, T. Imai, M. S. A. Hossain, M. T. Islam, K. Wood, J. Henzie and Y. Yamauchi, *Nat. Commun.*, 2017, **8**, 15581.
222 B. Jiang, C. Li, M. Imura, J. Tang and Y. Yamauchi, *Adv. Sci.*, 2015, **2**, 1500112.
223 C. Zhu, D. Du, A. Eychmüller and Y. Lin, *Chem. Rev.*, 2015, **115**, 8896–8943.
224 V. Malgras, Q. Ji, Y. Kamachi, T. Mori, F.-K. Shieh, K. C.-W. Wu, K. Ariga and Y. Yamauchi, *Bull. Chem. Soc. Jpn.*, 2015, **88**, 1171–1200.
225 Y. Li, B. P. Bastakoti, V. Malgras, C. Li, J. Tang, J. H. Kim and Y. Yamauchi, *Angew. Chem., Int. Ed.*, 2015, **54**, 11073–11077.
226 B. Jiang, C. Li, V. Malgras, M. Imura, S. Tominaka and Y. Yamauchi, *Chem. Sci.*, 2016, **7**, 1575–1581.
227 C. Li, M. Iqbal, B. Jiang, Z. Wang, J. Kim, A. K. Nanjundan, A. E. Whitten, K. Wood and Y. Yamauchi, *Chem. Sci.*, 2019, **10**, 4054–4061.
228 B. Jiang, K. Kani, M. Iqbal, H. Abe, T. Kimura, M. S. A. Hossain, O. Anjaneyulu, J. Henzie and Y. Yamauchi, *Chem. Mater.*, 2018, **30**, 428–435.
229 Y. Kang, B. Jiang, Z. A. Alothman, A. Y. Badjah, M. Naushad, M. Habila, S. Wabaidur, J. Henzie, H. Li and Y. Yamauchi, *Chem. – Eur. J.*, 2019, **25**, 343–348.
230 Y. Li, C. Li, B. P. Bastakoti, J. Tang, B. Jiang, J. Kim, M. Shahabuddin, Y. Bando, J. H. Kim and Y. Yamauchi, *J. Mater. Chem. A*, 2016, **4**, 9169–9176.
231 H. Wang, H. Yu, Y. Li, S. Yin, H. Xue, X. Li, Y. Xu and L. Wang, *Nanotechnology*, 2018, **29**, 175403.
232 C. Park, J. Jung, C. W. Lee and J. Cho, *Sci. Rep.*, 2016, **6**, 39136.
233 Y. Guo, J. Tang, J. Henzie, B. Jiang, H. Qian, Z. Wang, H. Tan, Y. Bando and Y. Yamauchi, *Mater. Horiz.*, 2017, **4**, 1171–1177.
234 H. Ilbeygi, I. Y. Kim, M. G. Kim, W. Cha, P. S. M. Kumar, D. H. Park and A. Vinu, *Angew. Chem., Int. Ed.*, 2019, **58**, 10849–10854.

235 B. Liu, L. Jin, H. Zheng, H. Yao, Y. Wu, A. Lopes and J. He, *ACS Appl. Mater. Interfaces*, 2017, **9**, 1746–1758.
236 H. Tan, Y. Li, X. Jiang, J. Tang, Z. Wang, H. Qian, P. Mei, V. Malgras, Y. Bando and Y. Yamauchi, *Nano Energy*, 2017, **36**, 286–294.
237 Y. Zhang, Y. Liu, W. Liu, X. Li and L. Mao, *Appl. Surf. Sci.*, 2017, **407**, 64–71.
238 F. Zhang, D. Gu, T. Yu, F. Zhang, S. Xie, L. Zhang, Y. Deng, Y. Wan, B. Tu and D. Zhao, *J. Am. Chem. Soc.*, 2007, **129**, 7746–7747.
239 D. Liu, J.-H. Lei, L.-P. Guo and K.-J. Deng, *Carbon*, 2011, **49**, 2113–2119.
240 M. Li and J. Xue, *J. Colloid Interface Sci.*, 2012, **377**, 169–175.
241 Z. Lin, H. Tian, F. Xu, X. Yang, Y. Mai and X. Feng, *Polym. Chem.*, 2016, **7**, 2092–2098.
242 J. Liang, X. Y. Yu, H. Zhou, H. B. Wu, S. Ding and X. W. Lou, *Angew. Chem., Int. Ed.*, 2014, **53**, 12803–12807.
243 H. Yu, X. Qiu, S. P. Nunes and K.-V. Peinemann, *Nat. Commun.*, 2014, **5**, 4110.
244 Y. La, C. Park, T. J. Shin, S. H. Joo, S. Kang and K. T. Kim, *Nat. Chem.*, 2014, **6**, 534–541.
245 C. Park, Y. La, T. H. An, H. Y. Jeong, S. Kang, S. H. Joo, H. Ahn, T. J. Shin and K. T. Kim, *Nat. Commun.*, 2015, **6**, 6392.
246 K. H. Ku, J. M. Shin, D. Klinger, S. G. Jang, R. C. Hayward, C. J. Hawker and B. J. Kim, *ACS Nano*, 2016, **10**, 5243–5251.
247 A. Cho, Y. La, T. J. Shin, C. Park and K. T. Kim, *Macromolecules*, 2016, **49**, 4510–4519.
248 H. He, K. Rahimi, M. Zhong, A. Mourran, D. R. Luebke, H. B. Nulwala, M. Möller and K. Matyjaszewski, *Nat. Commun.*, 2017, **8**, 14057.
249 X. Lyu, A. Xiao, W. Zhang, P. Hou, K. Gu, Z. Tang, H. Pan, F. Wu, Z. Shen and X. H. Fan, *Angew. Chem., Int. Ed.*, 2018, **57**, 10132–10136.
250 F. Lv, Z. An and P. Wu, *Nat. Commun.*, 2019, **10**, 1397.
251 S. Ha, Y. La and K. T. Kim, *Acc. Chem. Res.*, 2020, **53**, 620–631.
252 Z. Lin, J. Zhou, C. Cortez-Jugo, Y. Han, Y. Ma, S. Pan, E. Hanssen, J. J. Richardson and F. Caruso, *J. Am. Chem. Soc.*, 2020, **142**, 335–341.
253 Y. La, J. Song, M. G. Jeong, A. Cho, S.-M. Jin, E. Lee and K. T. Kim, *Nat. Commun.*, 2018, **9**, 5327.
254 R. K. O'Reilly, C. J. Hawker and K. L. Wooley, *Chem. Soc. Rev.*, 2006, **35**, 1068–1083.
255 L. Tan and B. Tan, *Chem. Soc. Rev.*, 2017, **46**, 3322–3356.
256 J. Cai, K. P. Mineart, X. Li, R. J. Spontak, I. Manners and H. Qiu, *ACS Macro Lett.*, 2018, **7**, 1040–1045.
257 T. N. Gao, T. Wang, W. Wu, Y. Liu, Q. Huo, Z. A. Qiao and S. Dai, *Adv. Mater.*, 2019, **31**, 1806254.
258 Z. Li, D. Wu, X. Huang, J. Ma, H. Liu, Y. Liang, R. Fu and K. Matyjaszewski, *Energy Environ. Sci.*, 2014, **7**, 3006–3012.
259 Y. Liang, S. Lu, D. Wu, B. Sun, F. Xu and R. Fu, *J. Mater. Chem. A*, 2013, **1**, 3061–3067.
260 J. W. To, J. He, J. Mei, R. Haghpanah, Z. Chen, T. Kurosawa, S. Chen, W.-G. Bae, L. Pan, J. B.-H. Tok, J. Wilcox and Z. Bao, *J. Am. Chem. Soc.*, 2016, **138**, 1001–1009.
261 D. Liu, J.-H. Lei, L.-P. Guo, D. Qu, Y. Li and B.-L. Su, *Carbon*, 2012, **50**, 476–487.
262 L. Hu, M. Chen, X. Fang and L. Wu, *Chem. Soc. Rev.*, 2012, **41**, 1350–1362.
263 Y. Zhang, S. Gong, Q. Zhang, P. Ming, S. Wan, J. Peng, L. Jiang and Q. Cheng, *Chem. Soc. Rev.*, 2016, **45**, 2378–2395.
264 Y. Fang, Y. Lv, R. Che, H. Wu, X. Zhang, D. Gu, G. Zheng and D. Zhao, *J. Am. Chem. Soc.*, 2013, **135**, 1524–1530.
265 R. Dong, T. Zhang and X. Feng, *Chem. Rev.*, 2018, **118**, 6189–6235.
266 J. Cai, C. Li, N. Kong, Y. Lu, G. Lin, X. Wang, Y. Yao, I. Manners and H. Qiu, *Science*, 2019, **366**, 1095–1098.
267 T. Chen, L. Qiu, Z. Yang and H. Peng, *Chem. Soc. Rev.*, 2013, **42**, 5031–5041.
268 Y. Huang, Y. Mai, U. Beser, J. Teyssandier, G. Velpula, H. Van Gorp, L. A. Straasø, M. R. Hansen, D. Rizzo, C. Casiraghi, R. Yang, G. Zhang, D. Wu, F. Zhang, D. Yan, S. D. Feyter, K. Müllen and X. Feng, *J. Am. Chem. Soc.*, 2016, **138**, 10136–10139.
269 Q. Wei, F. Xiong, S. Tan, L. Huang, E. H. Lan, B. Dunn and L. Mai, *Adv. Mater.*, 2017, **29**, 1602300.
270 K. Yu, X. Pan, G. Zhang, X. Liao, X. Zhou, M. Yan, L. Xu and L. Mai, *Adv. Energy Mater.*, 2018, **8**, 1802369.
271 Y. Huang, F. Xu, L. Ganzer, F. V. Camargo, T. Nagahara, J. Teyssandier, H. Van Gorp, K. Basse, L. A. Straasø, V. Nagyte, C. Casiragi, M. R. Hansen, S. D. Feyter, D. Yan, K. Müllen, X. Feng, G. Cerullo and Y. Mai, *J. Am. Chem. Soc.*, 2018, **140**, 10416–10420.
272 W. Niu, J. Liu, Y. Mai, K. Müllen and X. Feng, *Trends Chem.*, 2019, **1**, 549–558.
273 H. M. Chen, C. K. Chen, R.-S. Liu, L. Zhang, J. Zhang and D. P. Wilkinson, *Chem. Soc. Rev.*, 2012, **41**, 5654–5671.
274 G. Zhou, L. Xu, G. Hu, L. Mai and Y. Cui, *Chem. Rev.*, 2019, **119**, 11042–11109.
275 Z.-S. Wu, X. Feng and H.-M. Cheng, *Natl. Sci. Rev.*, 2014, **1**, 277–292.
276 S. Liu, P. Gordiichuk, Z.-S. Wu, Z. Liu, W. Wei, M. Wagner, N. Mohamed-Noriega, D. Wu, Y. Mai, A. Herrmann, K. Müllen and X. Feng, *Nat. Commun.*, 2015, **6**, 8817.
277 X. Zhu, Y. Xia, X. Zhang, A. A. Al-Khalaf, T. Zhao, J. Xu, L. Peng, W. N. Hozzein, W. Li and D. Zhao, *J. Mater. Chem. A*, 2019, **7**, 8975–8983.
278 Y. Liu, A. A. Elzatahry, W. Luo, P. Zhang, J. Fan, Y. Wei, C. Wang, Y. Deng, G. Zheng, F. Zhang, Y. Tang, L. Mai and D. Zhao, *Nano Energy*, 2016, **25**, 80–90.
279 Y. Deng, H. Xue, S. Lu, Y. Song, X. Cao, L. Wang, H. Wang, Y. Zhao and H. Gu, *ACS Appl. Energy Mater.*, 2018, **1**, 4891–4898.
280 D. Hou, J. Zhang, Q. Li, P. Zhang, C. Chen, D. Yan and Y. Mai, *Langmuir*, 2018, **34**, 10924–10931.
281 Y. Fang, Y. Lv, J. Tang, H. Wu, D. Jia, D. Feng, B. Kong, Y. Wang, A. A. Elzatahry, D. Al-Dahyan, Q. Zhang, G. Zheng and D. Zhao, *Angew. Chem., Int. Ed.*, 2015, **54**, 8425–8429.
282 L. Liu, X. Yang, Y. Xie, H. Liu, X. Zhou, X. Xiao, Y. Ren, Z. Ma, X. Cheng, Y. Deng and D. Zhao, *Adv. Mater.*, 2020, **32**, 1906653.

283 Q. Wang and D. O'Hare, *Chem. Rev.*, 2012, **112**, 4124–4155.
284 L. Wang and T. Sasaki, *Chem. Rev.*, 2014, **114**, 9455–9486.
285 X. Chia, A. Y. S. Eng, A. Ambrosi, S. M. Tan and M. Pumera, *Chem. Rev.*, 2015, **115**, 11941–11966.
286 S. Liu, J. Zhang, R. Dong, P. Gordiichuk, T. Zhang, X. Zhuang, Y. Mai, F. Liu, A. Herrmann and X. Feng, *Angew. Chem., Int. Ed.*, 2016, **55**, 12516–12521.
287 B. Y. Guan, L. Yu and X. W. Lou, *Adv. Mater.*, 2016, **28**, 9596–9601.
288 F. Bonaccorso, L. Colombo, G. Yu, M. Stoller, V. Tozzini, A. C. Ferrari, R. S. Ruoff and V. Pellegrini, *Science*, 2015, **347**, 1246501.
289 E. Pomerantseva and Y. Gogotsi, *Nat. Energy*, 2017, **2**, 17089.
290 N. Wang, H. Tian, S. Zhu, D. Yue and Y. Mai, *Chin. J. Polym. Sci.*, 2018, **36**, 266–272.
291 H. Tian, N. Wang, F. Xu, P. Zhang, D. Hou, Y. Mai and X. Feng, *J. Mater. Chem. A*, 2018, **6**, 10354–10360.
292 K. Lan, Q. Wei, R. Wang, Y. Xia, S. Tan, Y. Wang, A. Elzatahry, P. Feng, L. Mai and D. Zhao, *J. Am. Chem. Soc.*, 2019, **141**, 16755–16762.
293 S. Liu, F. Wang, R. Dong, T. Zhang, J. Zhang, X. Zhuang, Y. Mai and X. Feng, *Adv. Mater.*, 2016, **28**, 8365–8370.
294 D. Hou, S. Zhu, H. Tian, H. Wei, X. Feng and Y. Mai, *ACS Appl. Mater. Interfaces*, 2018, **10**, 40800–40807.
295 H. Tan, J. Tang, J. Henzie, Y. Li, X. Xu, T. Chen, Z. Wang, J. Wang, Y. Ide, Y. Bando and Y. Yamauchi, *ACS Nano*, 2018, **12**, 5674–5683.
296 Y. Li, Y. Liu, J. Li, D. Xiong, X. Chen, M. Liu, Z. Zhong, V. Malgras, Y. Bando, Y. Yamauchi and J. Xu, *Mater. Horiz.*, 2020, **7**, 489–494.
297 C. M. Parlett, K. Wilson and A. F. Lee, *Chem. Soc. Rev.*, 2013, **42**, 3876–3893.
298 X. Yang, X. Zhuang, Y. Huang, J. Jiang, H. Tian, D. Wu, F. Zhang, Y. Mai and X. Feng, *Polym. Chem.*, 2015, **6**, 1088–1095.
299 X. Yang, Z. Lin, J. Zheng, Y. Huang, B. Chen, Y. Mai and X. Feng, *Nanoscale*, 2016, **8**, 8650–8657.
300 C. Tang, H.-F. Wang, J.-Q. Huang, W. Qian, F. Wei, S.-Z. Qiao and Q. Zhang, *J. Phys. Chem. B*, 2019, **2**, 332–371.
301 J. Tang, J. Liu, R. R. Salunkhe, T. Wang and Y. Yamauchi, *Macromol. Chem. Phys.*, 2016, **52**, 505–508.
302 P. Qiu, B. Ma, C.-T. Hung, W. Li and D. Zhao, *Acc. Chem. Res.*, 2019, **52**, 2928–2938.
303 X. Zhu, Y. Xia, X. Zhang, A. A. Al-Khalaf, T. Zhao, J. Xu, L. Peng, W. N. Hozzein, W. Li and D. Zhao, *J. Mater. Chem. A*, 2019, **7**, 8975–8983.
304 K. Lan, Y. Xia, R. Wang, Z. Zhao, W. Zhang, X. Zhang, A. Elzatahry and D. Zhao, *Matter*, 2019, **1**, 527–538.
305 Y. Xu, Y. Li, X. Qian, D. Yang, X. Chai, Z. Wang, X. Li, L. Wang and H. Wang, *Nanoscale*, 2019, **11**, 4781–4787.
306 C. Li, H. Yu, S. Liu, Y. Xu, Z. Wang, X. Li, L. Wang and H. Wang, *Chem. – Asian J.*, 2019, **14**, 3397–3403.
307 R. Liu, L. Wan, S. Liu, L. Pan, D. Wu and D. Zhao, *Adv. Funct. Mater.*, 2015, **25**, 526–533.
308 S. Schacht, Q. Huo, I. Voigt-Martin, G. Stucky and F. Schüth, *Science*, 1996, **273**, 768–771.
309 H. Zhang and A. I. Cooper, *Soft Matter*, 2005, **1**, 107–113.
310 Y. Xia, X. Na, J. Wu and G. Ma, *Adv. Mater.*, 2018, **31**, 1801159.
311 C. H. Chen, A. R. Abate, D. Lee, E. M. Terentjev and D. A. Weitz, *Adv. Mater.*, 2009, **21**, 3201–3204.
312 J. Hu, S. Zhou, Y. Sun, X. Fang and L. Wu, *Chem. Soc. Rev.*, 2012, **41**, 4356–4378.
313 K. Piradashvili, E. M. Alexandrino, F. R. Wurm and K. Landfester, *Chem. Rev.*, 2015, **116**, 2141–2169.
314 V. Mihali and A. Honciuc, *ACS Nano*, 2019, **13**, 3483–3491.
315 J. Liu, T. Yang, D.-W. Wang, G. Q. M. Lu, D. Zhao and S. Z. Qiao, *Nat. Commun.*, 2013, **4**, 2798.
316 B. Y. Guan, S. L. Zhang and X. W. Lou, *Angew. Chem., Int. Ed.*, 2018, **57**, 6176–6180.
317 S. H. Im, U. Jeong and Y. Xia, *Nat. Mater.*, 2005, **4**, 671–675.
318 Y. Wang, C. Zhang, C. Tang, J. Li, K. Shen, J. Liu, X. Qu, J. Li, Q. Wang and Z. Yang, *Macromolecules*, 2011, **44**, 3787–3794.
319 J.-B. Fan, Y. Song, H. Liu, Z. Lu, F. Zhang, H. Liu, J. Meng, L. Gu, S. Wang and L. Jiang, *Sci. Adv.*, 2017, **3**, e1603203.
320 C. Chen, H. Wang, C. Han, J. Deng, J. Wang, M. Li, M. Tang, H. Jin and Y. Wang, *J. Am. Chem. Soc.*, 2017, **139**, 2657–2663.
321 K. H. Ku, J. M. Shin, H. Yun, G. R. Yi, S. G. Jang and B. J. Kim, *Adv. Funct. Mater.*, 2018, **28**, 1802961.
322 Y. Song, J. Zhou, J. B. Fan, W. Zhai, J. Meng and S. Wang, *Adv. Funct. Mater.*, 2018, **28**, 1802493.
323 H. Lv, D. Xu, L. Sun, J. Henzie, A. Lopes, Q. Gu, Y. Yamauchi and B. Liu, *Nano Lett.*, 2019, **19**, 3379–3385.
324 D. Liu, N. Xue, L. Wei, Y. Zhang, Z. Qin, X. Li, B. P. Binks and H. Yang, *Angew. Chem., Int. Ed.*, 2018, **57**, 10899–10904.
325 Y. Xue, Q. Zhang, W. Wang, H. Cao, Q. Yang and L. Fu, *Adv. Energy Mater.*, 2017, **7**, 1602684.
326 H. Shi, *Electrochim. Acta*, 1996, **41**, 1633–1639.
327 D. Qu, *J. Power Sources*, 2002, **109**, 403–411.
328 P. Simon and Y. Gogotsi, *Nat. Mater.*, 2008, **7**, 845–854.
329 Y. Liang, R. Fu and D. Wu, *ACS Nano*, 2013, **7**, 1748–1754.
330 J. Park, Y. Nabe, T. Hayakawa and M. Kakimoto, *ACS Catal.*, 2014, **4**, 3749–3754.
331 T. Lin, I.-W. Chen, F. Liu, C. Yang, H. Bi, F. Xu and F. Huang, *Science*, 2015, **350**, 1508–1513.
332 J. Xue, T. Wu, Y. Dai and Y. Xia, *Chem. Rev.*, 2019, **119**, 5298–5415.
333 X. Peng, L. Peng, C. Wu and Y. Xie, *Chem. Soc. Rev.*, 2014, **43**, 3303–3323.
334 E. Pomerantseva, F. Bonaccorso, X. Feng, Y. Cui and Y. Gogotsi, *Science*, 2019, **366**, 969.
335 M. Armand and J. M. Tarascon, *Nature*, 2008, **451**, 652–657.
336 M. D. Levi and D. Aurbach, *J. Phys. Chem. B*, 1997, **101**, 4641–4647.
337 A. B. Fuertes, G. Lota, T. A. Centeno and E. Frackowiak, *Electrochim. Acta*, 2005, **50**, 2799–2805.
338 A. Vu, Y. Qian and A. Stein, *Adv. Energy Mater.*, 2012, **2**, 1056–1085.
339 M. Fisher, X. Hua, B. Wilts, E. Castillo-Martinez and U. Steiner, *ACS Appl. Mater. Interfaces*, 2018, **10**, 1646–1653.
340 G. Wang, H. Liu, J. Liu, S. Qiao, G. M. Lu, P. Munroe and H. Ahn, *Adv. Mater.*, 2010, **22**, 4944–4948.

341 D. Saikia, J. R. Deka, C.-J. Chou, C.-H. Lin, Y.-C. Yang and H.-M. Kao, *ACS Appl. Energy Mater.*, 2019, **2**, 1121–1133.
342 H. Liu, X. Liu, W. Li, X. Guo, Y. Wang, G. Wang and D. Zhao, *Adv. Energy Mater.*, 2017, **7**, 1700283.
343 D. Saikia, T.-H. Wang, C.-J. Chou, J. Fang, L.-D. Tsai and H.-M. Kao, *RSC Adv.*, 2015, **5**, 42922–42930.
344 S. Fang, D. Bresser and S. Passerini, *Adv. Energy Mater.*, 2020, **10**, 1902485.
345 H. Liu, Z. Bi, X. G. Sun, R. R. Unocic, M. P. Paranthaman, S. Dai and G. M. Brown, *Adv. Mater.*, 2011, **23**, 3450–3454.
346 C. Jo, Y. Kim, J. Hwang, J. Shim, J. Chun and J. Lee, *Chem. Mater.*, 2014, **26**, 3508–3514.
347 J. Hwang, C. Jo, K. Hur, J. Lim, S. Kim and J. Lee, *J. Am. Chem. Soc.*, 2014, **136**, 16066–16072.
348 J. Hu, C.-F. Sun, E. Gillette, Z. Gui, Y. Wang and S. B. Lee, *Nanoscale*, 2016, **8**, 12958–12969.
349 Y. Fang, Y. Lv, F. Gong, A. A. Elzatahry, G. Zheng and D. Zhao, *Adv. Mater.*, 2016, **28**, 9385–9390.
350 H. T. Le, D. T. Ngo, X.-M. Pham, T.-Y. Nguyen, T.-D. Dang and C.-J. Park, *J. Power Sources*, 2019, **440**, 227104.
351 R. A. Adams, A. Varma and V. G. Pol, *Adv. Energy Mater.*, 2019, **9**, 1900550.
352 Y. Li, Y. Lu, P. Adelhelm, M.-M. Titirici and Y.-S. Hu, *Chem. Soc. Rev.*, 2019, **48**, 4655–4687.
353 J. Leng, Z. Wang, J. Wang, H.-H. Wu, G. Yan, X. Li, H. Guo, Y. Liu, Q. Zhang and Z. Guo, *Chem. Soc. Rev.*, 2019, **48**, 3015–3072.
354 Y. Liang, W.-H. Lai, Z. Miao and S.-L. Chou, *Small*, 2018, **14**, 1702514.
355 L. Zhu, Y. Shen, M. Sun, J. Qian, Y. Cao, X. Ai and H. Yang, *Chem. Commun.*, 2013, **49**, 11370–11372.
356 M. Zhou, W. Li, T. Gu, K. Wang, S. Cheng and K. Jiang, *Chem. Commun.*, 2015, **51**, 14354–14356.
357 X. Xiang, K. Zhang and J. Chen, *Adv. Mater.*, 2015, **27**, 5343–5364.
358 N. Yabuuchi, K. Kubota, M. Dahbi and S. Komaba, *Chem. Rev.*, 2014, **114**, 11636–11682.
359 X. Wu, Y. Chen, Z. Xing, C. W. K. Lam, S.-S. Pang, W. Zhang and Z. Ju, *Adv. Energy Mater.*, 2019, **9**, 1900343.
360 R. Rajagopalan, Y. Tang, X. Ji, C. Jia and H. Wang, *Adv. Funct. Mater.*, 2020, **30**, 1909486.
361 W. Wang, J. Zhou, Z. Wang, L. Zhao, P. Li, Y. Yang, C. Yang, H. Huang and S. Guo, *Adv. Energy Mater.*, 2018, **8**, 1701648.
362 P. Bruce, S. Freunberger, L. Hardvick and J.-M. L. Trascon, *Nat. Mater.*, 2012, **11**, 19–29.
363 R. Fang, S. Zhao, Z. Sun, D. W. Wang, H. M. Cheng and F. Li, *Adv. Mater.*, 2017, **29**, 1606823.
364 J. Schuster, G. He, B. Mandlmeier, T. Yim, K. T. Lee, T. Bein and L. F. Nazar, *Angew. Chem., Int. Ed.*, 2012, **51**, 3591–3595.
365 F. Jin, S. Xiao, L. Lu and Y. Wang, *Nano Lett.*, 2015, **16**, 440–447.
366 G. Hu, C. Xu, Z. Sun, S. Wang, H. M. Cheng, F. Li and W. Ren, *Adv. Mater.*, 2016, **28**, 1603–1609.
367 R. Fang, G. Li, S. Zhao, L. Yin, K. Du, P. Hou, S. Wang, H.-M. Cheng, C. Liu and F. Li, *Nano Energy*, 2017, **42**, 205–214.
368 Z. Li, L. Yuan, Z. Yi, Y. Sun, Y. Liu, Y. Jiang, Y. Shen, Y. Xin, Z. Zhang and Y. Huang, *Adv. Energy Mater.*, 2014, **4**, 1301473.
369 X. Ji, K. T. Lee and L. F. Nazar, *Nat. Mater.*, 2009, **8**, 500–506.
370 J. Song, T. Xu, M. L. Gordin, P. Zhu, D. Lv, Y.-B. Jiang, Y. Chen, Y. Duan and D. Wang, *Adv. Funct. Mater.*, 2014, **24**, 1243–1250.
371 Z. Li, Y. Jiang, L. Yuan, Z. Yi, C. Wu, Y. Liu, P. Strasser and Y. Huang, *ACS Nano*, 2014, **8**, 9295–9303.
372 S. Choudhury, M. Agrawal, P. Formanek, D. Jehnichen, D. Fischer, B. Krause, V. Albrecht, M. Stamm and L. Ionov, *ACS Nano*, 2015, **9**, 6147–6157.
373 H.-J. Liu, J. Wang, C.-X. Wang and Y.-Y. Xia, *Adv. Energy Mater.*, 2011, **1**, 1101–1108.
374 Y. Korenblit, M. Rose, E. Kockrick, L. Borchardt, A. Kvit, S. Kaskel and G. Yushin, *ACS Nano*, 2010, **4**, 1337–1344.
375 Q. Li, R. Jiang, Y. Dou, Z. Wu, T. Huang, D. Feng, J. Yang, A. Yu and D. Zhao, *Carbon*, 2011, **49**, 1248–1257.
376 X. Xi, D. Wu, L. Han, Y. Yu, Y. Su, W. Tang and R. Liu, *ACS Nano*, 2018, **12**, 5436–5444.
377 J. Hu, M. Noked, E. Gillette, Z. Gui and S. B. Lee, *Carbon*, 2015, **93**, 903–914.
378 N. Choudhary, C. Li, J. Moore, N. Nagaiah, L. Zhai, Y. Jung and J. Thomas, *Adv. Mater.*, 2017, **29**, 1605336.
379 H. Peng, B. Yao, X. Wei, T. Liu, T. Kou, P. Xiao, Y. Zhang and Y. Li, *Adv. Energy Mater.*, 2019, **9**, 1803665.
380 H. Chen, Q. Li, N. Teng, D. Long, C. Ma, Y. Wei, J. Wang and L. Ling, *Electrochim. Acta*, 2016, **214**, 231–240.
381 J.-W. Lang, X.-B. Yan, X.-Y. Yuan, J. Yang and Q.-J. Xue, *J. Power Sources*, 2011, **196**, 10472–10478.
382 Y. Shao, M. F. El-Kady, J. Sun, Y. Li, Q. Zhang, M. Zhu, H. Wang, B. Dunn and R. B. Kaner, *Chem. Rev.*, 2018, **118**, 9233–9280.
383 D. Wei, M. R. Scherer, C. Bower, P. Andrew, T. Ryhänen and U. Steiner, *Nano Lett.*, 2012, **12**, 1857–1862.
384 S. Zheng, X. Shi, P. Das, Z. S. Wu and X. Bao, *Adv. Mater.*, 2019, **31**, 1900583.
385 D. Yu, K. Goh, H. Wang, L. Wei, W. Jiang, Q. Zhang, L. Dai and Y. Chen, *Nat. Nanotechnol.*, 2014, **9**, 555–562.
386 S. Zheng, X. Tang, Z.-S. Wu, Y.-Z. Tan, S. Wang, C. Sun, H.-M. Cheng and X. Bao, *ACS Nano*, 2017, **11**, 2171–2179.
387 S. Zheng, J. Ma, Z.-S. Wu, F. Zhou, Y.-B. He, F. Kang, H.-M. Cheng and X. Bao, *Energy Environ. Sci.*, 2018, **11**, 2001–2009.
388 I. Roger, M. A. Shipman and M. D. Symes, *Nat. Rev. Chem.*, 2017, **1**, 0003.
389 Y. Nie, L. Li and Z. Wei, *Chem. Soc. Rev.*, 2015, **44**, 2168–2201.
390 S. H. Lee, J. Kim, D. Y. Chung, J. M. Yoo, H. S. Lee, M. J. Kim, B. S. Mun, S. G. Kwon, Y.-E. Sung and T. Hyeon, *J. Am. Chem. Soc.*, 2019, **141**, 2035–2045.
391 V. Yarlagadda, M. K. Carpenter, T. E. Moylan, R. S. Kukreja, R. Koestner, W. Gu, L. Thompson and A. Kongkanand, *ACS Energy Lett.*, 2018, **3**, 618–621.
392 F. Cheng and J. Chen, *Chem. Soc. Rev.*, 2012, **41**, 2172–2192.
393 D. Wang and D. Astruc, *Chem. Soc. Rev.*, 2017, **46**, 816–854.
394 X. Liu and L. Dai, *Nat. Rev. Mater.*, 2016, **1**, 16064.

395 H. Xue, J. Tang, H. Gong, H. Guo, X. Fan, T. Wang, J. He and Y. Yamauchi, *ACS Appl. Mater. Interfaces*, 2016, **8**, 20766–20771.
396 H.-W. Liang, W. Wei, Z.-S. Wu, X. Feng and K. Müllen, *J. Am. Chem. Soc.*, 2013, **135**, 16002–16005.
397 Z. Li, G. Li, L. Jiang, J. Li, G. Sun, C. Xia and F. Li, *Angew. Chem., Int. Ed.*, 2015, **54**, 1494–1498.
398 G. A. Ferrero, K. Preuss, A. Marinovic, A. B. Jorge, N. Mansor, D. J. Brett, A. B. Fuertes, M. Sevilla and M.-M. Titirici, *ACS Nano*, 2016, **10**, 5922–5932.
399 F. L. Meng, Z. L. Wang, H. X. Zhong, J. Wang, J. M. Yan and X. B. Zhang, *Adv. Mater.*, 2016, **28**, 7948–7955.
400 J. P. Paraknowitsch and A. Thomas, *Energy Environ. Sci.*, 2013, **6**, 2839–2855.
401 X. Wang, G. Sun, P. Routh, D.-H. Kim, W. Huang and P. Chen, *Chem. Soc. Rev.*, 2014, **43**, 7067–7098.
402 M. Zhou, H.-L. Wang and S. Guo, *Chem. Soc. Rev.*, 2016, **45**, 1273–1307.
403 K. Gong, F. Du, Z. Xia, M. Durstock and L. Dai, *Science*, 2009, **323**, 760–764.
404 D. Hou, J. Zhang, H. Tian, Q. Li, C. Li and Y. Mai, *Adv. Mater. Interfaces*, 2019, **6**, 1901476.
405 C. G. Morales-Guio, L.-A. Stern and X. Hu, *Chem. Soc. Rev.*, 2014, **43**, 6555–6569.
406 S. Lu and Z. Zhuang, *Sci. China Mater.*, 2016, **59**, 217–238.
407 R. S. Datta, F. Haque, M. Mohiuddin, B. J. Carey, N. Syed, A. Zavabeti, B. Zhang, H. khan, K. J. Berean, J. Z. Ou, N. Mahommd, T. Daeneke and K. Kalantar-zadeh, *J. Mater. Chem. A*, 2017, **5**, 24223–24231.
408 M. Miao, J. Pan, T. He, Y. Yan, B. Y. Xia and X. Wang, *Chem. – Eur. J.*, 2017, **23**, 10947–10961.
409 J. D. Benck, T. R. Hellstern, J. Kibsgaard, P. Chakthranont and T. F. Jaramillo, *ACS Catal.*, 2014, **4**, 3957–3971.
410 P. Xiao, M. A. Sk, L. Thia, X. Ge, R. J. Lim, J.-Y. Wang, K. H. Lim and X. Wang, *Energy Environ. Sci.*, 2014, **7**, 2624–2629.
411 Z. Luo, R. Miao, T. D. Huan, I. M. Mosa, A. S. Poyraz, W. Zhong, J. E. Cloud, D. A. Kriz, S. Thanneeru, J. He, Y. Zhang, R. Ramprasad and S. L. Suib, *Adv. Energy Mater.*, 2016, **6**, 1600528.
412 L. Han, S. Dong and E. Wang, *Adv. Mater.*, 2016, **28**, 9266–9291.
413 B. Jiang, J. Kim, Y. Guo, K. C. Wu, S. M. Alshehri, T. Ahamad, N. Alhokbany, J. Henzie and Y. Yamachi, *Catal. Sci. Technol.*, 2019, **9**, 3697–3702.
414 J. Ran, J. Zhang, J. Yu, M. Jaroniec and S. Z. Qiao, *Chem. Soc. Rev.*, 2014, **43**, 7787–7812.
415 W. Wang, X. Xu, W. Zhou and Z. Shao, *Adv. Sci.*, 2017, **4**, 1600371.
416 A. Fujishima and K. Honda, *Nature*, 1972, **238**, 37–38.
417 D. K. Lee, D. Lee, M. A. Lumley and K.-S. Choi, *Chem. Soc. Rev.*, 2019, **48**, 2126–2157.
418 S. Kment, F. Riboni, S. Pausova, L. Wang, L. Wang, H. Han, Z. Hubicka, J. Krysa, P. Schmuki and R. Zboril, *Chem. Soc. Rev.*, 2017, **46**, 3716–3769.
419 K. Lan, R. Wang, W. Zhang, Z. Zhao, A. Elzatahry, X. Zhang, Y. Liu, D. Al-Dhayan, Y. Xia and D. Zhao, *Chem*, 2018, **4**, 2436–2450.
420 J. H. Kim, D. Hansora, P. Sharma, J.-W. Jang and J. S. Lee, *Chem. Soc. Rev.*, 2019, **48**, 1908–1971.
421 X. Chen, S. Shen, L. Guo and S. S. Mao, *Chem. Rev.*, 2010, **110**, 6503–6570.
422 H.-Y. Lin, H.-C. Yang and W.-L. Wang, *Catal. Today*, 2011, **174**, 106–113.
423 M. Faraji, M. Yousefi, S. Yousefzadeh, M. Zirak, N. Naseri, T. H. Jeon, W. Choi and A. Z. Moshfegh, *Energy Environ. Sci.*, 2019, **12**, 59–95.
424 A. Primo, T. Marino, A. Corma, R. Molinari and H. Garcia, *J. Am. Chem. Soc.*, 2011, **133**, 6930–6933.
425 A. Tanaka, K. Hashimoto and H. Kominami, *J. Am. Chem. Soc.*, 2014, **136**, 586–589.
426 J. Leng, Z. Wang, J. Wang, H.-H. Wu, G. Yan, X. Li, H. Guo, Y. Liu, Q. Zhang and Z. Guo, *Chem. Soc. Rev.*, 2019, **48**, 3015–3072.
427 B. O'regan and M. Grätzel, *Nature*, 1991, **353**, 737–740.
428 D. Feng, W. Luo, J. Zhang, M. Xu, R. Zhang, H. Wu, Y. Lv, A. M. Asiri, S. B. Khan, M. M. Rahman, G. Zheng and D. Zhao, *J. Mater. Chem. A*, 2013, **1**, 1591–1599.
429 M. Zukalova, A. Zukal, L. Kavan, M. K. Nazeeruddin, P. Liska and M. Grätzel, *Nano Lett.*, 2005, **5**, 1789–1792.
430 E. J. Crossland, M. Nedelcu, C. Ducati, S. Ludwigs, M. A. Hillmyer, U. Steiner and H. J. Snaith, *Nano Lett.*, 2008, **9**, 2813–2819.
431 M. Nedelcu, J. Lee, E. J. W. Crossland, S. C. Warren, M. C. Orilall, S. Guldin, S. Hüttner, C. Ducati, D. Eder, U. Wiesner and H. J. Snaith, *Soft Matter*, 2009, **5**, 134–139.
432 P. Docampo, S. Guldin, M. Stefik, P. Tiwana, M. C. Orilall, S. Hüttner, H. Sai, U. Wiesner, U. Steiner and H. J. Snaith, *Adv. Funct. Mater.*, 2010, **20**, 1787–1796.
433 S. Guldin, P. Docampo, M. Stefik, G. Kamita, U. Wiesner, H. J. Snaith and U. Steiner, *Small*, 2012, **8**, 432–440.
434 K. W. Tan, D. T. Moore, M. Saliba, H. Sai, L. A. Estroff, T. Hanrath, H. J. Snaith and U. Wiesner, *ACS Nano*, 2014, **8**, 4730–4739.
435 Y. Liu, R. Che, G. Chen, J. Fan, Z. Sun, Z. Wu, M. Wang, B. Li, J. Wei, Y. Wei, G. Wang, G. Guan, A. A. Elzatahry., A. A. Bagabas, A. M. Al-Enizi, Y. Deng, H. Peng and D. Zhao, *Sci. Adv.*, 2015, **1**, e1500166.
436 M. A. Green, A. Ho-Baillie and H. J. Snaith, *Nat. Photonics*, 2014, **8**, 506–514.
437 H. Halim and Y. Guo, *Sci. China Mater.*, 2016, **59**, 495–506.
438 A. K. Jena, A. Kulkarni and T. Miyasaka, *Chem. Rev.*, 2019, **119**, 3036–3103.
439 N. J. Jeon, J. H. Noh, W. S. Yang, Y. C. Kim, S. Ryu, J. Seo and S. I. Seok, *Nature*, 2015, **517**, 476–480.
440 C.-C. Chung, C. S. Lee, E. Jokar, J. H. Kim and E. W.-G. Diau, *J. Phys. Chem. C*, 2016, **120**, 9619–9627.

